Density oscillations of one-dimensional correlated electron systems from Density Functional Theory

Limitations of Local Density Approximation (LDA) in describing Luttinger liquids

Doctoral Thesis

JOVAN ODAVIĆ

Institute for Theory of Statistical Physics
RWTH Aachen University
Aachen, Germany 2019

Density oscillations of one-dimensional correlated electron systems from Density Functional Theory

Limitations of Local Density Approximation (LDA) in describing Luttinger liquids

Von der Fakultät für Mathematik, Informatik und Naturwissenschaften der RWTH Aachen University zur Erlangung des akademischen Grades eines Doktors der Naturwissenschaften

vorgelegt von

Jovan Odavić, M. Sc. Physik
aus Sremski Karlovci (Serbien)

Berichter:
Prof. Dr. Volker Meden
Prof. Dr. Herbert Schoeller
Dr. Nicole Helbig

Tag der mündlichen Prüfung: 21.06.2019

Density oscillations of one-dimensional correlated electron systems from Density Functional Theory. Limitations of Local Density Approximation (LDA) in describing Luttinger liquids.

Committee chair: Prof. Dr. Markus Morgenstern
Institute for Condense Matter Physics, Institut B, RWTH Aachen University

Examiner/Reporter/Adviser: Prof. Dr. Volker Meden
Institute for Theory of Statistical Physics, RWTH Aachen University

Examiner/Reporter/Adviser: Dr. Nicole Helbig
Peter-Grünberg Institut and Institute for Advanced Simulation, Forschungszentrum Jülich

Additional Reporter: Prof. Dr. Herbert Schoeller
Institute for Theory of Statistical Physics, RWTH Aachen University

Examiner: Prof. Dr. Riccardo Mazzarello
Institute for Theoretical Solid State Physics, RWTH Aachen University

Doctoral Thesis

Institute for Theory of Statistical Physics
RWTH Aachen University

Declaration of Authorship

I, Jovan Odavić

declare that this thesis and the work presented in it are my own and has been generated by me as the result of my own original research.

I do solemnely swear that:

1. This work was done wholly while in candidature for the doctoral degree at this faculty and university;
2. Where any part of this thesis has previously been submitted for a degree or any other qualification at this university or any other institution, this has been clearly stated;
3. Where I have consulted the published work of othersor myself, this is always clearly attributed;
4. Where I have quoted from the work of othersor myself, the source is always given. This thesis is entirely my own work, with the exception of such quotations;
5. I have acknowledged all majorsources of assistance;
6. Where the thesis is based on work done by myself jointly with others, I have made clear exactly what was done by others and what I have contributed myself;
7. None of this work has been published before submission.

Aachen, 08.05.2019

Posvećeno Nadi Odavić[†] (1958-2018)

Abstract

Gapless quasi-one-dimensional systems are not described by Fermi liquid theory, as is the case of interacting systems in higher dimensions, but rather by another unique framework, the Luttinger liquid theory. Our work is focused on the questions regarding strongly correlated one-dimensional Luttinger liquid physics. In particular, we try to bridge the gap between what is known from field theoretical methods, such as bosonization, and the real physical systems that are fabricated in the laboratory. Beyond weak interactions this gap is wider than most theorist imagine and experimentalist would like. By starting from microscopic models we investigate, whether or not, methods such as Kohn-Sham Density Functional Theory (KS DFT) using the Local Density Approximation (LDA) for the exchange-correlation potential can lead to a correct description of the underlying Luttinger liquid low-energy fixed point. Basic theorems of KS DFT guarantee that the KS ground state charge density matches the density of the fully interacting many-body if the exchange-correlation potential is exact. Therefore, in this thesis we focus exclusively on the oscillations, known as Friedel oscillation, that occur in the density in presence of a boundary (or infinitely strong impurity). The particular power-law decay of the Friedel oscillations, away from the boundary and into the bulk, represent one of the hallmarks of the Luttinger liquid paradigm. In this thesis we use the Hartree-Fock approximation to investigate the power-law decay of Friedel oscillations, propose a method to compute the density based on Matsubara Green's functions and most importantly clarify the limitations of LDA in describing Luttinger liquids.

Deutsche Zusammenfassung

Im Gegensatz zu zwei- und drei-dimensionalen Systemen werden quasi-eindimensionale Systeme ohne Bandlücke nicht durch die Fermi-Flüssigkeitstheorie, sondern durch die sogenannten Luttinger-Flüssigkeitstheorie beschrieben. Unsere Arbeit untersucht Eigenschaften besagter Systeme in der Anwesenheit von starken Korrelationen. Wir verbinden Erkenntnisse die durch feldtheoretische Methoden, wie etwa Bosonisierung, erlangt wurden mit Kenntnissen über reale physikalische Systeme. Jenseits des Grenzfalls schwacher Wechselwirkung ist die Kluft zwischen diesen Bereichen noch immer relativ groß. Unter Benutzung von mikroskopischen Modellen untersuchen wir ob etwa die Kohn-Sham Dichte Funktional Theorie (KS DFT) kombiniert mit der Lokalen Dichte Näherung (LDA) eine korrekte Beschreibung des Luttinger Flüssigkeit Fixpunktes liefern kann. Grundlegende Theoreme der KS DFT garantieren, dass die Ladungsdichte des KS Grundzustandes mit der Dichte des wechselwirkenden Viel-Teilchensystems übereinstimmt, wenn das Austausch-Korrelations Potential richtig gewählt wird. Wir konzentrieren uns auf die Dichte-Oszillationen, auch bekannt als Friedel Oszillationen, die auftreten, wenn das System einen Rand hat. Der Potenz-ähnliche Zerfall der Friedel Oszillationen vom Rand in das System hinein ist eine der typischen Eigenschaften von Luttinger Flssigkeits Physik. In dieser Arbeit benutzen wir die Hartee-Fock Näherung um den Zerfall der Friedel Oszillationen zu untersuchen, wir entwickeln eine auf Matsubara Greensfunktionen basierende Methode um die Dichte zu berechnen und bestimmen dadurch die Grenzen der Anwendbarkeit der LDA in der Beschreibung von Luttinger Flüssigkeiten.

Contents

1 Introduction

In classical physics, electrostatic screening is a well understood phenomena; see Ref. [HD23]. For example, a positively charged macroscopic particle deposited in a negatively charged environment is going to be screened. In particular, the mobile negative charge carriers distribute themselves such that the stationary positive charge is neutralized, and according to the decaying Coulomb potential multiplied by an exponential damping term.

On the other hand, at mesoscopic scales and at sufficiently low temperatures the physics of charge screening is considerably different. The presence of a charge impurity in a homogeneous Fermi gas induces charge density modulations known as Friedel oscillations (FO); see Refs. [Fri58, TZ85, SG05]. These charge oscillations occur with $2k_{\mathrm{F}}$ periodicity[1] and are an intrinsic quantum phenomena. In case of non-interacting fermions the FO decay as

$$n(r) \sim \frac{\cos\left(2k_{\mathrm{F}}r + \delta\right)}{r^{D}}, \tag{1.1}$$

where δ is a phase shift, D denotes the spatial dimension and r the distance from the impurity. The powerlaw decay r^{-D} of the charge oscillations is a consequence of the non-analyticity of the static density response function[2] $\chi_0(q)$ at $q = 2k_{\mathrm{F}}$ which occurs due to the sharp metallic Fermi surface.

[1] Here k_{F} denotes the Fermi momentum.

[2] In the literature also known as the non-interacting Lindhard's function; see Refs. [Giu08, SG05] for the explicit definition, discussion and relationship of the Lindhard function to the density.

In case of two- and three-dimensional electronic Fermi liquids, the electron-electron interactions do not induce any additional non-analytic behavior in the static response function χ (compared to the non-interacting response function χ_0), and according to Ref. [SG05] this implies no fundamental changes to the powerlaw decay of FO in Eq. 1.1. In particular, the exponent remains unchanged. However, in one dimension the interactions lead to non-trivial modifications to the FO. In 1D the density amplitudes asymptotically decay as a power law with an exponent that depends on the interaction[3]. This change is rooted in the observation that in 1D the excitations are not quasi-particle like, but rather of collective nature.

The behavior of FO and other correlation functions in 1D is captured by the bosonization approach; see Ref. [Gia04]. In fact, all correlation functions exhibit powerlaw behavior with exponents which are considered to be nonuniversal functions parameterized by a single variable, the Luttinger parameter K. This is due to the low-energy properties of various 1D systems being captured by the Tomonaga-Luttinger model[4]. According to Ref. [Hal81] this implies the existence of a Luttinger liquid (LL) universality class, which replaces the Fermi liquid description valid in higher dimension. The LL description tells us that the relations between the exponents of different correlation functions are universal; see Ref. [Gia12].

The powerlaw behavior of correlation functions is typical for systems at the critical phase transition point. Due to the long-range quantum fluctuations, one-dimensional systems are always on the verge of ordering and, therefore, considered to be critical.

The LL powerlaw behavior has already been verified in a number of 1D systems with multitude of experimental techniques. In particular, in organic conductors like the Bechgaard salts, different and independent measurements such as those of optical conductivity, temperature dependent conductivity and transport found an agreement with LL theory predictions; see Ref. [Gia12] and references therein. In such compounds, the measured power law exponents[5] and their relationships (predicted from theory) between each other

[3] Among other things; see Ref. [Fra17] and discussion surrounding it.

[4] Which turns out to be the renormalization group fixed point model for all of the different models; see Ref. [Lut63].

[5] In these different observables.

was shown to hold in a particular energy window. Thereby, hinting at the universality paradigm of LLs, but not decisively confirming it due to the lack of further tuning parameters (e.g. interaction) within the experimental setups. There are other experimental results which are in agreement with LL theoretical predictions, such as: high-resolution photo-emission experiments on a number of quasi-one-dimensional conductors, transport measurements in carbon nano-tubes and measurements of current-voltage characteristics in fractional quantum Hall fluids; see Refs. [Sch02, Gia12] for an expanded but not complete literature account.

The FO have been observed in scanning tunneling microscopy (STM) experiments in dimensions higher than one, by probing the local density of states (LDOS); see Refs. [PSH+98, KBYH01, CLE93]. Various, direct and indirect, experimental measurements of FO in 1D have been proposed over the last two decades; see Refs. [Egg00, RHL+17]. Recent advances in ultra cold Fermi gases in Refs. [BDZ08, GPS08], together with the developments in high resolution imagining using microscope objectives in Refs. [ZMM+11, CNO+15, HHK+15], potentially offer access to direct measurements of FO in artificial cold atom 1D systems. Moreover, interactions can be tuned in this kind of experiments, which enables realistic simulation of interacting many-body systems and the study of correlation effects on the observable such as the density. Recently, an experimental feasibility study has been carried out in Ref. [RHL+17], which found that direct measurements of FO in 1D, with present technology, are indeed within reach.

The study of the interplay between impurity and interaction effects in 1D is not just of academic interest. Transport properties of quasi-one-dimensional systems such as carbon nano-tubes, atomic point contacts and quantum wires are dramatically influenced by both; see Ref. [DBGY10]. Therefore, any future mesoscopic devices will have to take these effects into account.

On the theoretical side, progress still has to be made in respect to the direct comparison to the experimental results. The relation of the finite size effects, environment and impurities defects[6] with the

[6] All of the listed are inherent in any experimental realization; the experimental samples are finite in length/width, they can not be perfectly decoupled from the environment and manufacturing techniques always introduce imperfections.

correlation effects and how, in such complex systems, the asymptotic LL physics sets in is still a subject of scientific study. The issue lies in the inability to solve the Schrödinger equation for systems with large number of interacting particles. Available exact analytical and numerical methods in 1D treat only extremely small systems, such as the Bethe ansatz (BA) and the exact diagonalization (ED), respectively[7].

The BA equations, in principle, provide us with a closed set of equations that, when solved, contain the full information about eigenvalues and eigenstates[8]. Evaluating observables in the exact BA basis is, however, extremely difficult and challenging; see e.g. Ref. [KMT99]. The BA equations are algebraic equations which in the thermodynamic (TD) limit become integral equations which are then again subject to numerical evaluation. In particular limits even closed form analytic TD solutions are available. If conformal invariance is assumed the BA equations in the TD limit can be used to compute the Luttinger parameter K for particular microscopic models; see Ref. [WVP96]. ED, on the other hand, is rendered useless for any investigation of the low energy fixed point because the Hilbert space of a quantum many-body problem grows exponentially with system size.

With the mentioned exact methods *the transition* to the long-distance (or equivalently low-energy) physics of LL can not be resolved. However, a number of approximate methods exist that can provide an alternative.

Methods, such as the Density Matrix Renormalization Group[9] (DMRG) offer extremely precise estimates[10] for the eigenstates and many different correlation functions (e.g. the ground state density) at an arbitrary interaction strength. Due to the particular scaling of the entanglement entropy in one dimension, DMRG can treat much larger systems than ED; see Ref. [VLRK03, Sch11a]. However, probing the scales at which the system reaches the asymptotic LL

[7] See Chap. 3 for the particular BA application and see Ref. [NM05] for ED

[8] With the increase of the system size the numerical effort to solve the exact equations dramatically increases as well.

[9] See Ref. [Whi92, Whi93] for the original formulation of the algorithm and e.g. Ref. [SMMS02] for a more specialized application of DMRG in the context of LL.

[10] In many applications, the precision is limited only by machine precision.

regime with this method remains computationally challenging. The Hilbert space eventually become too large to be efficiently treated; see Ref. [Sch11a]. Therefore, physics in the intermediate to large scales has to be extrapolated. In the TD limit or the true low energy limit, the *infinite* DMRG (iDMRG) algorithm can be formulated, giving the correct asymptotics of microscopic lattice models; see Refs. [KM12, Sch11b, Vid07].

Other methods based on the renormalization group idea, such as the Functional Renormalization Group[11] (fRG) have been used to analyze the FO decay in 1D, LDOS and other quantities; see Refs. [AEM+04, Ens05]. fRG is approximate because one has to truncate an infinite hierarchy of coupled flow equations that describe how a particular model arrives at its low energy fixed point. With simple truncation schemes this method is able to access weak to intermediate correlated regimes, and was shown to perform better than the perturbation theory, which is valid only for weak interactions[12]. The fRG is systematic and flexible, able to treat extremely large systems with impurities, coupling to an environment and additionally allows for a consistent study of the finite size effects. However, to access the strongly correlated regimes, the infinite hierarchy has to be truncated in more elaborate ways which do not necessarily lead to an efficient algorithm; see Refs. [MSH+12].

Another method, typically used by material scientists and chemist and known as Density Functional Theory (DFT) has been employed recently in studies of LL physics. In this thesis, we focus on this method together with the perturbation theory in an attempt to describe the correlation effects in FO. In the following paragraphs we present a more detailed overview of the literature and the DFT method.

In Ref. [SDSE08] the static response function χ of the spinless fermion model in 1D was investigated for LL physics signatures. The authors used the Local Density Approximation (LDA) built from the BA ground state energy in the TD limit for the exchange-correlation functional and observed that it deviates from the exact response

[11] In the literature also known as the *exact* renormalization group

[12] In particular, perturbation theory was shown to perform well with infinitely strong impurities (open boundary conditions) and not so well for weak and moderately strong impurities

function as $q \to 2k_{\mathrm{F}}$. In particular, the LDA develops a finite cusp in χ^{LDA} which is independent of system size L instead of a power law divergence as $L \to \infty$; see Fig. 3. of the mentioned reference. Additionally, the dynamical response function $\chi(q, \omega)$ was computed using the adiabatic[13] LDA. The response function χ^{ALDA} displays features of the particle-hole continuum[14] and correct scaling (in agreement with LL predictions) in the low frequency $\omega \to 0$ and small wave-vector $q \to 0$ limit. They also found that the Fermi velocity v_{F} is correctly reproduced by the LDA for a wide range of fillings when compared to the exact charge velocity from BA, something that the random-phase approximation (typically reliable in higher dimensions) is unable to do; see Fig. 5 in Ref. [SDSE08]. However, the transmission probability thought a single impurity is not correctly renormalized by the LDA built from the BA solution; see Fig. 6 in the same paper. This indicates that impurity physics might not be correctly captured by this particular approximation.

Nevertheless, questions regarding impurity screening and in particular FO in the same model of spinless fermions as in Ref. [SDSE08] have been raised[15] in Ref. [AC07]. The density oscillation amplitudes were found to be incorrectly reproduced by the LDA, at and away from half-filling, when compared to the exact amplitudes from ED for systems of size $L \leq 24$. The asymptotic decay of FO has not been investigated by the authors. In this thesis, we do perform such an analysis; see later paragraphs for an overview.

In Ref. [LSOC03] the FO in a 1D Hubbard model have been investigated using LDA DFT, where the LDA is built from the BA solution to the homogeneous 1D Hubbard model in the TD limit. However, the authors measured the power law exponent in a system for which it is unclear if the asymptotic low energy physics have set in. In particular, the influence of the finite size effects on the measured exponents is not illustrated. Therefore, in this thesis, we discuss the finite size effects in depth and employ a consistent

[13] Adibatic in this context implying that the ω dependence is ignored.

[14] Indicative of the fractionalization of excitation; see Ref. [Gia12].

[15] In this paper the XXZ Heisenberg spin chain in 1D is initially featured, but this model can be mapped to the the fermionic one as described in Chap. 3 and the fermionic charge densities is what is examined in Fig. 3 and 4 in Ref. [AC07].

methodology to achieve the high energy resolution required to reach the regime of the asymptotic density decay.

However, we focus on the one dimensional spinless fermion model rather than the Hubbard model in our work; see Sect. 5.1 and 5.3 for their definitions, respectively. The finite Hubbard model with open boundary conditions in 1D, due to the presence of the two-particle backscattering, is considered to have nontrivial low energy asymptotics. We discuss this issue in detail in Sect. 5.3.

Two main paradigm exist in efforts to tackle many-body problems such as the one of FO in 1D and the correlated LL physics. The *ab initio*[16] and the model Hamiltonian approach. The model Hamiltonian approach usually deals with simplified Hamiltonians with reduced degrees of freedom, and are designed to give a qualitative understanding of a specific mechanism or behavior present in nature. Examples of such models[17] within the condensed matter theory are the Ising, Heisenberg and the Hubbard model; see e.g. [Gia04] and [CC13]. On the other hand, the *ab initio* approach is typically used for quantitative calculation of certain material- or molecule-specific properties; see Ref. [DG90, Ull12]. A method is considered to belong to the *ab initio* class if dimensional constants and parameters appearing in it are fundamental constants of nature, such as: the electronic charge, Plank's constant, the proton charge and etc. DFT is usually applied to the *ab initio* Hamiltonians. However, in this thesis we will not use DFT in an *ab initio* sense and instead view it as just a many-body method for solving the model Hamiltonians; this was done before in e.g. Refs. [SDSE08, LSOC03, AC07].

In Chapter 2 we present a detailed introduction to the Matsubara Green's function formalism which we extensively use throughout our work. In Chapter 4 we show how the Matsubara formalism is used in DFT, and resulting in the formulation of the ODE DFT method. By using the ODE DFT approach to compute the density, we are able to treat large systems and thereby give a consistent interpretation of the low energy physics and FO for the LDA based on the BA. To benchmark the results and to build the LDA we use the BA equations derived in Chapter 3.

[16] Latin term for "from the beginning".
[17] Some previously mentioned.

In Chapter 5 we present our finite size LDA DFT results of different models and discuss how we infer FO asymptotics in the density data. In Chapter 7 we present our main results on the LDA DFT ability to described LL physics in the FO. Moreover, we discuss the Hartree-Fock results for the density in comparision to LDA DFT. In Chapter 6 we use the Matsubara Green's function formalism to get analytical insights from the Hartree-Fock approximation and discuss the special nature of half-filling in the spinless fermion model in respect to the density oscillation. This analysis provides explanations for the non-generic features[18] at half-filling and is relevant to any methodology that attempts to treat FO physics in this particular microscopic model.

We set the constants such as the $\hbar$ the electric charge e and k_B to 1 in this thesis unless otherwise stated.

[18] Not predicted by field theory.

2 Matsubara Green's function formalism

In this Chapter, we introduce the concepts and motivation behind the Matsubara Green's functions. After a short introduction to the topic in Sect. 2.1, we present the formalism for single-particle Hamiltonians and compute the Green's function for non-interacting fermions in Sect. 2.2. In Sect. 2.3 we discuss some equilibrium observables[1] in detail and particularities of their evaluation in Sect. 2.4. Finally, in Sect. 2.5 we derive an explicit expression for the reservoir self-energy, a quantity that takes into account an infinite non-interacting environment within the Matsubara formalism.

2.1 Introduction

Observables often take the form of Green's functions or they are directly derived from them in some way. Here, we shall introduce a more general class of Green's functions, the Matsubara Green's functions where the time and frequency are imaginary quantities ($it \to \tau$ and $\omega \to i\omega_n$). The Matsubara Green's functions are best suited for problems at a finite temperature and in equilibrium. The formalism is often easier to use than the usual zero temperature ones and contains the correct zero temperature physics as we set $T = 0$. The complexification of the arguments is a mathematical trick that is extremely useful when, for example, performing perturbation

[1] Those which are expressible in terms of Green's functions.

theory in the interaction and formulating the corresponding Feynman diagrams; see Ref. [BF04]. The single-particle Matsubara Green's functions[2], are defined

$$\begin{aligned} G_{\nu,\nu'}(\tau,\tau') &\equiv -\big\langle T_\tau\big[c_\nu(\tau)c^\dagger_{\nu'}(\tau')\big]\big\rangle \\ &= -\frac{1}{Z}\mathrm{Tr}\Big\{e^{-\beta H}T_\tau\big[c_\nu(\tau)c^\dagger_{\nu'}(\tau')\big]\Big\}, \end{aligned} \tag{2.1}$$

where ν, ν' are the quantum numbers, and $\beta = 1/T$. T_τ is the time-ordering operator, for the imaginary time τ, which orders the time arguments in such a way that the later times are stacked to the left

$$T_\tau\big[c_\nu(\tau)c^\dagger_{\nu'}(\tau')\big] = \theta(\tau-\tau')c_\nu(\tau)c^\dagger_{\nu'}(\tau') \pm \theta(\tau'-\tau)c^\dagger_{\nu'}(\tau')c_\nu(\tau). \tag{2.2}$$

The sign in front of the second term is a plus for bosons and minus for fermions. We note the following properties of Matsubara Green's functions:

i. $G_{\nu,\nu'}(\tau,\tau') = G_{\nu,\nu'}(\tau-\tau')$,

ii. $G_{\nu,\nu'}(\tau,\tau')$ converges iff $-\beta < \tau-\tau' < \beta$,

In particular, $\tau > \tau'$ in the second inequality $\tau-\tau' < \beta$ guarantees convergence (exponential decay) of the Matsubara Green's function. This becomes apparent if we use the Lehmann representation and the Heisenberg picture for the operators

$$\begin{aligned} G_{\nu,\nu'}(\tau,\tau') &= -Z^{-1}\mathrm{Tr}\Big[e^{-\beta H}e^{(\tau-\tau')H}c_\nu e^{-(\tau-\tau')H}c^\dagger_{\nu'}\Big] \\ &= -Z^{-1}\sum_{m,m'} e^{-E_m(\beta-\tau+\tau')}e^{(\tau'-\tau)E_{m'}} \\ &\quad\times \langle m|c_\nu|m'\rangle\langle m'|c^\dagger_{\nu'}|m\rangle. \end{aligned} \tag{2.3}$$

Similarly, the first inequality can be obtained if $\tau < \tau'$.

iii. $G_{\nu,\nu'}(\tau) = \pm G_{\nu,\nu'}(\tau+\beta)$ for $\tau < 0$ and $G_{\nu,\nu'}(\tau) = \pm G_{\nu,\nu'}(\tau-\beta)$ for $\tau > 0$.

[2]We work in the second quantization but suppress the typical hat operator notation for convenience.

Properties *i.* and *iii.* are consequences of the trace invariance under cyclic permutations. The Matsubara Green's function has the following Fourier transform in respect to the imaginary time τ as

$$G_{\nu,\nu'}(i\omega_n) = \int_0^\beta \mathrm{d}\tau e^{i\omega_n \tau} G_{\nu,\nu'}(\tau), \tag{2.4}$$

$$G_{\nu,\nu'}(\tau) = \frac{1}{\beta} \sum_{n=-\infty}^{\infty} e^{-i\omega_n \tau} G_{\nu,\nu'}(i\omega_n). \tag{2.5}$$

The frequencies read

$$\omega_n = \begin{cases} \dfrac{2n\pi}{\beta} & \text{for bosons,} \\ \dfrac{(2n+1)\pi}{\beta} & \text{for fermions.} \end{cases} \tag{2.6}$$

This means that the information about the particle statistics is encoded in the Matsubara frequencies ω_n. The Green's function is transformed from the $|\nu\rangle$ to the real-space $|j\rangle$ basis according to

$$G_{j,j'}(i\omega_n) = \sum_{\nu,\nu'} \langle j|\nu\rangle G_{\nu,\nu'}(i\omega_n) \langle \nu'|j'\rangle. \tag{2.7}$$

In the Lehmann representation[3],

$$G_{\nu,\nu'}(i\omega_n) = \sum_{mm'} \frac{\langle m|c_\nu|m'\rangle \langle m'|c_\nu^\dagger|m\rangle}{i\omega_n + E_m - E_{m'}} \left(e^{-\beta E_m} \mp e^{-\beta E_{m'}}\right), \tag{2.8}$$

it is easy to see that the Green's function coincides with the retarded and advanced Green's functions after analytical continuation $i\omega \to \omega \pm i\epsilon$, where ϵ is a positive infinitesimal[4]. The analytic continuation takes the series of poles at $E_{m'} - E_m$ from the imaginary axis to the real axis. The retarded (advanced) Green's functions can then be further used to compute physically relevant quantities such as the single-particle spectral function, the occupation, the charge current and others; see Ref. [Mah00].

[3] From Eq. 2.3 and 2.4.

[4] Plus sign for retarded, minus for advanced.

2.2 Single-particle formalism

Suppose that the fermionic non-interacting Hamiltonian H^0 is diagonal in the momentum $|\nu\rangle$ basis, which implies the following quadratic form

$$H^0 = \sum_\nu \xi_\nu c_\nu^\dagger c_\nu \tag{2.9}$$

We define the single-particle dispersion as $\xi_\nu = \varepsilon_\nu - \mu$, treating the problem in the grand canonical ensemble, with μ being the chemical potential and ε_ν the single-particle energies. The corresponding Matsubara Green's function is diagonal in $|\nu\rangle$ and reduces to

$$G^0_{\nu,\nu}(\tau,\tau') = G^0_{\nu,\nu'}(\tau,\tau')\delta_{\nu,\nu'}. \tag{2.10}$$

In the Heisenberg picture the operators decouple from their imaginary time arguments to yield $c_\nu(\tau) = e^{\tau H_0} c_\nu e^{-\tau H_0} = e^{-\xi_\nu \tau} c_\nu$ and $c_\nu^\dagger = e^{\tau H_0} c_\nu^\dagger e^{-\tau H_0} = e^{\xi_\nu \tau} c_\nu^\dagger$. In this representation, the Green's function reads

$$\begin{aligned} G^0_{\nu,\nu}(\tau,\tau') &= -\Big[\theta(\tau-\tau')\langle c_\nu c_\nu^\dagger\rangle - \theta(\tau'-\tau)\langle c_\nu^\dagger c_\nu\rangle\Big] e^{-\xi_\nu(\tau-\tau')} \\ &= -\Big[\theta(\tau-\tau')\big(1-n_{\mathrm{F}}(\xi_\nu)\big) - \theta(\tau'-\tau) n_{\mathrm{F}}(\xi_\nu)\Big] e^{\xi_\nu(\tau'-\tau)}, \end{aligned} \tag{2.11}$$

where $n_{\mathrm{F}}(\xi_\nu) = (e^{\beta\xi_\nu}+1)^{-1}$ is the usual Fermi-Dirac distribution. The Green's function in Eq. 2.11 is discontinuous across $\tau'' = \tau - \tau' = 0$. Notice, however, that $G^0_{\nu,\nu}$ has two different limits for $\tau'' \to 0^\pm$. In the frequency domain we have

$$\begin{aligned} G^0_{\nu,\nu}(i\omega_n) &= \int_0^\beta \mathrm{d}\tau'' e^{i\omega_n\tau''} G^0_{\nu,\nu}(\tau'') = -\big(1-n_{\mathrm{F}}\big)\int_0^\beta \mathrm{d}\tau e^{(i\omega_n-\xi_\nu)\tau''} \\ &= \frac{1}{i\omega_n - \xi_\nu}, \end{aligned} \tag{2.12}$$

where we used $e^{i\omega_n\beta} = -1$ and $1 - n_{\mathrm{F}}(\xi_\nu) = (e^{-\beta\xi_\nu}+1)^{-1}$.

2.3 Observables and zero temperature limit

The equilibrium expectation value for the single-particle occupation per site $j \in \mathbb{Z}^+$ can be directly computed from the Matsubara Green's function according to[5]

$$\langle n_j \rangle = \langle c_j^\dagger c_j \rangle = \frac{1}{\beta} \sum_{n=-\infty}^{\infty} e^{i\omega_n \eta} G_{j,j}(i\omega_n), \tag{2.14}$$

as $\eta \to 0^+$. The factor η is a regularization device to the logarithmically divergent sum[6]. This term effectively provides a cut-off to the slowly diverging sum and is sent to zero after the summation has been performed.

Given that we are usually interested in the zero temperature physics we take the $T \to 0$ limit first. At zero temperature there exists an infinite series of poles along the imaginary axis and the sum over the Matsubara frequencies turns into an integral

$$\begin{aligned} \lim_{T\to 0} \langle n_j \rangle = \lim_{\eta \to 0} \frac{1}{2\pi} \int_{-\infty}^{\infty} e^{i\omega\eta} G(i\omega) \mathrm{d}\omega = \frac{1}{2\pi} \Bigg[\lim_{\eta \to 0} \int_{-\infty}^{-M} e^{i\omega\eta} G(i\omega) \mathrm{d}\omega \\ + \int_{-M}^{0} G(i\omega) \mathrm{d}\omega + \int_{0}^{M} G(i\omega) \mathrm{d}\omega + \lim_{\eta \to 0} \int_{M}^{\infty} e^{i\omega\eta} G(i\omega) \mathrm{d}\omega \Bigg], \end{aligned} \tag{2.15}$$

where in the second equality we separated the integral into four which are bounded by M. We suppress the indices of the Green's function until the final expression. Furthermore, we omit the convergence

[5] The expression for the occupation trivially reduces to the second term in Eq. 2.11 by using Eq. 2.7 and the following identity

$$\lim_{\eta \to 0^+} T \sum_n \frac{e^{i\omega_n \eta}}{i\omega_n - x} = \frac{1}{e^{\beta x} + 1}, \tag{2.13}$$

in the example case of the tight-binding chain. For the derivation of the identity in Eq. 2.13 using contour integration see Ref. [FW03].

[6] In particular $\Sigma_{n=1}^{N} \frac{1}{n} \sim \ln(N)$ and in literature known as the harmonic series.

factor in the second an third integral because the integrals are convergent in $\big[-M, 0\big]$ and $\big[0, M\big]$ domains and together they amount to

$$\int_{-M}^{0} G(i\omega)\mathrm{d}\omega + \int_{0}^{M} G(i\omega)\mathrm{d}\omega = 2\int_{0}^{M} \mathrm{Re}\big[G(i\omega)\big]\mathrm{d}\omega. \tag{2.16}$$

The remaining two terms are explicitly evaluated using the fact that the Green's function scales[7] as $G(i\omega) \sim 1/i\omega$ for large ω. In particular

$$\lim_{\eta\to 0}\left[\int_{-\infty}^{-M} e^{i\omega\eta}G(i\omega)\mathrm{d}\omega + \int_{M}^{\infty} e^{i\omega\eta}G(i\omega)\mathrm{d}\omega\right] = \lim_{\eta\to 0} 2\int_{M}^{\infty} \frac{\sin(\omega\eta)}{\omega}\mathrm{d}\omega. \tag{2.17}$$

After using a simple variable transformation, $x = \omega\eta$, and performing the limit we obtain

$$2\int_{0}^{\infty} \frac{\sin(x)}{x}\mathrm{d}x = 2\int_{0}^{\infty}\mathrm{d}t\int_{0}^{\infty} e^{-xt}\sin(x)\mathrm{d}x = 2\int_{0}^{\infty}\frac{\mathrm{d}t}{1+t^2} = \pi. \tag{2.18}$$

Plugging the terms from Eqs. 2.16 and 2.18 into the expression for the equilibrium occupation in Eq. 2.15, we obtain for $M \to \infty$

$$\langle n_j\rangle = \frac{1}{2} + \frac{1}{\pi}\int_{0}^{\infty} \mathrm{Re}\big[G_{j,j}(i\omega)\big]\mathrm{d}\omega. \tag{2.19}$$

This expression for the occupation is convergent as the real part of the Matsubara Green's function scales as $1/\omega^2$ in the high-frequency limit. Within the Matsubara formalism it is also possible to compute the single-particle off-diagonal ($j \neq j'$) expectation values by using the off-diagonal Green's function according to

$$\langle c_j^\dagger c_{j'}\rangle = \frac{(-1)^{j'-j}}{\pi}\int_{0}^{\infty} \mathrm{Re}\big[G_{j,j'}(i\omega)\big]\mathrm{d}\omega, \quad \text{for} \quad j' > j \tag{2.20}$$

[7] See Eq. 2.12.

This integral, in contrast to the occupation when $j = j'$, converges and no special treatment is required[8]. This is due to the fast algebraic decay of the real part of the Matsubara Green's function as $1/\omega^{j'-j+1}$. As an illustration of how the Matsubara formalism is applied to a specific model, in Sect. 2.4, we present the calculations for a simple tight-binding chain.

2.4 Practical implementation and example

In this Section, we compute the occupation (density) per site of a tight-binding chain using the Matsubara Green's function formalism. We discuss different implementations within the formalism, their complexity and precision. An important role in these calculations is played by the chemical potential μ. Furthermore, we try to highlight the challenges in determining μ and discuss the advantages of using the Matsubara formalism for large lattices compared to the standard diagonalization.

In real-space the Hamiltonian of a tight-binding chain with hopping amplitude t is defined as

$$H^0 = -t \sum_{j=1}^{L-1} \left(c_{j+1}^\dagger c_j + \text{h.c.} \right). \tag{2.21}$$

We assume open boundary conditions (OBC) where the wave function is zero at the two auxiliary sites $j = 0$ and $j = L + 1$. The states have quantized momenta, $k_n = \frac{\pi n}{L+1}$, and it is trivial to diagonalize the Hamiltonian H^0 by going to Fourier space. In Fourier representation it is straightforward to obtain

$$n_j^0 = \langle c_j^\dagger c_j \rangle_0 = \frac{N + \frac{1}{2}}{L+1} - \frac{1}{2(L+1)} \frac{\sin\left[\frac{\pi j (2N+1)}{L+1}\right]}{\sin\left[\frac{\pi j}{L+1}\right]}, \tag{2.22}$$

for the tight-binding chain density for each j, and where N denotes the total number of fermions. With the explicit density at hand and serving as a benchmark for further numerical calculations, we

[8] Compared to the treatment of Eq. 2.14, leading to Eq. 2.19.

proceed to discuss the Matsubara approach; see inset of Fig. 2.1. The equilibrium occupation of the tight-binding chain at site $j = 1, 2, ..., L$ follows from Eq. 2.19 as

$$n_j^0 = \frac{1}{2} + \frac{1}{\pi} \int_0^\infty \mathrm{Re}\big[G_{j,j}^0(i\omega)\big] \mathrm{d}\omega. \tag{2.23}$$

The Green function G^0 can be understood as the resolvent matrix with elements

$$G_{j,j}^0(i\omega) = \langle j | \Big[\big(i\omega - \mu^0\big)\mathbb{I} - h^0 \Big]^{-1} | j \rangle, \tag{2.24}$$

where $\mathbb{I}$ denotes the identity matrix, and h^0 is the single-particle Hamiltonian of the tight-binding chain with Hilbert space of size L and reads

$$h^0 = -t \sum_{j=1}^{L-1} \Big(|j+1\rangle\langle j| + |j\rangle\langle j+1| \Big). \tag{2.25}$$

The single-particle basis is spanned by the set of states $\{|j\rangle\}$, where $|j\rangle$ denotes the Wannier state centered on real-space site j. Therefore, to evaluate the density we need to compute the resolvent which involves taking an inverse of a complex square matrix.

We now address the complete computational effort required to evaluate the density using Eq. 2.23. We distinguish the following computational steps:

- *Matrix inversion* of order $\mathcal{O}(L)$,

  With standard methods the inversion of a general complex matrix of size $L \times L$ can be accomplished in $\mathcal{O}(L^2)$ steps. However, the tight-binding Hamiltonian is a matrix operator of tridiagonal[9] structure and only the diagonal elements ($j = j'$) of the inverse $G_{j,j'}^0(i\omega)$ are required to compute the density.

[9] The Hamiltonian matrix is also tridiagonal in presence of local interactions that do not extend beyond the nearest-neighbor sites; e.g. Hartree-Fock Hamiltonian of the spinless fermion model in Eq. 5.1 or the Kohn-Sham Hamiltonian in Eq. 5.15.

These facts make the inversion possible in $\mathcal{O}(L)$ steps by an recursive scheme derived using the LDU decomposition. The explicit algorithm is described in Ref. [AEM+04] and leads to a computational speedup necessary to access larger chains. In Ref. [Kan12] an algorithm for the inversion of pentadiagonal[10] matrices, in a similar number of steps, is given.

- *Integral evaluation* of order $\mathcal{O}(I)$,

  After obtaining the Green's function the integral in the frequency ω needs to be solved. Lets denote I as the number of sampling instances necessary for a reliable approximation to the integral. This number does not scale with the system size and is practically a constant.

- *Fixing the chemical potential* of order $\mathcal{O}(B)$.

  The Green's function comes with the chemical potential μ which needs to be chosen such that the occupations sum to the total number of particles, $\sum_j n_j = N$. In the case of the tight-binding chain, which we currently consider, the chemical potential is explicitly known and reads[11] $\mu^0 = -2t\cos(\pi\nu)$. We use ν to denote the filling, defined as $\nu = N/L$. However, in presence of the two-particle interaction terms H^{int} in the Hamiltonian

  $$H = H^0 + H^{\text{int}}, \tag{2.26}$$

  which is typically approximated (for example using the self-consistent Hartree-Fock approximation) the chemical potential is *a priori* unknown and has to be determined empirically. To fix the chemical potential we use the bisection method. We denote the number of bisection steps as B. Furthermore, in the case of half-filling $\nu = 1/2$ the chemical potential is $\mu = 0$[12]; see Fig. 2.2. If the Hamiltonian in Eq. 2.26 is integrable, the

[10] For example in case of next-nearest-neighbor interaction or a five-point stencil representation of the second order kinetic operator in first quantization; e.g. the Hamiltonian in Eq. 5.18.

[11] This is the chemical potential of the continuum limit; see Fig. 2.2.

[12] This is also the case in presence of interaction is due to the particle-hole symmetry; see Sect. 3.5.

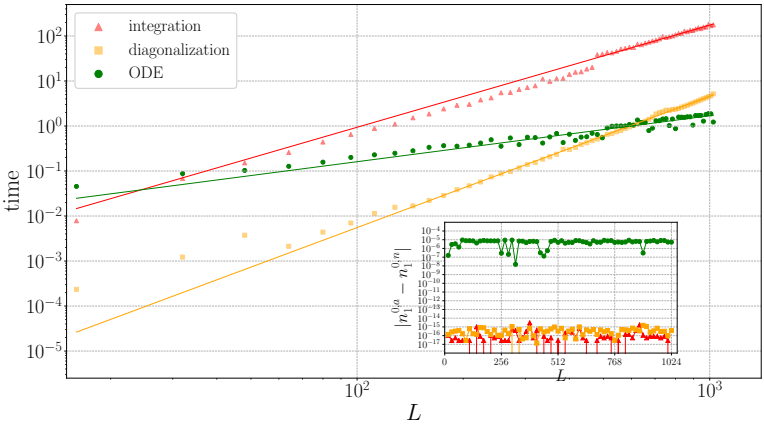

Figure 2.1: Execution times for the computation of the density on a typical single-core processor for all j over different system sizes L. The straight lines are fits to $f(L) = aL^b$. Empirically we find: for the integration $a = 2.703839 \cdot 10^{-5}, b = 2.269975$, for the exact diagonalization $a = 8.065386 \cdot 10^{-9}, b = 2.918336$ and for the ODE $a = 0.001459, b = 1.021339$. In the inset the precision $|n_1^{0,\mathrm{a}} - n_1^{0,\mathrm{n}}|$ is plotted, where $n_1^{0,\mathrm{n}}$ is the numerically computed density and $n_1^{0,\mathrm{a}}$ is the density from Eq. 2.22. We set $t = 1$ and use quarter filling $\nu = 1/4$. See text for further discussion.

chemical potential can be computed using Bethe ansatz; see Chap. 3.

Accounting for all the computational steps the total theoretical lower bound on the cost of evaluating the density via Eq. 2.23 for all $j \in \{1, 2, 3, ..., L\}$ is of the order $\mathcal{O}(IBL^2)$. However, in practice and using the common routines we identify the scaling $\mathcal{O}(L^{2.27})$ in executation times, consistent with the lower bound; see Fig. 2.1 and caption. With this method we are able to achieve machine precision similar to the exact diagonalization; see inset. For performing the diagonalization we used specialized routines that treat tridiagonal matrices and we were able to achieve scaling of $\mathcal{O}(L^{2.92})$. Beyond quadratic scaling of these two methods render them useless

for more than 10^4 site lattices without further optimizations and parallelization[13].

The main issue in the just described approach for solving Eq. 2.23 is that for each j we have to independently compute the inverse to evaluate the integral. The integration routines, for separate j's, sample the ω space differently in order to achieve the prescribed precision[14]. This is not the case anymore if we recast the expression for the density as a first order differential equation (ODE)

$$\frac{\mathrm{d}(n_j - 1/2)}{\mathrm{d}\omega} = \frac{1}{\pi}\mathrm{Re}\big[G_{j,j}(i\omega)\big], \quad n_j(0) = 0 \quad \text{for} \quad \forall j. \tag{2.27}$$

Simultaneously integrating this system of equations offers an efficient way to compute the density because for each ω we generate the complete RHS from the inverse only once, and the frequency sampling $\omega_1, \omega_2, ..., \omega_I$ is the same for all j's. This reduces the numerical cost by an order in L. The computation of the density now is linear in the lattice size, in particular $\mathcal{O}(IBL)$; see Fig. 2.1. This reduction in computational effort does not come without a price. The price is a significant loss in precision due to a finite number of steps we take to flow the frequency toward infinity[15] ($\omega \to \infty$). Nevertheless, for most practical purposes this is sufficient; see Sect. 5 and 7. The chemical potential in TD limit now provides only an approximation for the finite non-interacting system within the ODE approach as can be seen from the inset of Fig. 2.2. Looking at the intersection between the green line with the red offers only an approximation to the total particle number.

The Matsubara Green's function approach is applicable in general as long as we have a tridiagonal, pentadiagonal (and beyond) Hamiltonian matrix whose inverse can be evaluated efficiently. This is usually the case when we have open boundary conditions (OBC) or when coupling lattices with a noninteracting environment; see Sect. 2.5. With the ODE approach we can treat systems of 10^7 sites

[13] For a small number of particles the scaling is better, but in our particular applications we usually look at systems with filling of 1/4, 1/2 etc.

[14] For example at $j = 1$, the points that are sampled to evaluate the integral are $\omega_{1,1}, \omega_{1,2}, ..., \omega_{1,I}$ and those points might be different than $\omega_{2,1}, \omega_{2,2}, ..., \omega_{2,I}$ for $j = 2$.

[15] More elaborate integration schemes should in principle provide a better resolution and agreement with the diagonalization.

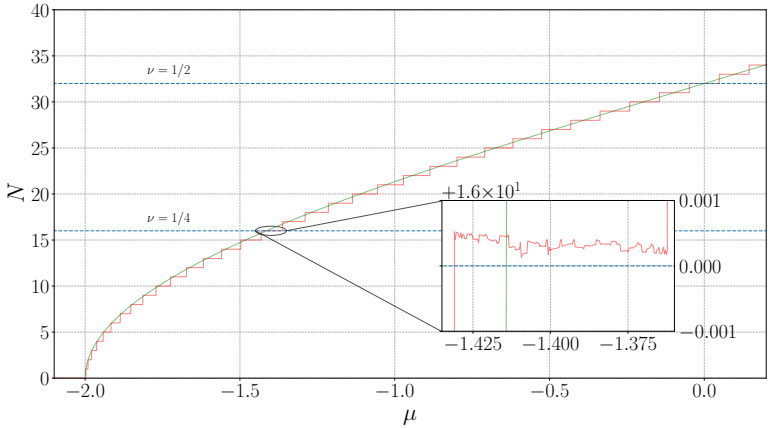

Figure 2.2: Landscape of the chemical potential of the finite tight-binding chain of size $L = 64$. The non-monotonic step-like behavior makes the search for the optimal μ non-trivial. Blue dashed lines represent the target particle number, N^{target}, in the total system with filling $\nu = N^{\text{target}}/L$. The green line is the continuum (TD) limit chemical potential $\mu^0 = -2\cos(\pi\nu)$.

while considering a large number of particles (quarter, half-filling etc.).

2.4.1 Determining the chemical potential

We now illustrate the challenges of determining the chemical potential within the ODE scheme on the example of the tight-binding chain. However, as we already mentioned, the chemical potential is explicitly known for this non-interacting model Hamiltonian[16]. Nevertheless, we use this model to elucidate the chemical potential landscape which is expected to be present in any finite system, with and without interactions.

The chemical potential is characterized by a step-like landscape

[16] Although, within the ODE scheme μ^0 offers only an approximation; see inset of Fig. 2.2.

as we change the particle number N; see Fig. 2.2. In the continuum (TD) limit the steps disappear and we have a monotonically increasing and continuous function. For finite systems the non-monotonic structure makes it difficult to obtain a good approximation for the chemical potential; see inset. Any search algorithm will eventually get stuck in some local minima, which is still not close enough to the target N^{target} (blue dashed line). This implies a finite precision in the total particle number and as mentioned before is a direct consequence of taking a finite number of steps to flow $\omega \to \infty$. Furthermore, with standard bisection algorithm we run the risk of getting stuck precisely at the discontinuity between the particle numbers, for example jumping between $N-1$ and N or N and $N+1$. This would not pose a problem if we were running the calculation to compute the density just once, where we can manually reinitialize the bisection from a more suitable point on the μ axis. However, in our work we typically perform self-consistent calculations[17] where multiple and consecutive iteration cycles over the density are required. For those particular applications we propose and use the following algorithm to determine the best possible chemical potential μ:

- *Phase I*: use standard bisection for a finite number of steps and record the total N at each step,
- *Phase II*: if we are stuck at a lower/higher step then the target one (happens if the bisection takes us near the discontinuity) start a new bisection routine after moving in μ space by $\pm a/L$,
- *Phase III*: select the case where $|N^{\text{target}} - N|$ is minimal from recorded steps from *Phase I* and *II*.

The parameter a in the second phase is determined empirically for each particular Hamiltonian[18] before running the computation for extremely large matrices, and the $1/L$ scaling is related to the energy level differences between available discrete states. Moreover, the search for μ in large systems can be accelerated by first narrowing down the possible μ range from smaller systems.

[17] Such as DFT or self-consistent Hartree-Fock calculations in Sect. 5.

[18] For example if we have interaction the landscape of the steps changes dramatically and a will be different from the one for a tight-binding chain.

2.5 Connecting an infinite environment to a finite lattice

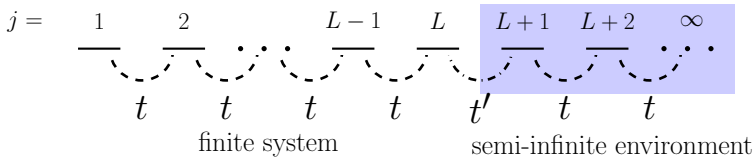

Figure 2.3: Sketch of a finite tight-binding chain with hopping t (Hamiltonian in Eq. 2.21) which we couple to a non-interacting semi-infinite reservoir via t'.

The Matsubara Green's function formalism is not limited to treating just finite systems. By attaching a reservoir[19] to finite systems, we effectively describe semi-infinite one; see Fig. 2.3. In this thesis, we are primarily interested in the effects of the boundary at $j = 0$. Therefore, by coupling the finite system to a single reservoir we aim to capture the boundary effects (e.g. in the density) such as the one of Friedel oscillations in a semi-infinite system.

We make use of the projection technique described in Ref. [Ens05] and matrix inversion recipe from Ref. [KSA+05] to treat such composite systems[20]. We split the Hilbert space of the total Hamiltonian into disjoint spaces with projection operators $P_L + P_\infty = 1$. P_L projects onto the Hilbert space of states in the finite system of size L with indices $j = 1, 2, .., L$, while P_∞ projects on sites $L+1, L+2, ..., \infty$. In block form the Hamiltonian then reads

$$h = \begin{pmatrix} h_{P_L P_L} & h_{P_L P_\infty} \\ h_{P_\infty P_L} & h_{P_\infty P_\infty} \end{pmatrix}. \tag{2.28}$$

[19] Which is modeled as a semi-infinite tight-binding chain.
[20] Finite system together with the reservoir on the right.

The explicit single-particle Hamiltonians read

$$h_{P_L P_L} = -t \sum_{j=1}^{L-1} \Big(|j+1\rangle\langle j| + |j\rangle\langle j+1| \Big) + h^{\text{int}} + h^{\text{imp}}, \tag{2.29}$$

where h^{int} denotes any interaction (two-particle) term decomposed in the single-particle basis and h^{imp} any impurity (single-particle) term present in the finite system. The remaining Hamiltonians are given as

$$h_{P_L P_\infty} = -t' |L\rangle\langle L+1|, \tag{2.30}$$

$$h_{P_\infty P_L} = -t' |L+1\rangle\langle L|, \tag{2.31}$$

$$h_{P_\infty P_\infty} = -t \sum_{j>L} \Big(|j+1\rangle\langle j| + |j\rangle\langle j+1| \Big). \tag{2.32}$$

The corresponding Matsubara Green's function is defined as

$$G := \frac{1}{(i\omega - \mu)\mathbb{I} - h} = \begin{pmatrix} G_{P_L P_L} & G_{P_L P_\infty} \\ G_{P_\infty P_L} & G_{P_\infty P_\infty} \end{pmatrix}, \tag{2.33}$$

where $\mathbb{I} = \mathbb{I}_{P_L} \otimes \mathbb{I}_{P_\infty}$ is the composite identity operator. We rewrite the Green's function in terms of the Dyson equation as

$$\frac{1}{\begin{pmatrix} A & B \\ C & D \end{pmatrix}} = \frac{1}{\begin{pmatrix} A & 0 \\ 0 & D \end{pmatrix}} - \frac{1}{\begin{pmatrix} A & 0 \\ 0 & D \end{pmatrix}} \begin{pmatrix} 0 & B \\ C & 0 \end{pmatrix} \frac{1}{\begin{pmatrix} A & B \\ C & D \end{pmatrix}}, \tag{2.34}$$

where for simplicity we denoted $A = (i\omega - \mu)\mathbb{I}_{P_L} - h_{P_L P_L}$, $B = h_{P_L P_\infty}$, $C = h_{P_\infty P_L}$ and $D = (i\omega - \mu)\mathbb{I}_{P_\infty} - h_{P_\infty P_\infty}$. From the Dyson equation we can directly read off the elements as

$$G_{P_L P_L} = P_L \frac{1}{(i\omega - \mu)\mathbb{I} - h} P_L = A^{-1} - A^{-1} B G_{P_\infty P_L}, \tag{2.35}$$

$$G_{P_L P_\infty} = P_L \frac{1}{(i\omega - \mu)\mathbb{I} - h} P_\infty = -A^{-1} B G_{P_\infty P_\infty}, \tag{2.36}$$

$$G_{P_\infty P_L} = P_\infty \frac{1}{(i\omega - \mu)\mathbb{I} - h} P_L = -D^{-1} C G_{P_L P_L}, \tag{2.37}$$

$$G_{P_\infty P_\infty} = P_\infty \frac{1}{(i\omega - \mu)\mathbb{I} - h} P_\infty = D^{-1} - D^{-1} C G_{P_L P_\infty}. \tag{2.38}$$

Plugging Eq. 2.37 into Eq. 2.35 we obtain

$$G_{P_L P_L} = \frac{1}{(i\omega - \mu)\mathbb{I}_{P_L} - h_{P_L P_L} - \Sigma_{P_L P_L}}, \tag{2.39}$$

where $\Sigma_{P_L P_L} = BD^{-1}C$ defines the reservoir self-energy. The reservoir self-energy takes the following form

$$\Sigma_{P_L P_L} = t'^2 |L\rangle\langle L+1|D^{-1}|L+1\rangle\langle L|, \tag{2.40}$$

and to compute it we have to evaluate the reservoir Green's function[21] at the interface site $L+1$. We start by writing the denominator in block form as

$$D = (i\omega - \mu)\mathbb{I}_{P_\infty} - h_{P_\infty P_\infty} = \begin{pmatrix} i\omega - \mu & \bar{t} \\ \bar{t}^T & D_1 \end{pmatrix}, \tag{2.41}$$

where $\bar{t} = \big[-t, 0, 0, ..., 0\big]$ is a row vector and D_1 is again a semi-infinite matrix reading

$$D_1 = \begin{pmatrix} i\omega - \mu & -t & 0 & ... \\ -t & i\omega - \mu & -t & ... \\ 0 & -t & i\omega - \mu & \\ \vdots & \vdots & \vdots & \ddots \end{pmatrix}. \tag{2.42}$$

We further denote the inverse of D as

$$D^{-1} = \begin{pmatrix} Q_{00} & \bar{Q}_{01} \\ \bar{Q}_{10} & Q_1 \end{pmatrix}. \tag{2.43}$$

Writing D^{-1} as a Dyson type equation as in Eq. 2.34 the matrix elements of the inverse follow immediately as

$$Q_{00} = (i\omega - \mu)^{-1} - (i\omega - \mu)^{-1}\bar{t}\bar{Q}_{10}, \tag{2.44}$$

$$\bar{Q}_{10} = -D_1^{-1}\bar{t}^T Q_{00}. \tag{2.45}$$

Plugging $\bar{Q}_{10}$ back into Q_{00} we obtain

$$Q_{00} = \frac{1}{i\omega - \mu - \bar{t}D_1^{-1}\bar{t}^T}. \tag{2.46}$$

[21] Which in nothing more than the resolvent $\Big[(i\omega - \mu)\mathbb{I}_{P_\infty} - h_{P_\infty P_\infty}\Big]^{-1}$.

By iterating we arrive at a semi-infinite continued fraction expression for the first element of the inverse matrix

$$Q_{00} = \cfrac{1}{i\omega - \mu - \cfrac{t^2}{i\omega - \mu - \cfrac{t^2}{\ddots}}}. \tag{2.47}$$

This particular continued fraction can be expressed as a second order polynomial

$$t^2 Q_{00}^2 - (i\omega - \mu) Q_{00} + 1 = 0, \tag{2.48}$$

which when solved gives two solutions for the reservoir Matsubara Green's function at the interface site

$$Q_{00} = \langle L+1| \frac{1}{(i\omega - \mu)\mathbb{I}_{P_\infty} - h_{P_\infty P_\infty}} |L+1\rangle \tag{2.49}$$

$$= \frac{i\omega - \mu}{2t^2} \left(1 \pm \sqrt{1 - \frac{4t^2}{(i\omega - \mu)^2}} \right). \tag{2.50}$$

The explicit formula for the reservoir self-energy in the finite system basis finally reads

$$\Sigma_{j,j'}(i\omega) = \frac{t'^2 (i\omega - \mu)}{2t^2} \left(1 - \sqrt{1 - \frac{4t^2}{(i\omega - \mu)^2}} \right) \delta_{j,L} \delta_{j,j'}, \tag{2.51}$$

where we selected the appropriate[22] solution out of the two in Eq. 2.50. The finite system Hamiltonian, in the presence of semi-infinite reservoirs, gets modified by Eq. 2.51 in the last diagonal element. The reservoirs are thought to be non-interacting and therefore in Eq. 2.51 $\mu \equiv \mu^0 = -2t \cos(\pi\nu)$.

[22] The one that offers a smooth transition to the semi-infinite environment.

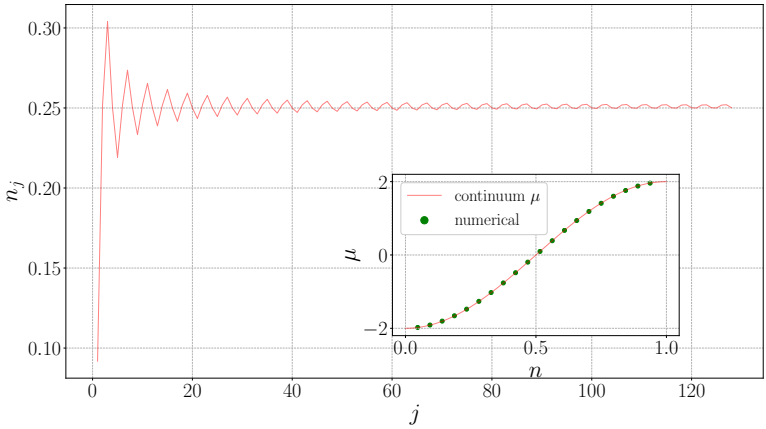

Figure 2.4: Density profile of the tight-binding chain at quarter filling $\nu = 1/4$ connected to a non-interacting reservoir on the right; see the sketch in Fig. 2.3. Inset: Chemical potential of a finite system $L = 128$ for different fillings connected to a single non-interacting lead to the right via Eq. 2.51. Red line is the continuum chemical potential of the tight-binding chain. We set $t = t' = 1$.

As an illustration, in Fig. 2.4 we plot the density profile in a clean semi-infinite non-interacting tight-binding chain[23] with the help of Eq. 2.51. The chemical potential, using the bisection algorithm in Sect. 2.4.1, is found to be in accordance with the continuum value μ^0, up to the precision available to the ODE Matsubara Green's function formalism; see inset.

[23] We assumed h^{int} and h^{imp} are not present in Eq. 2.29

3 Bethe ansatz approach

In this Chapter, we present a self-contained solution to the one-dimensional anisotropic spin-1/2 Heisenberg XXZ spin chain in the presence of an external magnetic field with periodic boundary conditions (PBC). The relevance of this particular spin model, within the context of this thesis, lies in the existence of an exact correspondence between this model and the spinless fermion model which is featured in our work and belongs to the Luttinger liquid universality class of models; see Sect. 5.1.

From a short introduction to the model in Sect. 3.1 we proceed to Sect. 3.2 where we apply the coordinate Bethe ansatz (BA) approach to the spin model and obtain the spectrum for a finite system of size L. Next in Sect. 3.3 we take the thermodynamic limit $L \to \infty$ and arrive at integral equations for the quantities relevant to the Luttinger liquid phenomenology. In Sect. 3.4 we discuss the numerical approach to solving these integral equations. The integral equations have closed form solutions in the zero magnetic field limit which are made explicit in Sect. 3.5. Finally in Sect. 3.6 we discuss an alternative approach to solving the set of BA integral equations. This alternative approach is useful for the purpose of building the approximation in Sect. 5.1.2.

3.1 Introduction

The anisotropic spin-1/2 Heisenberg XXZ spin chain is a microscopic model for magnetism. In one-dimension, in a particular parameter regime, it exhibits gapless excitations and belongs to the Luttinger liquid universality class. The low-energy behavior of the model in the LL regime, is described by a free bosonic field theory. In one dimension and in second quantization the chain is defined as

$$H = \sum_{j=1}^{L} \left[J_x \hat{S}_j^x \hat{S}_{j+1}^x + J_y \hat{S}_j^y \hat{S}_{j+1}^y + J_z \hat{S}_j^z \hat{S}_{j+1}^z + h \hat{S}_j^z \right]. \tag{3.1}$$

The spin operators $\hat{S}_j^\alpha$, at each site j, are related to the Pauli spin matrices as $\hat{S}_j^\alpha = \frac{1}{2}\hat{\sigma}_j^\alpha$. PBC are assumed, implying $\hat{S}_{j+L}^\alpha = \hat{S}_j^\alpha$ with $\alpha = x, y, z$. We choose the parameterization $J_x = J_y = J$, $J_z = J\Delta$. For $J < 0$ the ferromagnetic order is present in the $x - y$ plane and antiferromagnetic for $J > 0$. The parameter Δ controls the degree of anisotropy along the z direction. We differentiate between a planar $|\Delta| < 1$ and axial $|\Delta| > 1$ regimes. The planar regime is gapless and is described by Luttinger liquid phenomenology. The magnetic field strength h introduces a finite magnetization into the model. The complete phase diagram of the spin-1/2 Heisenberg XXZ spin chain is given in Ref. [Fra17].

The spin Hamiltonian in Eq. 3.1 can be mapped to a fermionic model with nearest-neighbor interactions via the Jordan-Wigner transformation, and by using the spin flip operators $\hat{S}_j^\pm = \hat{S}_j^x \pm i\hat{S}_j^y$. In particular,

$$\hat{S}_j^z \to \hat{c}_j^\dagger \hat{c}_j - \frac{1}{2}, \tag{3.2}$$

$$\hat{S}_j^+ \to \hat{c}_j^\dagger e^{i\pi \sum_{k=-\infty}^{j-1} \hat{c}_k^\dagger \hat{c}_k}. \tag{3.3}$$

leads to

$$
\begin{aligned}
H = & -\frac{1}{2}\sum_{j=1}^{L}\left(\hat{c}_j^\dagger \hat{c}_{j+1} + \hat{c}_j \hat{c}_{j+1}^\dagger\right) \\
& + \Delta \sum_{j=1}^{L}\left(\hat{c}_j^\dagger \hat{c}_j - \frac{1}{2}\right)\left(\hat{c}_{j+1}^\dagger \hat{c}_{j+1} - \frac{1}{2}\right) \\
& - h\sum_{j=1}^{L}\hat{c}_j^\dagger \hat{c}_j + \frac{h}{2}L. \qquad (3.4)
\end{aligned}
$$

This Hamiltonian is particle-hole symmetric $\hat{c}_j \to (-1)^j \hat{\tilde{c}}_j^\dagger$ only under the change of the direction of the field (chemical potential) $h \to -h$. The particle-hole symmetry corresponds to the spin reversal symmetry in the spin chain. In Sect. 6-7 we discuss some interesting consequences of this symmetry on the density. For the spin Hamiltonian, as we show in the next sections, an exact and complete solution is available via Bethe ansatz, and via Jordan-Wigner mapping these results extend to the fermionic model. However, before doing so we bring the Hamiltonian in Eq. 3.4 to a more familiar form and together with $U = 2\Delta$ obtain

$$
\begin{aligned}
H' &= 2H + UN - \frac{UL}{4} - 2hN + hL \\
&= -\sum_{j=1}^{L}\left(\hat{c}_j^\dagger \hat{c}_{j+1} + \hat{c}_j \hat{c}_{j+1}^\dagger\right) + U\sum_{j=1}^{L}\hat{c}_j^\dagger \hat{c}_j \hat{c}_{j+1}^\dagger \hat{c}_{j+1}. \qquad (3.5)
\end{aligned}
$$

In the following section, starting from a microscopic XXZ spin Hamiltonian we present the exact solution for the spectrum via coordinate Bethe ansatz method of the spin chain of size L in Eq. 3.1. From the derived expressions for finite systems we proceed to take the thermodynamic limit and compute interesting quantities in Sect. 3.3 and 3.4, respectively.

3.2 Bethe ansatz solution

We start by using the spin flip operators to rewrite the Hamiltonian to

$$H = J\sum_{j=1}^{L}\left[\frac{1}{2}\left(\hat{S}_j^+\hat{S}_{j+1}^- + \hat{S}_j^-\hat{S}_{j+1}^+\right) + \Delta\hat{S}_j^z\hat{S}_{j+1}^z\right] + h\sum_{j=1}^{L}\hat{S}_j^z. \quad (3.6)$$

H acts on a Hilbert space of dimension 2^L with orthogonal basis vectors $|\sigma_1...\sigma_L\rangle$, where $\sigma_j =\uparrow$ is the up spin and $\sigma_j =\downarrow$ a down spin at site j. The total magnetization in this model is conserved which enables us to consider separate sectors defined by the quantum number $S^z = L/2 - r$ where r is the number of down spins. We now rotate the spin operator by a phase angle π and thereby change the sign $\hat{S}_j^{x,y} \to (-1)^j\hat{S}_j^{x,y}$. Alongside the rotation we perform the inversion of the magnetic field $h \to -h$. These transformations leave the Hamiltonian unchanged and enable us to focus on sectors for which $0 \leq S^z \leq L/2$. The sector $r = 0$ has an eigenstate $|0\rangle = |\uparrow\uparrow ... \uparrow\rangle$ with all spins up which we take as the reference state. The reference state has the eigenenergy

$$e_0 = \frac{E_0}{L} = \frac{J\Delta}{4} - \frac{h}{2}. \quad (3.7)$$

The Bethe ansatz for unnormalized eigenstates of r down spins reads

$$|\Psi\rangle = \sum_{1\leq j_1<...<j_r\leq L} f(j_1, ..., j_r)|j_1, ..., j_r\rangle. \quad (3.8)$$

The states are defined with respect to the reference state as $|j_1, ..., j_r\rangle \equiv \hat{S}_{j_1}^-\hat{S}_{j_2}^-...\hat{S}_{j_r}^-|0\rangle$. The coefficients are given as

$$f(j_1, ..., j_r) = \sum_{\mathcal{P}}\exp\left[i\sum_{s=1}^{r}k_{\mathcal{P}_s}j_s + \frac{i}{2}\sum_{s<t}\tilde{\Theta}(k_{\mathcal{P}_s}, k_{\mathcal{P}_t})\right], \quad (3.9)$$

where the sum $\mathcal{P}$ is over all $r!$ permutations of labels $\{1, 2, ..., r\}$[1], and furthermore the phase shifts $\tilde{\Theta}$ are antisymmetric functions

[1] In Ref. [Gia04] and [KM98] for the case of $r = 2$ the explicit states are presented.

$\tilde{\Theta}(k_s, k_t) = -\tilde{\Theta}(k_t, k_s)$. Coefficients $f(j_1, j_2, ..., j_r)$ are subject to a set of consistency equations derived from the eigenvalue equation $\mathcal{H}|\Psi\rangle = E|\Psi\rangle$. The energy and total momenta are then derived to be

$$E = E_0 + \sum_{s=1}^{r} \Big[J(-\Delta - \cos k_s) + h \Big], \tag{3.10}$$

$$K = \sum_{s=1}^{r} k_s. \tag{3.11}$$

The scattering phases, due to consistency relations, take the form

$$\Theta(k, k') = 2 \arctan \frac{\Delta \sin\left(\frac{1}{2}(k - k')\right)}{\cos\left(\frac{1}{2}(k + k')\right) - \Delta \cos\left(\frac{1}{2}(k - k')\right)}, \tag{3.12}$$

where $\Theta(k, k') \equiv \tilde{\Theta}(k, k') - \pi$. Moreover, by using periodic boundary conditions[2] we arrive at the relation

$$e^{ik_s L} = \prod_{t \neq s} e^{i\tilde{\Theta}(k_s, k_t)} = (-1)^{r-1} \prod_{t \neq s} \frac{e^{k_s - k_t} + 1 - 2\Delta e^{ik_s}}{e^{k_s - k_t} + 1 - 2\Delta e^{ik_t}}. \tag{3.14}$$

From Eq. 3.14 we can read off the Bethe equations

$$k_s L = 2\pi \tilde{I}_s - \sum_{t \neq s} \Theta(k_s, k_t), \quad s = 1, 2, ..., r, \tag{3.15}$$

where $\{\tilde{I}_s\}$ is the set of integer/half-integer (depending if L is odd/even, respectively) quantum numbers describing the possible states $\tilde{I}_s \in \mathbb{Z}^+$ and $\tilde{I}_s \in \mathbb{Z}^+ + 1/2$, respectively. The Bethe equations are a set of r coupled algebraic equations in r unknowns and are solved numerically. By specifying the system size L, the number

[2] Eq. 3.12 and 3.14 can be shown to be equivalent by using the following identity

$$2i \arctan(z) = \ln\left[\frac{1 + iz}{1 - iz}\right]. \tag{3.13}$$

of down spins r and the anisotropy parameter Δ we are able to compute the quasi-momenta k_s which in turn determine all the eigenvalues and eigenstates of the model.

Having obtained the full spectrum of the finite system we now proceed to take the thermodynamic limit $L \to \infty$. However, before doing so, we introduce a parameterization for the quasi-momenta in terms of *rapidities* λ_s, as suggested in Ref. [Orb58]. This parameterization has the advantage of making the two-particle scattering phase translationally invariant and consequently makes the counting of possible states easier. The parameterization for $|\Delta| < 1$, where and the rapidities $-\infty < \lambda < \infty$, reads

$$\Delta = \cos\gamma \quad \text{for} \quad 0 < \gamma < \pi, \tag{3.16}$$

$$e^{ik} = -\frac{\sinh\left(\frac{1}{2}(\lambda - i\gamma)\right)}{\sinh\left(\frac{1}{2}(\lambda + i\gamma)\right)}, \tag{3.17}$$

$$e^{i\tilde{\Theta}(k,k')} = -\frac{\sinh\left(\frac{1}{2}(\lambda - \lambda' - 2i\gamma)\right)}{\sinh\left(\frac{1}{2}(\lambda - \lambda' + 2i\gamma)\right)}, \tag{3.18}$$

$$\theta_n = 2\arctan\left[\cot\left(\frac{n\gamma}{2}\right)\tanh\left(\frac{\lambda}{2}\right)\right]. \tag{3.19}$$

Consequently the Bethe equations take the following form

$$L\theta_1(\lambda_s) = 2\pi I_s + \sum_{t\neq s}\theta_2(\lambda_s - \lambda_t), \tag{3.20}$$

$$I_s = -\frac{L+1}{2} + s, \quad s = 1, 2, ..., r.$$

Furthermore, the total ground state energy and momentum are

$$E = E_0 + \sum_{s=1}^{r}\left[\frac{J\sin^2(\gamma)}{\cos(\gamma) - \cosh(\lambda)} + h\right], \tag{3.21}$$

$$K = \frac{2\pi}{L}\sum_{s=1}^{r} I_s. \tag{3.22}$$

To compute the total momentum we used that $k_s = \theta_1(\lambda_s)$ and that in Eq. 3.15 the scattering phase is an antisymmetric function.

The anisotropic spin-1/2 XXZ Heisenberg spin chain, as we have seen, maps onto the spinless fermion model with nearest-neighbor interactions. The interacting fermionic Hamiltonian in the low energy limit (linear spectrum) is quadratic when bosonized. In the bosonic representation the correlation functions can be accessed. The correlation function such as the density is parameterized by the Luttinger parameter K, and the finite-size ground-state energy by the central charge[3] c. In the next section we take the thermodynamic (TD) limit of the spin chain and derive expressions that can be used to evaluate the ground state energy which we use for building the approximation in Sect. 5.1.2. Furthermore, we compute the exact Luttinger parameter against which we benchmark the results of the microscopic model in Sect. 5-7.

3.3 The thermodynamic (TD) limit

In the TD limit $L \to \infty$ and $r \to \infty$ while the ratio between them is kept finite. To correctly take the limit it is necessary to define the quantity $x \equiv \frac{s}{L}$. The Bethe roots λ_s turn into function $\lambda(x)$ that depend on this newly defined continuous variable. The Bethe equations in the TD limit now read

$$\theta_1\Big(\lambda(x)\Big) = 2\pi x + \int \theta_2\Big(\lambda(x) - \lambda(y)\Big)\mathrm{d}y. \tag{3.23}$$

We avoid specifying the support of the integral for now and proceed to differentiate the expression with respect to $\lambda(x)$ to obtain

$$\frac{\mathrm{d}}{\mathrm{d}\lambda}\theta_1\Big(\lambda(x)\Big) = 2\pi\frac{\mathrm{d}x}{\mathrm{d}\lambda} + \int \frac{\mathrm{d}}{\mathrm{d}\lambda}\theta_2\Big(\lambda(x) - \lambda(y)\Big)\mathrm{d}y. \tag{3.24}$$

We further introduce the definition for the rapidity density as

$$\sigma(\lambda) \equiv \frac{\mathrm{d}x}{\mathrm{d}\lambda}, \tag{3.25}$$

[3] Without further details we note that the central charge for this model is $c = 1$ and belongs to the Luttinger universality class; see Ref. [Fra17].

and perform a change of variables to integrate over λ instead of x as

$$\int f\Big(\lambda(x)\Big)\mathrm{d}x = \int f(\lambda)\sigma(\lambda)\mathrm{d}\lambda. \tag{3.26}$$

The rapidity density is nothing but the Jacobian of the variable transformation. Finally, the TD limit of Eq. 3.20 reads

$$\sigma(\lambda) = \frac{1}{2\pi}K_1(\lambda) - \frac{1}{2\pi}\int_{-\Lambda}^{\Lambda} K_2(\lambda-\mu)\sigma(\mu)\mathrm{d}\mu, \tag{3.27}$$

with newly defined functions

$$K_1(\lambda) \equiv \frac{\mathrm{d}\theta_1}{\mathrm{d}\lambda} = \frac{\sin(\gamma)}{\cosh(\lambda)-\cos(\gamma)}, \tag{3.28}$$

$$K_2(\lambda) \equiv \frac{\mathrm{d}\theta_2}{\mathrm{d}\lambda} = \frac{\sin(2\gamma)}{\cosh(\lambda)-\cos(2\gamma)}. \tag{3.29}$$

Eq. 3.27 is an inhomogeneous Fredholm integral equation of the second kind for the rapidity density and is specified through the support Λ. The latter needs to be determined consistently from the successive minimization of the ground state energy with respect to the external field

$$\frac{\partial e}{\partial h} = 0 \quad \Leftrightarrow \quad \frac{\partial e}{\partial \Lambda} = 0. \tag{3.30}$$

Solving the integral equation for the rapidity can be viewed as an intermediate but essential step towards computing an observable like the ground state energy. The expression for the ground state energy per site follows directly from the TD limit of Eq. 3.21

$$e = e_0 + \int_{-\Lambda}^{\Lambda} \epsilon_0(\lambda)\sigma(\lambda)\mathrm{d}\lambda, \tag{3.31}$$

$$\epsilon_0 \equiv h + \frac{J\sin^2(\gamma)}{\cos(\gamma)-\cosh(\lambda)}. \tag{3.32}$$

The total magnetization per site is computed as

$$m = \frac{\langle \hat{S}^z \rangle}{L} = \frac{1}{2} - \int_{-\Lambda}^{\Lambda} \sigma(\lambda) \mathrm{d}\lambda, \tag{3.33}$$

where the integral over the rapidity density counts the number of down spins in the chain. The spin (or Fermi) velocity is defined as the derivative of the *dressed energy* with respect to the *dressed momentum*. In particular

$$v_s \equiv \left. \frac{\partial \epsilon(\lambda)}{\partial k(\lambda)} \right|_{\lambda=\Lambda} = \left. \frac{\partial \epsilon(\lambda)}{\partial \lambda} \frac{\partial \lambda}{\partial k(\lambda)} \right|_{\lambda=\Lambda}. \tag{3.34}$$

From Eq. 3.20 the dressed momentum follows

$$k(\lambda) = \theta_1(\lambda) - \int_{-\Lambda}^{\Lambda} \theta_2(\lambda - \mu)\sigma(\mu)\mathrm{d}\mu, \tag{3.35}$$

and is related to the rapidity density according to

$$\frac{\partial k(\lambda)}{\partial \lambda} = 2\pi\sigma(\lambda). \tag{3.36}$$

The dressed energy[4], reads

$$\epsilon(\lambda) = \epsilon_0(\lambda) - \frac{1}{2\pi} \int_{-\Lambda}^{\Lambda} K_2(\lambda - \mu)\epsilon(\mu)\mathrm{d}\mu. \tag{3.37}$$

Using the dressed energy it is possible to define the function $\rho(\mu)$ as

$$A \equiv \left. \frac{\partial \epsilon(\lambda)}{\partial \lambda} \right|_{\lambda=\Lambda} = \left. \frac{\partial \epsilon_0}{\partial \lambda} \right|_{\lambda=\Lambda} - \int_{-\Lambda}^{\Lambda} \epsilon_0(\mu)\rho(\mu)\mathrm{d}\mu, \tag{3.38}$$

$$\rho(\mu) = \left. \frac{1}{2\pi} \frac{\partial K_2(\lambda - \mu)}{\partial \lambda} \right|_{\lambda=\Lambda} - \frac{1}{2\pi} \int_{-\Lambda}^{\Lambda} K_2(\mu - \mu')\rho(\mu')\mathrm{d}\mu'. \tag{3.39}$$

[4] As introduced and explicitly derived in Ref. [Fra17].

After obtaining the support Λ, the integral Eq. 3.39 can readily be solved for the function $\rho(\mu)$. With this function obtained, A in Eq. 3.38 follows immediately and the spin (Fermi) velocity finally reads

$$v_s = \frac{A}{2\pi\sigma(\Lambda)}. \tag{3.40}$$

In the presence of an external field a useful auxiliary quantity, the *dressed charge* can be defined; see Ref. [KBI97]. This quantity enables the calculation of the Luttinger parameter, the conformal dimension of elementary excitations and offers an a posteriori verification of the precision of the numerical solutions by recomputing the magnetic field strength h via auxiliary functions; see Eq. 3.43. The integral equation for the dressed charge takes the form

$$Q(\lambda) = 1 - \frac{1}{2\pi}\int_{-\Lambda}^{\Lambda} K_2(\lambda-\mu)Q(\mu)\mathrm{d}\mu. \tag{3.41}$$

The Luttinger parameter is then given as

$$K = Q^2(\Lambda), \tag{3.42}$$

and the 'benchmark' relation reads

$$h(\Lambda) = 2\pi\sqrt{1-\Delta^2}\frac{\sigma(\Lambda)}{Q(\Lambda)}. \tag{3.43}$$

3.4 Numerical implementations

For a finite magnetic field, $h \neq 0$, the integral equations need to be solved numerically. Each value h corresponds to a particular magnetization per site m, ground state energy e, spin (Fermi) velocity and Luttinger parameter K. Initially, we use a simple bisection to solve Eq. 3.30, while simultaneously and iteratively (self-consistently) solving Eq. 3.27 for $\sigma(\lambda)$. The function $\sigma(\lambda)$ does not have an explicit form but only a numerical representation through a fixed number of points in the domain $\{-\Lambda, \Lambda\}$. We select to represent $\sigma(\lambda)$ on $10^3 + 1$ points, while linearly interpolating between each

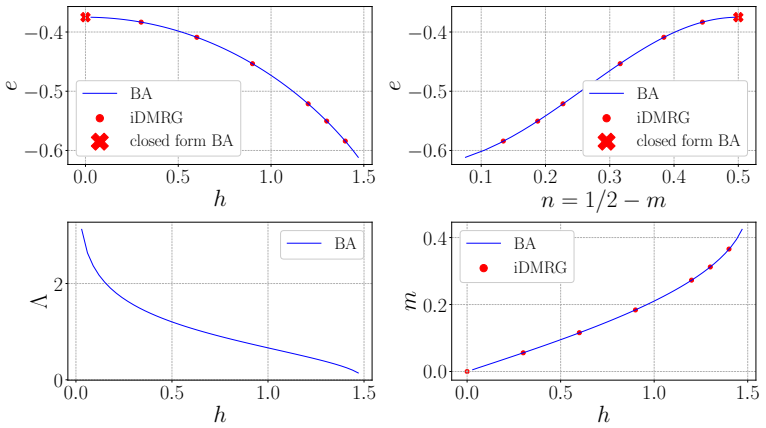

Figure 3.1: Bethe ansatz results for the ground state energy e, occupation $n = \frac{1}{2} - m$, support Λ and magnetization m compared against iDMRG from [Kar18] for $\Delta = 0.5$. The closed form solutions for $h = 0$ are presented in Sect. 3.5. The support $\Lambda \to \infty$ diverges as $h \to 0$.

two neighboring points to obtain a better approximation of the function and for usage in the integration routines. After obtaining the numerical approximation to the rapidity density and Λ, the spin velocity and Luttinger parameter follow immediately. Eq. 3.43, if the calculations are correctly performed, yield the same magnetic field h we inputed up to the numerical precision. From Fig. 3.2 (bottom plot) we can read off the precision to be at around 10^{-4} for most values of the magnetic field. However, the precision drops dramatically as we approach the $h \to 0$ limit because the integration domain diverges and the integration routines can only achieve a modest precision with a limited number of grid points. The main error in this calculation comes from the discrete representation of functions.

In Fig. 3.1 and 3.2 the results for the different quantities are presented, and they are consistent with the numerical infinite Density Matrix Renormalization Group (iDMRG) performed for the spin

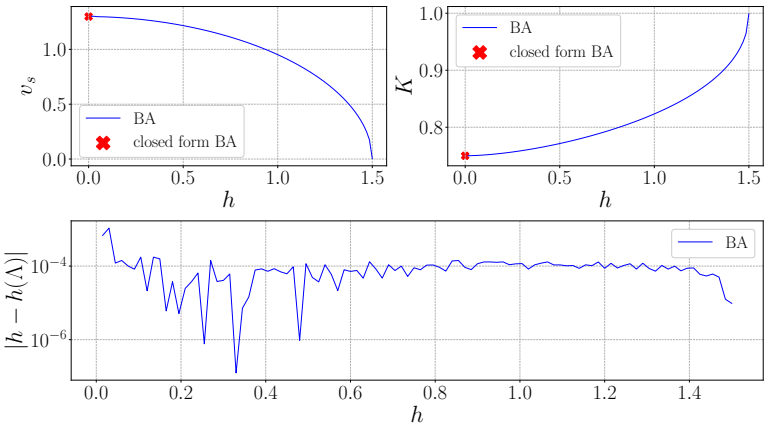

Figure 3.2: Top: Bethe ansatz solution for spin (Fermi) velocity v_s and Luttinger parameter K. Bottom: difference between inputed h and the 'benchmark' equation output Eq. 3.43.

Hamiltonian in Eq. 3.1; see Ref. [KM12] and [Sch11b, Vid07] for details on the method. We use the iDMRG data as a sanity check together with the closed form results at zero magnetic field in Sect. 3.5.

3.5 Zero magnetic field limit

In the case of vanishing external field, $h = 0$, the support diverges, i.e. $\Lambda \to \infty$. This enables the use of the Fourier transform to obtain an exact solution for:

- the rapidity density

$$\sigma(\lambda) = \frac{1}{4\gamma} \frac{1}{\cosh\left(\frac{\pi\lambda}{2\gamma}\right)}, \tag{3.44}$$

- the dressed momentum

$$k(\lambda) = \frac{\pi}{2} - \arctan\Big(\sinh\big(\frac{\pi\lambda}{2\gamma}\big)\Big), \tag{3.45}$$

- the dressed energy

$$\epsilon(\lambda) = \frac{J\pi}{2}\frac{\sin(\gamma)}{\gamma}\frac{1}{\cosh\left(\frac{\pi\lambda}{2\gamma}\right)}, \tag{3.46}$$

- the ground state energy per site

$$e = \frac{\Delta}{4} - \frac{\sin^2(\gamma)}{4\gamma}\int_{-\infty}^{\infty}\frac{\mathrm{d}\lambda}{\cosh\left(\frac{\pi\lambda}{2\gamma}\right)\Big(\cosh(\lambda) - \cos(\gamma)\Big)}, \tag{3.47}$$

- the spin (Fermi) velocity

$$v_s = \frac{\pi\sin(\gamma)}{2\gamma}, \tag{3.48}$$

- the magnetization per site

$$m = 0. \tag{3.49}$$

- the Luttinger parameter[5]

$$K = \frac{\pi}{2(\pi-\gamma)}. \tag{3.50}$$

These expressions are also valid for the fermionic model at half-filling $n = \frac{1}{2}$ due to the already described mapping in Sect. 3.1.

[5] Obtained perturbatively via the Wiener-Hopf method [KBI97].

3.6 Alternative approach

In Refs. [KBI97, QFY+97] an alternative approach to the energy minimization presented in Eq. 3.30 has been proposed. This approach is appropriate if the underlying Hamiltonian of interest is fermionic as the one in Eq. 3.5 rather than the spin Hamiltonian in Eq. 3.1. In particular, this approach allows us compute the ground state energy for a fixed density rather then a fixed magnetic field h value. This implies that the chemical potential has to be determined according to the condition

$$\epsilon(\pm\Lambda) = 0. \tag{3.51}$$

This condition reflects the fact that the model remain gapless in the paramagnetic (planar) $|\Delta| < 1$ regime; see Ref. [Fra17] for details. However, we approach to the computation of the chemical potential only after we determine the support Λ and the rapidity density $\sigma(\lambda)$ from the following equation

$$\int_{\Lambda}^{-\Lambda} \sigma(\lambda)\mathrm{d}\lambda = n. \tag{3.52}$$

Consequently, the ground state energy per site for the fermionic model[6] in the TD limit is computed as

$$e' = 2\int_{-\Lambda}^{\Lambda} \epsilon_0(\lambda)\sigma(\lambda)d\lambda + Un - 2\mu\nu, \tag{3.53}$$

where $\nu = N/L$ is the average density.

[6] In the fermionic model the external magnetic field h plays the role of the chemical potential μ.

4 Density Functional Theory

In this Chapter, we give a a short overview of the Density Functional Theory (DFT) method. DFT is based on the premise that the quantum many-body problem can be formulated in terms of the density as the main variable over the wave function. The success of the DFT method is linked to the ability to approximate the effects of the interaction in an efficient way. Over the years many different approximations have been formulated and are categorized according the the five rungs of the 'Jacob's ladder of DFT'[1] proposed by Perdew in Ref. [PS01]. With each rung the approximations produce more accurate results but their complexity increases as well. DFT is used in many branches of physics, chemistry and material science and is characterized by a low computational cost together with a significant degree of accuracy; see Ref. [Bur12] for a brief history of the method. However, in spite of enormous success in last decades, DFT is subject to many challenges when treating strongly correlated systems; see e.g. Ref. [WBS+14].

In Sect. 4.1 we present some general aspects of the DFT method and important facts on top of which this method is built. Next, in Sect. 4.2 we focus on a specific DFT formulation on the lattice. In Sect. 4.3 we discuss a practical scheme for the ground state (GS) DFT calculation, which can be considered an alternative to the usual *Aufbau* DFT approach.

[1] Jacob is a religious character, who dreamed of a ladder that extended to heaven.

4.1 Introduction

The ground-state DFT method relies on the Hohenberg-Kohn (HK) theorem which was originally introduced in Ref. [HK64]. Without explicitly stating the theorem we discuss one extremely important consequence namely that all observables are functionals of the ground state (GS) density. The GS energy, in particular, reads

$$E[n] = T[n] + V[n] + W[n], \tag{4.1}$$

where T is the kinetic energy, V represents all the single-particle potentials (e.g. ionic lattice electrostatic potentials in a solid) and W is the two-particle interaction term (e.g. Coulomb electron-electron interaction). All are functionals of the density. The universal part of the energy is

$$F[n] = T[n] + W[n], \tag{4.2}$$

implying that $F[n]$ is identical for all systems with the same interaction. The Kohn-Sham (KS) DFT scheme relies on rewriting Eq. 4.1 as[2]

$$\begin{aligned} E[n] &= T^{\mathrm{S}}[n] + \Big(T[n] - T^{\mathrm{S}}[n]\Big) + V[n] + E^{\mathrm{H}}[n] \\ &\quad + \Big(W[n] - E^{\mathrm{H}}[n]\Big), \\ &= T^{\mathrm{S}}[n] + V[n] + E^{\mathrm{H}}[n] + E^{\mathrm{XC}}[n], \end{aligned} \tag{4.3}$$

with $E^{\mathrm{XC}} = W^{\mathrm{XC}} + T^{\mathrm{C}}$, $T^{\mathrm{C}} = T - T^{\mathrm{S}}$ and $W^{\mathrm{XC}} = W - E^{\mathrm{H}}$, where E^{H} denotes the usual mean-field Hartree energy; see Ref. [KS65]. The T^{C} term contains the many-body correction to the kinetic energy and the corrections to the two-body interaction are encoded in W^{XC}. Within the DFT scheme the exchange-correlation energy E^{XC} is approximated, and in this thesis we focus on the Local Density Approximation (LDA) for the exchange-correlation energy; see Sect. 5.1.2 and 5.2 for two explicit examples.

[2] In order to remain consistent throughout the thesis we use the unconventional upper indices.

Minimization condition of energy w.r.t. the density,

$$\left.\frac{\delta E[n]}{\delta n(\mathbf{r})}\right|_{n=n^{\mathrm{GS}}} = 0, \tag{4.4}$$

leads us to the single-particle Schrödinger equation

$$H^{\mathrm{KS}}\psi_i(\mathbf{r}) = \epsilon_i\psi_i(\mathbf{r}), \tag{4.5}$$

where the KS Hamiltonian takes the form

$$H^{\mathrm{KS}} = -\frac{\bigtriangledown^2}{2} + V(\mathbf{r}) + V^{\mathrm{H}}(\mathbf{r}) + V^{\mathrm{XC}}(\mathbf{r}). \tag{4.6}$$

Eq. 4.5 when solved supplies the orbitals that determine the density according to

$$n(\mathbf{r}) = \sum_{i=1}^{N} \left|\psi_i(\mathbf{r})\right|^2. \tag{4.7}$$

The potentials in Eq. 4.5 are the functional derivatives of the corresponding energies $V^H(\mathbf{r}) = \frac{\delta E^{\mathrm{H}}}{\delta n(\mathbf{r})}$, $V^{\mathrm{XC}}(\mathbf{r}) = \frac{\delta E^{\mathrm{XC}}}{\delta n(\mathbf{r})}$ and $V(\mathbf{r}) = \frac{\delta V}{\delta n(\mathbf{r})}$. The KS Eq. 4.5 models a non-interacting system in an effective single-particle potential $V^{\mathrm{eff.}}(\mathbf{r}) = V(\mathbf{r}) + V^{\mathrm{H}}(\mathbf{r}) + V^{\mathrm{XC}}(\mathbf{r})$.

The KS scheme implies a minimization w.r.t. the density. In the DFT literature this minimization is known as the *self-consistent field* (SCF) method and the variational steps are labeled as SCF steps. Practically, this kind of procedure employs a non-interacting auxiliary system with the same as the interacting system. The density is, according to the conventional *Aufbau*[3] principle, constructed from the N lowest occupied single-particles orbitals as given by Eq. 4.7.

According to the HK theorem the density of the fictitious KS system and the interacting many-body system are equivalent. On the other hand, quantities such as the KS orbitals and energies do not have this interpretation. Nevertheless, in the literature, there have been multiple examples where these quantities have been interpreted

[3]Germany term for 'constructed' or 'construction'.

as such with different degrees of success; see Ref. [CC13] and [Ull12] and references therein. The only well-defined observables within a DFT scheme are the charge density[4] and the total GS energy. All observables are formally considered a functional of the density, but very few[5] have an explicit relation to it.

In a typical mean-field treatment the fluctuations are neglected and any difference between the exact and the mean-field is considered as *correlations*. By construction in Eq. 4.3, any non-vanishing exchange-correlation energy functional E^{XC} constitutes a beyond-mean-field approximation. The *exchange* part is exactly known as a functional of the KS orbitals. However, usually the exchange and correlation contributions to the energy are approximated together such that one profits from error cancellation effects.

In the following Section we review a particular DFT formulation suitable for model Hamiltonians defined in second quantization language. Some model Hamiltonians are readily solved by a diverse set of methods[6], making this basis the ideal laboratory for the study of the strongly correlated physics, and in particular the Luttinger liquid physics; see Chap. 1.

4.2 The lattice DFT method

There exist many formulations of the DFT method on the lattice and each has a different local property as the basic variable; see Ref. [CC13] for an overview of the different formulations. For every formulation the HK theorem can be shown to hold. In this thesis, we adopt the one which makes use of the site occupation (local density), $n_j = \langle c_j^\dagger c_j \rangle$ with $j \in \mathbb{Z}^+$, as the basic variable. We consider $c_j^\dagger$ and c_j as creation and annihilation operators in second quantization at site j, respectively. In the literature this is known as the *site-occupation functional theory* (SOFT); see Ref. [GS86]. Within the

[4] As well as the spin and current density for the extended spin- and current-DFT formalisms.

[5] Such as the dipole moment.

[6] For example, the Bethe ansatz solution to the 1D Heisenberg XXZ chain in Sect. 3

SOFT formalism the KS Hamiltonian reads

$$H^{\mathrm{KS}}[\{n_j\}] = -t \sum_{\langle i,j \rangle} \left(c_i^\dagger c_j + \mathrm{h.c.} \right) + \sum_j v_j^{\mathrm{eff.}}[\{n_j\}] c_j^\dagger c_j, \tag{4.8}$$

where $\langle i, j \rangle$ refers to first neighbors, $\{n_j\}$ denotes a set of densities of each lattice site j, and the effective potential is defined as

$$v_j^{\mathrm{eff.}}[\{n_j\}] = v_j + v_j^{\mathrm{H}}[\{n_j\}] + v_j^{\mathrm{XC}}[\{n_j\}]. \tag{4.9}$$

We purposely avoided to capitalize the potentials to indicate the different basis we use compared to standard formulations in Sect. 4.1. The ground-state KS density is computed from the single-particle Schrödinger equation

$$H^{\mathrm{KS}}[\{n_j\}] \psi_{i,j} = \epsilon_i \psi_{i,j}, \tag{4.10}$$

by summing the squares of the lowest N occupied orbitals,

$$n_j = \sum_{i=1}^{N} \left| \psi_{i,j} \right|^2. \tag{4.11}$$

The HK theorem ensures a one-to-one correspondence between $v^{\mathrm{eff.}}[n_j]$ and n_j, and according to Eq. 4.10 the KS states are functionals of the density, $\psi_{i,j}[n_j]$. The exchange-correlation potential v_j^{XC} in Eq. 4.9 depends exclusively on the local density n_j on site j and is *a priori* unknown, and therefore has to be approximated.

Furthermore, in SOFT formalism quantities become functions of the variables n_j, as opposed to functionals in the traditional formulation. The additional benefit of a lattice DFT formulation is that the ground state is actually v-representable[7] as shown in Ref. [CCR85]. In *ab initio* applications of the DFT method v-representability is considered an extremely difficult statement to prove.

[7] The requirement that the ground state density belong to some external potential; see Ref. [Ull12] for more details.

4.3 The ODE DFT method

In contrast to the usual *Aufbau* principle, in this thesis we employ the Matsubara Green's function formalism from Sect. 2 to compute the density. The Matsubara formalism enables the computation of the GS density without any reference to the eigenstates. To obtain the explicit density we replace the already efficient diagonalization of the KS non-interacting system with a matrix inversions of the KS Hamiltonian matrix. By performing the inversion one can compute the Matsubara Green's function which defines the system of first order differential equations (ODEs), which we then have to solve for the density. This formulations is extremely efficient if the Hamiltonian matrix is tridiagonal[8].

At zero temperature the set of differential equations from Eq. 2.27 in Matsubara frequencies ω for a DFT calculation of a lattice model KS Hamiltonian in Eq. 4.8 reads

$$\frac{\mathrm{d}(n_j - 1/2)}{\mathrm{d}\omega} = \frac{1}{\pi}\mathrm{Re}\Big[G^{\mathrm{KS}}_{j,j}(i\omega)[\{n_j\}]\Big], \tag{4.12}$$

with the initial conditions

$$n_j(0) = 0, \quad \text{for} \quad j = 1, 2, ..., L. \tag{4.13}$$

The Matsubara Green's function is defined as

$$G^{\mathrm{KS}}_{j,j}(i\omega)[\{n_j\}] = \langle j|\Big[(i\omega - \mu)\mathbb{I} - h^{\mathrm{KS}}[\{n_j\}]\Big]^{-1}|j\rangle, \tag{4.14}$$

where $\mathbb{I}$ denotes the identity matrix, h^{KS} is defined in the basis of Wannier states $\{|j\rangle\}$ centered on the lattice site j, and μ the chemical potential; see Chap. 2.

We denote this particular way for the computation of the density as the ODE DFT method or scheme. The advantages of this computational scheme have already been pointed out in Sect. 2.4 on the example of a simple tight-binding chain. The same features of this method apply to the DFT scheme but for the DFT calculation the additional SCF cycles are necessary to converge the density. The

[8] As well as pentadiagonal and beyond; see Chap. 2.

precision of the density computation offered with this method is sufficient such that the usual convergence criterion $\sum_j |n_j^{\text{inp}} - n_j^{\text{out}}| < \epsilon$, where n_j^{inp} is the input and n_j^{out} the output densities per site of the SCF step with $\epsilon = 10^{-5}$, can be employed.

The ODE DFT scheme enables us to access large lattice systems with OBC[9] as can be seen in Sect. 7. Furthermore, this scheme offers a natural way to treat transport setups. For example, using the ODE DFT scheme we were able to quite efficiently reproduce the findings in Ref. [SSDE11], where two non-interacting wide-band reservoirs are attached at the ends of the finite interacting chain.

The ODE DFT scheme can potentially be used for *ab initio* KS Hamiltonians with OBC in first quantization where the kinetic energy operator is approximated, for example, with centered difference (tridiagonal Hamiltonian matrix) or the five-point stencil rule (pentadiagonal). Furthermore, using the Galitskii-Migdal formula, the GS energy can be computed from the Matsubara Green's function; see Ref. [SL13]. However, the usefulness of this formula within the DFT method with accompanying approximations is still an open question and requires further research efforts.

Any orbital dependent approximation (e.g. exact-exchange) can not be treated with the ODE DFT approach because of the lack of access to the eigenstates. On the other hand, approximations such as the LDA and various generalized gradient approximations (GGAs) are suitable for this method. In particular, LDA exclusively requires the knowledge of the local density, while GGA needs the density and its gradient (first derivative in respect to the coordinate). Therefore, the scheme can be applied to approximation up to, and not including the third rung of 'Jacob's ladder'.

[9]The systems with periodic boundary conditions (PBC) can not be treated efficiently with this scheme because the Hamiltonian matrix is not tridiagonal.

5 Friedel oscillations in finite systems

In this Chapter, we present the results for the charge density coming out of DFT calculations employing the LDA in one dimension. Universality of the LL paradigm in 1D allows us to focus on specific models and expect that certain features are in accordance with the predictions from field theory. In particular, the rate of the decay of the Friedel oscillations in the density away from boundaries or impurities from the DFT calculation, should match the BA prediction if LDA is truly able to captures LL physics.

In Sect. 5.1 we focus on the spinless fermion model with nearest-neighbor interactions on the lattice and compare the results for the density to the numerically exact DMRG and the Hartree-Fock (HF) approximation . In Sect. 5.2 we step away from the lattice and discuss spinless fermions with long-range interaction in first quantization in real-space. In both of the sections we discuss the ability of LDA DFT to resolve the decay of Friedel oscillations in systems with open boundary conditions (OBC). Results for LL's with OBC are crucial to understand LL's with a local inhomogeneity. Such systems scale to chains with OBC as described in Ref. [KF92]. Finally, in Sect. 5.3 we shortly discuss the Friedel oscillation within the Hubbard model.

5.1 Short-range interaction on a lattice

We consider the spinless fermion model (SFM) with nearest-neighbor interaction with OBC in second quantization. The Hamiltonian of this model is defined as

$$H = -t \sum_{j=1}^{L-1} \left(c_{j+1}^\dagger c_j + c_j^\dagger c_{j+1} \right) + U \sum_{j=1}^{L-1} n_j n_{j+1}, \tag{5.1}$$

where t and U are the nearest-neighbor hopping and interaction amplitudes, respectively. We use the common second quantization notation, where $c_j^\dagger$ (c_j) denotes the creation (annihilation) operator and $n_j = c_j^\dagger c_j$ the local charge density operator of site j. The presence of the boundaries[1] induces the characteristic Friedel oscillation with $2k_\mathrm{F}$ periodicity, where k_F is the Fermi momentum. The interplay between the Fermi surface[2] effects and two-particle interaction modifies the decay rates of the oscillations away from the localized perturbation and into the bulk.

From the bosonization approach in Ref. [EG95], it is known that in the presence of local interaction the oscillations decay algebraically away from a boundary as

$$\delta n^B(x) = n^B(x) - \nu = -\frac{\sin\left(2k_\mathrm{F} x\right)}{2\pi x^K}, \tag{5.2}$$

where δn^B is a function of the continuous variable x and represents the deviation of the electron density away from average filling ν of the system. K is the universal Luttinger parameter which is a non-trivial function of the interaction strength, the filling and the single-particle dispersion; see Sect. 3.3. The boundary can be viewed as an infinitely strong impurity, through which particles can not tunnel. In case of weak impurities a slower decay is expected of the form x^{1-2K} close to the impurity but at long-distances the asymptotic boundary like decay x^{-K} is recovered. For spin-1/2 electrons[3] the Friedel oscillation term at $2k_\mathrm{F}$ is not the only oscillation mode present

[1] Also any localized perturbation such as an impurity.
[2] In one-dimensional systems the surface is just two points.
[3] Which are not discussed in this thesis; see Sect. 5.3.

in the density. In fact, there exists a mode with $4k_F$ periodicity, known as the Wigner component. For extremely strong interaction ($K < 1/3$) this component dominates over the Friedel $2k_F$ decay.

The SFM displays LL features at half-filing for $|U|/t < 2$, and away from half-filling for all $U/t > -2$; see Ref. [Hal80]. At half-filling and for $U/t > 2$ (repulsive interaction) a charge density wave (CDW) forms while for $U/t < -2$ (attractive interaction) the system exhibits a phase separation. For repulsive interactions the Luttinger parameter is $K < 1$ while for attractive $K > 1$; see Sect. 3.3. If the system is non-interacting then $K = 1$. By taking the thermodynamic limit ($L \to \infty$) in Eq. 2.22 we obtain the asymptotic decay of the Friedel oscillations in case of non-interacting fermions, i.e. $U = 0$, for the SF model to be j^{-1} and consistent with $K = 1$.

We have already seen in Sect. 3 that the SF model with PBC is integrable. Under the assumption of conformal invariance in the gapless regime, the n-point correlation functions of the OBC systems are related to the $2n$-point correlation functions of PBC systems; see Ref. [Car84]. This means that the asymptotic power-law decay of the density in Eq. 5.2 is exactly known with the explicit computation of the Luttinger parameter from Sect. 3.3. Other quantities, such as the central charge and conformal dimension, follow from the finite-size corrections[4] to the ground state energy; see Ref. [Fra17] and [WVP96].

Going further, we discuss the possibility to resolve the anticipated asymptotic power-law decay of the density in the microscopic single-particle LDA DFT calculations. We benchmark this kind of approach against exact results and other methods in strongly correlated LL regimes. One immediate advantage and motivation to use DFT is the low computational cost that comes from solving a non-interacting problem in an effective potential instead of solving the full interacting problem; see Sect. 4.

In our work, we exclusively use the Matsubara Green's function to obtain the density. In the following, we present the exact derivation of non-interacting density of the spinless fermion model in Eq. 5.1 using this formalism.

[4] Computed via BA as well.

5.1.1 Non-interacting ground state density

We compute the non-interacting density of the spinless fermion model at site j, where $j \in \{1, 2, ..., L\}$, from the Matsubara Green's function in Eq. 2.23 as

$$n_j^0 = \langle \hat{c}_j^\dagger \hat{c}_j \rangle_0 = \frac{1}{2} + \frac{1}{\pi} \int_0^\infty d\omega \mathrm{Re}\big[G_{j,j}^0(i\omega)\big], \tag{5.3}$$

and by decomposing the Matsubara Green's function matrix in the open boundary condition (OBC) momentum basis

$$G_{j,j}^0(i\omega) = \sum_{n,n'=1}^{L} \langle j|n\rangle \langle n'|j\rangle G_{n,n'}^0(i\omega). \tag{5.4}$$

The normalized single-particle OBC eigenstates $\langle j|n\rangle = \varphi_n(j)$ and $\langle n'|j\rangle = \varphi_{n'}^*(j)$ are given by

$$\varphi_n(j) = \sqrt{\frac{2}{L+1}} \sin(k_n j), \qquad k_n = \frac{n\pi}{(L+1)}, \qquad n \in \{1, 2, ..., L\}. \tag{5.5}$$

Using this decomposition we can write the density as

$$n_j^0 = \frac{1}{2} + \frac{2}{\pi(L+1)} \int_0^\infty d\omega \mathrm{Re} \sum_{n,n'=1}^{L} \sin(k_n j) \sin(k_{n'} j) G_{n,n'}^0(i\omega). \tag{5.6}$$

Due to the Green's function matrix being diagonal the density expression takes the form

$$n_j^0 = \frac{1}{2} + \frac{1}{\pi(L+1)} \int_0^\infty d\omega \mathrm{Re} \sum_{n=1} \left(\frac{1}{i\omega - \xi(k_n)} - \frac{\cos(2k_n j)}{i\omega - \xi(k_n)} \right). \tag{5.7}$$

We exchange the order of the sum and the integral and illustrate further computations by focusing on the second term[5]

$$\int_0^\infty d\omega \mathrm{Re} \sum_{n=1}^{L} \frac{\cos(2k_n j)}{i\omega - \xi(k_n)} = -\sum_{n=1}^{L} \xi(k_n) \cos(2k_n j) \int_0^\infty d\omega \frac{1}{\omega^2 + \xi^2(k_n)} = -\sum_{n=1}^{L} \cos(2k_n j) \arctan\left(\frac{\omega}{\xi(k_n)}\right)\Bigg|_0^\infty . \tag{5.8}$$

Evaluating the arctan gives $-\frac{\pi}{2}$ and $+\frac{\pi}{2}$ depending on the sign of the dispersion $\xi(k_n)$, below the Fermi level we have $\xi(k_n) < 0$ and above $\xi(k_n) > 0$. Some of the contributions within the sum cancel each other leaving a finite number of contributing terms. We define $\tau = 1/\nu$ and use it to specify (for a particular filling) which terms contribute in Eq. 5.8 as

$$\int_0^\infty d\omega \mathrm{Re} \sum_{n=1}^{L} \frac{\cos(2k_n j)}{i\omega - \xi(k_n)} = -\frac{\pi}{2} \sum_{n=N+1}^{N(\tau-1)} \cos(2k_n j). \tag{5.9}$$

In case of half-filling contributions from above and below the Fermi level completely cancel, and there is no summation in Eq. 5.9. However, away from half-filling, to evaluate this sum we use the geometric series[6] and find

$$n_j^0 = \frac{1}{2} - \frac{N(\tau-2)}{2(L+1)} + \frac{1}{2(L+1)} \frac{\cos(\pi j) \sin\left[\frac{N\pi j}{L+1}(\tau-2)\right]}{\sin\left[\frac{\pi j}{L+1}\right]}, \tag{5.10}$$

[5] The first term follows trivially.

[6] In particular, $\sum_{k=a}^{b} r^k = \frac{r^a - r^{b+1}}{1-r}$.

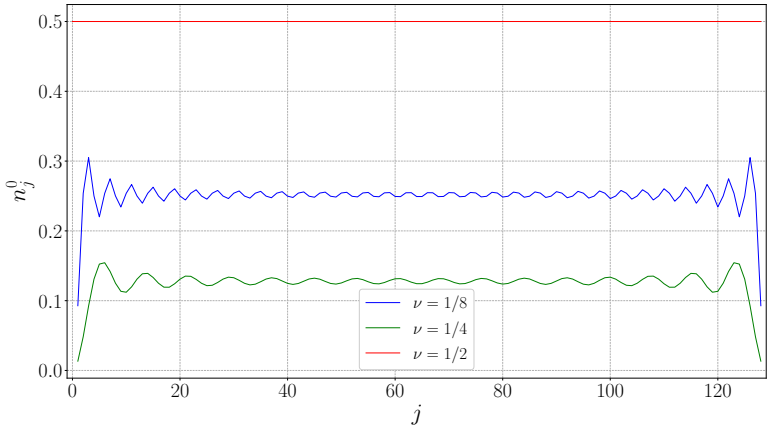

Figure 5.1: Non-interacting ground state density for different fillings. We set $L = 128$ and $t = 1$. Half-filling exhibits no oscillations. See text for details.

which reduces to the well known result in Eq. 2.22. In the TD limit, $L \to \infty$, the non-interacting density reduces to

$$n_j^0 = \nu - \frac{\sin\left(2k_{\mathrm{F}} j\right)}{2\pi j}. \tag{5.11}$$

Looking back at Eq. 5.8 we can alternatively identify the arctan with a Heaviside theta function $\theta(n)$ as

$$\begin{aligned} &- \sum_{n=1}^{L} \cos\left(2k_n j\right) \arctan\left(\frac{\omega}{\xi(k_n)}\right)\Bigg|_0^\infty \\ &= -\frac{\pi}{2} \sum_{n=1}^{L} \cos\left(2k_n j\right)\Big(\theta(n-N) - \theta(N-n)\Big). \end{aligned} \tag{5.12}$$

In this fashion, the density in the TD limit is straightforward to evaluate and without any reference to τ or the geometric series. In

particular, the second term yields

$$\begin{aligned}\lim_{L\to\infty} &-\frac{\pi}{2}\sum_{n=1}^{L}\cos\left(2k_n j\right)\Big(\theta(n-N)-\theta(N-n)\Big),\\ &=-\frac{\pi}{2}\frac{L+1}{\pi}\int_0^{\pi}\mathrm{d}k\cos\left(2kj\right)\Big(\theta(k-k_{\mathrm{F}})-\theta(k_{\mathrm{F}}-k)\Big),\\ &=\frac{L+1}{2}\frac{\sin\left(2k_{\mathrm{F}}j\right)}{j},\end{aligned} \tag{5.13}$$

and we obtain Eq. 5.11 again. It is interesting to note that at half-filling ($\nu = 1/2$) the density does not exhibit any oscillations which are characteristic of a finite system with boundaries. This can be attributed to the particle-hole symmetry of the spinless fermion Hamiltonian or, within the spin XXZ Heisenberg model representation, to the spin reversal symmetry; see Sect. 3.

We can also evaluate any single particle offdiagonal observable using the Matsubara formalism according to Eq. 2.20. In the non-interacting case this integral can be explicitly evaluated, and we obtain for $k > j$

$$\langle\hat{c}_j^{\dagger}\hat{c}_k\rangle_0 = \frac{\sin\left[\frac{\pi(k-j)}{L+1}(N+1/2)\right]}{2(L+1)\sin\left[\frac{\pi}{2(L+1)}\right]} - \frac{\sin\left[\frac{\pi(k+j)}{L+1}(N+1/2)\right]}{2(L+1)\sin\left[\frac{\pi}{2(L+1)}(k+j)\right]}. \tag{5.14}$$

5.1.2 Finite size DFT

In order to study the charge density oscillations of one-dimensional interacting fermions with OBC by means of DFT, we define the SF Kohn-Sham Hamiltonian as

$$H^{\mathrm{KS}} = -t\sum_{j=1}^{L-1}\left(c_{j+1}^{\dagger}c_j + c_j^{\dagger}c_{j+1}\right) + \sum_{j=1}^{L} v_j^{\mathrm{XC}} n_j + \sum_{j=1}^{L} v_j^{\mathrm{H}} n_j, \tag{5.15}$$

where, v_j^{XC} is the exchange-correlation potential which is a function(al) of the local densities as $v_j^{\mathrm{XC}} \equiv v_j^{\mathrm{XC}}[\{n_j\}]$, and $v_j^{\mathrm{H}} = U(n_{j+1} + n_{j-1})$ is the Hartree potential. The exchange-correlation

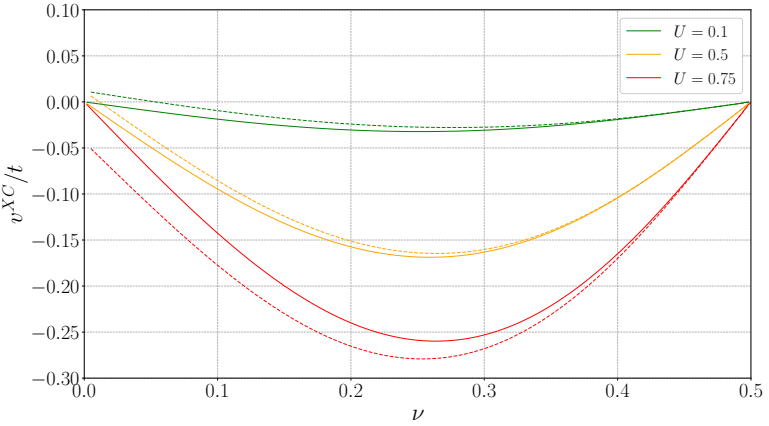

Figure 5.2: Exchange-correlation potential v^{XC} computed using Eq. 5.16 of the one-dimensional spinless fermion model for different interaction strengths U and average density (filling) ν. Solid lines are numerically obtained values from the BA equations. Dashed lines the parameterization proposed in Ref. [AC07]. We also use the fact that $v^{\mathrm{XC}}(1-\nu) = -v^{\mathrm{XC}}(\nu)$.

potential we use is built from the Bethe ansatz solution of the translationally invariant system with uniform density in the TD limit. In literature this is known as the local density approximation (LDA). This approximation implies that at each lattice site j the exchange-correlation potential is approximated by the potential obtained from a homogeneous electron liquid that has density n everywhere, in particular $v_j^{\mathrm{XC}}[\{n_j\}] \approx v^{\mathrm{XC,LDA}}[n]$.

The LDA exchange-correlation potential for this model, according to Ref. [SDSE08], is computed as

$$v_i^{\mathrm{XC,LDA}}(\nu, U) = \frac{\partial}{\partial \nu_i}\Big[e^{\mathrm{BA}}(\nu_i, U) - e^{\mathrm{H}}(\nu_i, U)\Big], \tag{5.16}$$

where $e^{\mathrm{BA}}(\nu_i)$ is the Bethe ansatz ground-state energy per site of the homogeneous system with the particular average density[7] ν and

[7] Note that the index i does not refer to the site index, but to the indexing

interaction strength U. This term is computed with Eq. 3.53. The remaining term is the Hartree energy which takes the following form $e^{\mathrm{H}}[\nu] = -\frac{2t}{\pi}\sin(k_{\mathrm{F}}) + U\nu^2$. We approximate the derivative with centered differences and additionally linearly interpolate to obtain a smooth LDA potential in regions where the BA equations become more challenging to solve (as $\nu \to 0$ and $\nu \to 1/2$). We already highlighted this particular issue in Sect. 3. In Fig. 5.2 we plot the LDA exchange-correlation potential obtained from the direct numerical evaluation of the BA equations. We compare the obtained potential with the parameterization proposed in Ref. [AC07]. This parameterization bypasses the intricate set of BA integral equations and is built by exploiting certain exact and closed form solutions of the BA equations at half-filling[8]. This parameterization therefore, as we can see from plot, gets more precise as we approach $\nu = 1/2$.

By construction, the LDA becomes exact in the homogeneous density limit. However, it turns out that LDA works quite well in some non-uniform situations; see Ref. [Ull12]. This is usually attributed to the error cancellation in the exchange-correlation energy from which the potential is derived. LDA exchange energies are usually overestimated while the correlation energies are underestimated, leading to an error compensation. We now explore how LDA performs for the Hamiltonian in Eq. 5.15.

In Fig. 5.3 we present the results of a DFT calculation, as introduced in Sect. 4, based on the LDA function(al) for a finite system of size $L = 128$ at quarter filling $\nu = 1/4$. To execute the calculation we used the efficient ODE DFT scheme detailed in Sect. 4.3. The criteria for convergence of the SCF cycle are taken as $\sum_j |n_j^{\mathrm{inp}} - n_j^{\mathrm{out}}| < \epsilon$. We set $\epsilon = 10^{-5}$, which is standard for most DFT calculations. The convergence is achieved in about ten SCF cycles, while performing the usual linear mixing of the density. The Friedel oscillation from the left boundary, as expected, interfere in the middle of the chain with the oscillations from the right boundary. In smaller systems the interference is more pronounced than in larger ones. Moreover, we compare the results for the density with the numerically exact amplitudes coming from DMRG.

of the average filling, i.e. different fillings.

[8] Equivalently, at zero magnetic field in the XXZ model; see Sect. 3 and Ref. [AC07] for details.

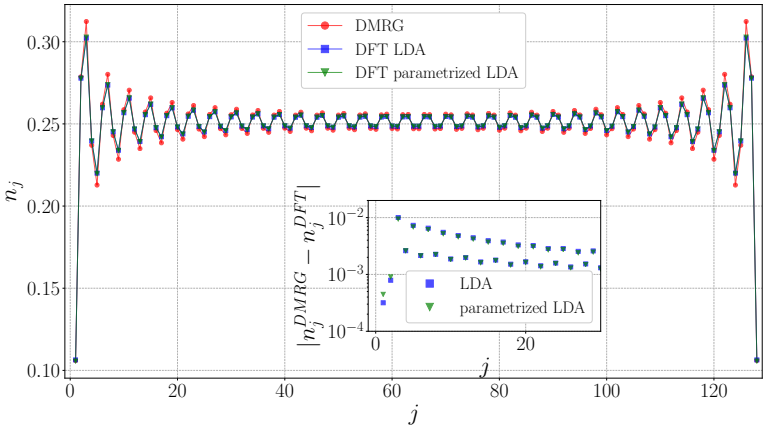

Figure 5.3: Density amplitude profile of a finite system of size $L = 128$ at quarter filling $\nu = 1/4$ for $U/t = 0.5$. Inset: difference between the numerical LDA and parameterized DFT and numerically exact DMRG for the same parameters.

The DFT densities exhibit the correct $2k_\mathrm{F}$ periodicity but the amplitudes are not correctly reproduced; see inset. The same trends in the density have been observed in Ref. [AC07] for the exchange-correlation functional(al) based on the parameterized LDA. Naively, one would expect that the exact numerical LDA performs better than the parameterization. However, the error that we make by using the parameterization[9] does not account for the wrong density amplitudes. The parameterization offers a less precise approximation of the true potential far away from half-filling and for stronger interactions[10]. Therefore, in all our further calculations we exclusively use the numerical LDA DFT approximation.

[9] For example at quarter filling.
[10] The first sites in the inset are a good example of this.

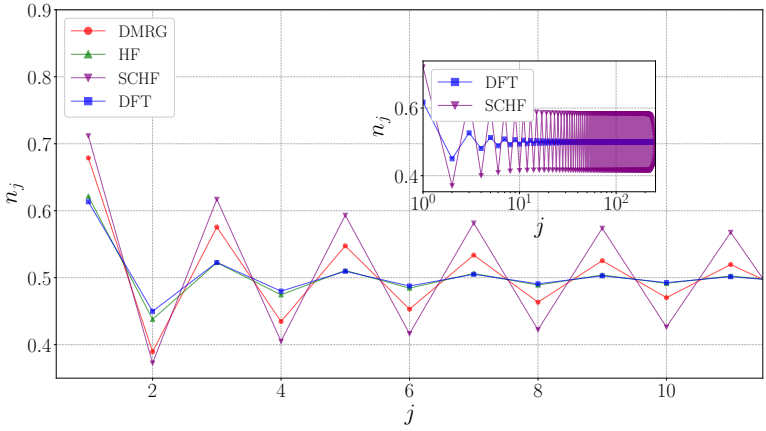

Figure 5.4: Density oscillation amplitudes for the first few sites away from the left boundary. We used $L = 64$ at half-filling $\nu = 1/2$ for $U/t = 1$. Inset: Same parameters but for a larger lattice of size $L = 512$. SCHF displays a non-decaying oscillation. A CDW is confirmed by observing that for ever increasing systems the oscillations maintain the non-decaying characteristic.

In Fig. 5.4 we compare the output of the LDA DFT calculation against other approximate methods such as Hartree-Fock (HF) and self-consistent Hartree-Fock (SCHF). Similarly to the HF approximation, DFT underestimates the amplitude of the oscillations. On the other hand, SCHF overestimates the amplitudes. In fact, the SCHF approximation exhibits a charge-density wave (CDW) modulation of the density (see inset), where at intermediate to long-distances away from the boundaries a non-decaying oscillation persist. A CDW is expected to appear in this system only for $U/t \geq 2$, and the SCHF predicts a CDW already at $U/t = 1$; see Ref. [Gia04]. However, LDA DFT shows no CDW instabilities during the self-consistency cycle which is an encouraging feature.

From bosonization and in the TD limit, as mentioned, we expect an algebraic power-law decay of the density oscillations. Obviously, the oscillations in the LDA calculations decay but the question remains if they decay according to the predictions. In addition, we

have to keep in mind that our data is for a system of finite size. In the literature different authors resort to simple fitting over a selected and finite dataset to show the underlying power-law; e.g. in Ref. [LSOC03]. However, it was decidedly shown in Ref. [CSN09] that conclusions from this kind of analysis are easily falsifiable. Therefore, in an effort to confirm or refute a potential power-law decay in the density data we compute the logarithmic derivative of the dominant density deviation envelope. The dominant envelope is the one with the largest amplitude, e.g. the densities at $j = 1, 3, 5, ...$ in Fig. 5.4 form this kind of envelope. Approximating the derivative with centered difference we define the logarithmic derivative as

$$\alpha_j = \frac{\ln\left(\tilde{n}_{j+\nu^{-1}}\right) - \ln\left(\tilde{n}_{j-\nu^{-1}}\right)}{\ln\left(j+\nu^{-1}\right) - \ln\left(j-\nu^{-1}\right)}, \tag{5.17}$$

with $\tilde{n}_j = n_j - \nu$ and where the mutual distance between local maxima in the density (dominant envelope) is ν^{-1}. We take as the criterion for a reliable detection of a power-law in the density data that the quantity defined in Eq. 5.17 has a constant value over several orders of magnitude in site index j. This derivative measure is extremely sensitive and any deviation from a power-law will be enhanced and apparent. The logarithmic derivative measure has been used before and for similar purpose in Ref. [MM16] and [AEM+04].

In Fig. 5.5 we show the logarithmic derivative of the dominant density envelopes for different numerical methods. The α_j is directly compared against the exact exponent of the asymptotic density decay for quarter filling computed via BA; see Eq. 3.42. We notice that as we move down the chain and away from the left boundary and into the bulk the influence of the right boundary prevents any consistent evaluation of the logarithmic derivative[11]. The α_j, for the HF and SCHF approximation, obviously differ. For the chosen parameter regime SCHF density decays as we move away from the boundary. However, this would no longer be the case if stronger interaction was considered due to the CDW instability. Nevertheless, the HF approximation always leads to a decaying density. At first glance,

[11] In particular, α_j deviates from a straight line that it is close to the left boundary.

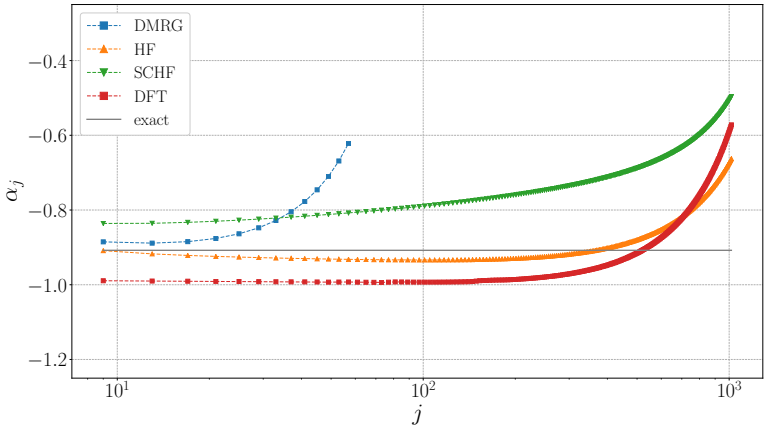

Figure 5.5: Logarithmic derivative of the dominant density envelope. We used $L = 2048$ at quarter filling $\nu = 1/4$ for $U/t = 0.5$. The DMRG logarithmic derivative profile has been obtained for $L = 128$ with the same parameters. For details see the main text.

one can argue that HF is characterized by an underlying power-law which does not fully develop due to the finite size effects. In Chap. 6 and 7 we perform an extensive analysis to determine if this is indeed the case. In principle, LDA DFT should provide an improvement to the HF approximation. However, is this really the case we answer in the last chapter. This is because, it is true even for the DMRG (which is considered numerically exact) that reliable measurement of a power-law in the density decay is practically impossible due to finiteness of the system. Therefore, in Sect. 7 we discuss how to minimize the effects of backscattering in finite systems by coupling them to an infinite non-interacting environment, and enable the evaluation of the potential power law decay in the density according to the criterion advocated here; see Sect. 2.5.

5.2 Long-range interaction in real-space

We consider a one-dimensional Hamiltonian in first quantized form of N particles moving in a box. The Hamiltonian is defined as

$$H = -\frac{1}{2}\sum_{j=1}^{N}\frac{d^2}{dx_j^2} + \frac{1}{2}\sum_{\substack{j\neq k\\ j,k=1}} v^{\text{int}}(x_j, x_k), \tag{5.18}$$

where v^{int} defines the two-particle interaction, which we consider to be a regularized Coulomb interaction. The regularization parameter is usually associated with an effective transverse dimension d and is frequently encountered in the literature; see e.g. Ref. [HFC+11] and [EG96]. The effective or 'soft' Coulomb potential is of the form

$$v^{\text{soft-C}}(x_j, x_k) = \frac{e^2}{\sqrt{d^2 + (x_j - x_k)^2}}, \tag{5.19}$$

and its Fourier transform reads as

$$V(q) = 2e^2 K_0(qd), \tag{5.20}$$

where K_0 is the modified Bessel function of the second type of order zero. It diverges logarithmically as the argument is sent to zero.

In finite systems with N non-interacting electrons in a box $x \in [-L, L]$[12] the density reads

$$\begin{aligned} n(x, L, N) &= \frac{2}{L}\sum_{n=1}^{N}\sin^2\left[\frac{n\pi}{2L}(x+L)\right] \\ &= \frac{N}{L} - \frac{1}{L}\frac{\cos\left[\frac{\pi}{2L}(x+L)(N+1)\right]\sin\left[\frac{\pi}{2L}(x+L)\right]}{\sin\left[\frac{\pi}{2L}(x+L)\right]}. \end{aligned} \tag{5.21}$$

The expression for density in the second line of Eq. 5.21 follows directly from the sum over the states in the first line by use of the

[12] We choose to position the box in accordance to the how the grid is defined in the *Octopus* environment; see Sect. 5.2.1.

geometric series. In the thermodynamic limit where $L \to \infty$ and ratio N/L is kept constant the density decays as x^{-1}.

From bosonization in Refs. [Sch93] and [Kle] it is expected that in case of spinless fermions and long-range interactions the Friedel oscillations decay asymptotically as

$$\delta n(x) \sim \cos(2k_{\mathrm{F}}x) \exp\Big[- C(\ln x)^{\frac{1}{2}} - D(\ln x)^{-\frac{1}{2}} + \mathcal{O}\Big((\ln x)^{-\frac{3}{2}}\Big)\Big], \tag{5.22}$$

where C and D are interaction dependent constants. This is in stark contrast to the power-law decay for vanishing and short-range interactions in Eq. 5.21 and 5.2, respectively. In fact, the decay is slower than any power law which is a direct consequence of the logarithmic divergence of the Fourier transform as $q \to 0$. This kind of slow asymptotic decay presents a computational challenge even within the field theory approach; see Ref. [Kle] for details. With this in mind we expect the finite size data from microscopic models to reach the asymptotic regime for extremely large system sizes.

Furthermore, the Wigner component of $4k_{\mathrm{F}}$ periodicity, contrary to the short-range interaction again, is expected to be present in the density decay for long-range interactions according to the bosonization treatment in Ref. [Sch93].

5.2.1 Finite size DFT

In Fig. 5.6 we present the results of an LDA DFT calculation performed for the Hamiltonian in Eq. 5.18. The LDA potential we use for one-dimensional real-space is presented in Ref. [HFC+11]. The exchange-correlation potential is built from the numerically exact GS energy of the 1D homogeneous electron gas. The exchange energy e^{X} is analytically known while the correlation energy is computed using the Monte Carlo techniques described in Ref. [CSS06]. This approximation is part of the *libxc* package and was shown to be of the same quality (in respect to the phenomena it is able to capture) as its counterpart in 3D with common Coulomb interaction; see see Ref. [MOB12] and [HFC+11].

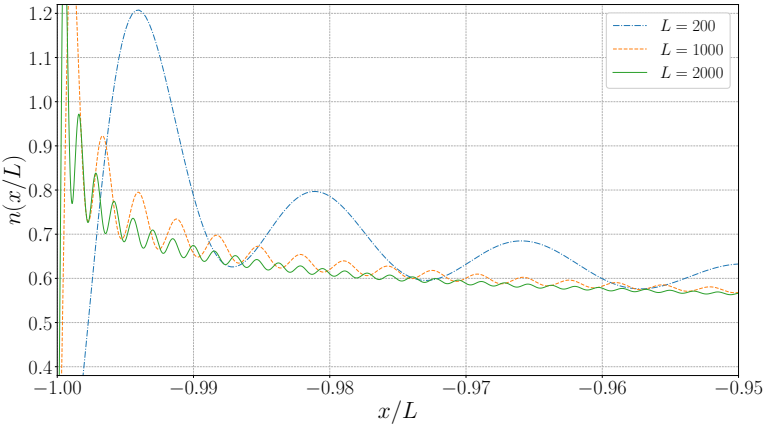

Figure 5.6: Friedel oscillations of the density for soft-Coulomb interaction performed with LDA DFT. Different system sizes at half-filling are considered. Calculation are performed in Hartree (Ha) atomic units as is common within the *Octopus* environment. Further details are given in the text.

To perform the DFT calculation we used the real-space implementation *Octopus* detailed in Ref. [ASG+15]. Given that we take the system to be half-filled ($N = L/2$) the diagonalization is a costly procedure despite treating an effectively non-interacting KS Hamiltonian. Treating N electrons implies keeping and working with at least N orbitals defined on extremely large grids, and computational resources quickly get expended. Therefore, we employed a parallelized version of the code to compute the density and to relieve the computational load. We set the spacing to be $\Delta x = 0.05$, and convergence was achieved in less then 50 SCF steps with the usual $\epsilon < 10^{-5}$ criterion.

To measure the density decay we first isolate the dominant envelope of the density, i.e. local maxima at $2k_{\mathrm{F}}$ periodicity. These data points, however, exhibit a decay that can not be reliably attributed with a naive fitting procedure to the expected exponential decay coming from bosonization in Eq. 5.22 or any power-law. Moreover, the density coming from LDA DFT calculations does not exhibit

the $4k_\mathrm{F}$ Wigner component predicted in Ref. [Sch93]. This is made obvious by taking the Fourier transform of the density as was done in Fig. 5.7.

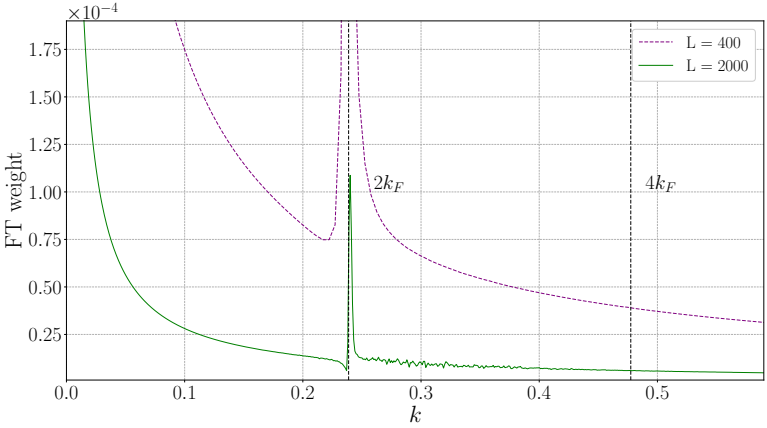

Figure 5.7: Fourier transform of the density for soft-Coulomb interaction performed with LDA DFT. Different system sizes at half-filling are considered. The $4k_\mathrm{F}$ component is not present in the density data. Calculation are performed in Hartree (Ha) atomic units.

5.3 Hubbard model

A prototypical model for electrons with local interactions is the Hubbard model (HM). In second quantization with OBC it reads

$$H = -t \sum_{\substack{j=1 \\ \sigma=\uparrow,\downarrow}}^{L-1} (c^\dagger_{\sigma,j} c_{\sigma,j+1} + c^\dagger_{\sigma,j+1} c_{\sigma,j}) + U \sum_{j=1}^{L} n_{\uparrow,j} n_{\downarrow,j}, \qquad (5.23)$$

where the lattice has L sites. $c^\dagger_{\sigma,j}$ ($c_{\sigma,j}$) creates (destroys) an electron of spin species σ at site j, $n_{\sigma,j} = c^\dagger_{\sigma,j} c_{\sigma,j}$ is the occupation operator at site j of the particular spin and U is the on-site Coulomb repulsion.

The second term of the Hamiltonian in Eq. 5.23 adds an energy cost to sites that are occupied by electrons of both up and down spin, while the first term describes free electrons. This simple model exhibits rich physics because of the competition of the interaction and kinetic term which is able to capture the metal-insulator phase transitions.

The HM is integrable as shown in Ref. [LW68]. Furthermore, it displays Luttinger liquid features away from half-filling for repulsive interactions. However, at half-filling a Mott insulator gap develops; see Ref. [Gia04]. Boundaries and impurities in the metallic phase of the HM generate Friedel oscillations (FO) as in the SFM; see Sect. 5.1. From bosonization it is known that the FO in the HM decay asymptotically as $(K_\sigma + K_\rho)/2$ away from the boundaries and for weak impurities as $1 - K_\sigma - K_\rho$ at intermediate distances. K_σ and K_ρ are exponents of the spin and the charge channel, respectively, and they can be computed exactly using the BA; see Ref. [Sch90].

It is important to note that the HM in Eq. 5.23 has a more involved low-energy asymptotics than the SFM in Eq. 5.1. A qualitatively correct description of the particularity of the HM with OBC at low energies is captured already by the Hartree-Fock approximation; see Ref. [SMM+00]. The local density of states (LDOS) $D_j(\omega)$ computed using perturbation theory[13] to first order in the interaction and close to the boundary reads

$$D_j(\omega) = D_j^0\left(1 + \frac{\tilde{V}(0) - 2\tilde{V}(2k_\mathrm{F})}{2\pi v_\mathrm{F}} \ln\left|\omega/\epsilon_\mathrm{F}\right| + \mathcal{O}(\tilde{V}^2)\right), \quad (5.24)$$

where $D_j^0(\omega)$ is the non-interacting LDOS, v_F is the Fermi velocity, ϵ_F the Fermi energy and $\tilde{V}$ is the Fourier transform of the real space interaction. Due to the local interaction in the HM the prefactor to the logarithmic term reduces to $\tilde{V}(0) - 2\tilde{V}(2k_\mathrm{F}) = -U$ and is negative for repulsive interactions ($U > 0$). This implies an *enhancement*[14] in $D_j(\omega)$ as $\omega \to 0$. The LDOS, however, undergoes a crossover when the first order correction term is of order one,

[13] We apply a similar type of analysis to the density in Sect. 6 but for the SFM.

[14] Bosonization, on the other hand, predicts a power-law *suppression* of the LDOS; see Eq. 5.26

making the second order correction terms relevant. In particular, from Eq. 5.24 it follows that the crossover (to a regime where the LDOS is suppressed) happens for

$$\omega_c = \epsilon_{\mathrm{F}} \exp\left(\frac{2\pi v_{\mathrm{F}}}{\tilde{V}(0) - 2\tilde{V}(2k_{\mathrm{F}})}\right), \tag{5.25}$$

which corresponds to a system size $L_c = \pi v_{\mathrm{F}}/\omega_c$. From Eq. 5.25 we observe that for weak interactions ($U \ll 2\pi k_{\mathrm{F}}$) the length scale at which the crossover happens is extremely large, implying we need extremely high energy resolution data to investigate the Luttinger liquid fixed point physics. However, the stronger the interaction, the smaller the crossover scale L_c becomes; see e.g. Fig. 5 and 6 in Ref. [AEM+06]. The existence of the crossover behavior and the phenomena of an enhanced LDOS is supported by the 'full inversion'[15] Hartree-Fock studies, DMRG and fRG studies; see Refs. [SMM+00, MMS+00].

The enhancement of the LDOS occurs due to the backward scattering process which is present in HM. In the g-ology language[16] the low-energy interaction processes are classified into:

- g_1 - backward scattering (fermions change from being left- to right-moving and vice versa which corresponds to $2k_{\mathrm{F}}$ scattering)
- g_2 - forward scattering (couples fermions from one side of the Fermi surface to the fermions on the other side)
- g_3 - Umklapp scattering (irrelevant away from half-filling)
- g_4 - forward scattering (couples fermions on the same side of the Fermi surface)

For the HM g_1 processes of electrons with opposite spin are distinguishable from g_2 processes. This is not the case in the absence of the spin degree of freedom as for example in the SFM in Sect. 5.1. The influence of the backscattering becomes obvious if the boundary

[15] When all orders in Eq. 5.24 are considered.
[16] See Refs. [Sól79, Gia04] for an extensive introduction.

exponent α_B is examined. α_B is the power law exponent of the local spectral function[17] which scales as

$$\rho_j(\omega) \sim |\omega|^{\alpha_B} \quad \text{as} \quad \omega \to 0, \tag{5.26}$$

where

$$\alpha_B = \frac{1}{2K_\rho} + \frac{1}{2K_\sigma} - 1. \tag{5.27}$$

The renormalization group flow[18] analysis showed that $K_\sigma = 1$ is approached only logarithmically from above because of the slow logarithmic decrease of the g_1 coupling[19]; see Fig. 4 in Ref. [AEM+06]. From Eq. 5.27 this implies that the asymptotic α_B is reached logarithmically slow from below, which is consistent with the perturbative LDOS results in Eq. 5.24. Furthermore, given that the decay of the FO is parameterized by the Luttinger parameter, one can expect that the same mechanism is active in the density and the low energy asymptotics is realized only at very long distances.

Irrespective of the low energy particularities, the decay of FO in the HM has been studied by means of LDA DFT in Ref. [CLSO03] and [LSOC03]. The authors assumed the existence of a pure power-law behavior in the density and performed a fit to obtain the decay exponent. In the case of repulsive interactions they obtained values for the exponents smaller than -1. This can be taken as an indication that their assumptions of a pure underlying power-law behavior is incorrect. Furthermore, given the system sizes considered in Ref. [LSOC03] the data must be influenced by finite size effects. This is made obvious by the numerically exact DMRG density data and its logarithmic derivative plot in Fig. 5.5 for the case of SFM. If we trivially averaged the exponent over the sites j for a lattice system of this small size[20] in Fig. 5.5 we would obtain an exponent dominated by finite size effects. On the other hand, by simply

[17] Defined using the Green's function as $\rho_j(\omega) = -\mathrm{Im}G_{j,j}(\omega + i0^+)/\pi$, and is equivalent to the LDOS in Eq. 5.24 up to the level spacing; see Ref. [SMM+00]. If Eq. 5.26 is expanded, logarithmic terms as the ones in Eq. 5.24 are present.

[18] Correct up to second order in the interaction.

[19] Where $K_\sigma = 1$ for spin-rotation invariant systems.

[20] $L = 128$ is comparable to the system sizes considered in Ref. [CLSO03].

fitting the data to a power law also introduces uncontrolled errors by selecting over which range the fit is performed on top of the data being contaminated by finite size effects.

The backscattering g_1 can be tuned to zero if the HM is extended. In particular, if the Hamiltonian in Eq. 5.23 is supplemented with an extra interaction term between nearest-neighbor sites of the form

$$H^{\text{extended}} = H + U' \sum_{j=1}^{L-1} n_j n_{j+1}. \tag{5.28}$$

Then for this model there exists a particular choice of U'/U, such that the backscattering is completely gone, and the prefactor to the logarithmic term in Eq. 5.24 is positive for repulsive interactions. The extended HM in Eq. 5.28 is, however, not integrable and its low energy physics is similar to the SFM; see Ref. [AEM+06].

6 Friedel oscillations from perturbation theory

This Chapter is dedicated to the analytical perturbation theory results on the spinless fermion model with nearest-neighbor interactions and OBC. We employ the Matsubara Green's function formalism from Chap. 2 and find that, away from half-filling, the first order perturbation theory for the density is consistent with the field theory prediction to the leading order in the interaction. In particular, we identify the divergent logarithmic correction in the site index with a prefactor that is linear in U; see Sect. 6.1. This result is however surprising, given that in systems with PBC the divergent terms appear only at the second order in the interaction; see Ref. [Sól79]. At half-filling we show that the perturbation theory exhibits non-generic features, i.e. is inconsistent with field theory predictions. Therefore, in Sect. 6.2 we change the basis in which we perform the perturbative treatment resulting in a consistent Hartree-Fock approach.

6.1 Interacting ground state density away from half-filling

In the presence of interactions, the Matsubara Green's function becomes more difficult to compute due to the non-trivial structure of the self-energy

$$G_{n,n'}(i\omega) = \frac{1}{\Big[i\omega - \xi(k_n)\Big]\delta_{n,n'} - \Sigma_{n,n'}(i\omega)}, \tag{6.1}$$

where the self-energy $\Sigma(i\omega)$ encodes the effect of the interaction; see Sect. 2. In Sect. 6.1.1 we derive the frequency independent self-energy to first order in the interaction (Hartree-Fock) for SFM defined in Eq. 5.1.

6.1.1 Perturbation theory for the self-energy

The starting point is the two-particle interaction term of the SFM with OBC, which reads

$$\hat{V} = U \sum_{j=1}^{L-1} \hat{c}_j^\dagger \hat{c}_j \hat{c}_{j+1}^\dagger \hat{c}_{j+1}. \tag{6.2}$$

The two-particle interaction term in Eq. 6.2 can be written in terms of the creation and annihilation operators $\hat{a}_n^\dagger$, $\hat{a}_n$ of the eigenstates φ_n. In particular,

$$\hat{c}_j^\dagger = \sum_{n=1}^{\infty} \varphi_n(j) \hat{a}_n^\dagger. \tag{6.3}$$

In this basis the interaction term reads

$$\hat{V} = \sum_{n,m,n',m'} v_{n,m;n',m'} \hat{a}_n^\dagger \hat{a}_{n'} \hat{a}_m^\dagger \hat{a}_{m'}, \tag{6.4}$$

$$\tag{6.5}$$

where

$$\frac{v_{n,m;n',m'}}{4U} = \sum_{j=1}^{L-1} \frac{\sin(k_n j)\sin(k_{n'} j)\sin\big[k_m(j+1)\big]\sin\big[k_{m'}(j+1)\big]}{(L+1)^2}. \tag{6.6}$$

Using basic trigonometric identities we can rewrite the matrix elements as

$$v_{n,m;n',m'} = \frac{1}{L+1}\Big[F(k_n - k_{n'}, k_m - k_{m'}) - F(k_n - k_{n'}, k_m + k_{m'}) \\ - F(k_n + k_{n'}, k_m - k_{m'}) + F(k_n + k_{n'}, k_m + k_{m'})\Big], \tag{6.7}$$

where we defined F as

$$F(q,q') = \frac{U}{(L+1)}\sum_{j=1}^{L}\cos(qj)\cos(q'(j+1)) \\ - \frac{U}{L+1}\cos(qL)\cos(q'(L+1)). \tag{6.8}$$

Here, the second term is a boundary term that emerges due to the sum going from 1 to L. Going further we denote it by B and proceed to write

$$F(q,q') = \frac{U}{4(L+1)}\sum_{j=1}^{L}\Big[e^{i(q+q')j+iq'} + e^{i(q-q')j-iq'} \\ + e^{-i(q-q')j+iq'} + e^{-i(q+q')j-iq'}\Big] - B. \tag{6.9}$$

Using $\sum_{j=1}^{L} e^{i(q-q')j+iq} = e^{iq}\sum_{j=1}^{L} e^{i(q-q')j} = e^{iq}\delta^{(2\pi)}_{q,q'}L$, where $\delta^{(2\pi)}$ is the 2π-periodic delta function, we obtain

$$F(q,q') = \frac{U}{2}\left(1 - \frac{1}{L+1}\right)\cos(q)\left[\delta^{(2\pi)}_{q,q'} + \delta^{(2\pi)}_{q,-q'}\right] - B. \tag{6.10}$$

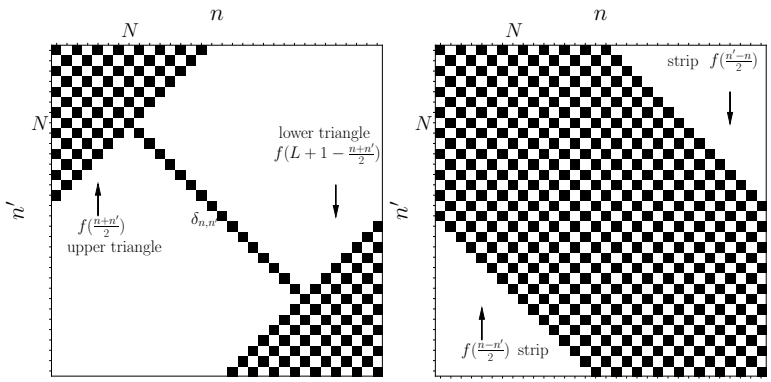

Figure 6.1: Graphical representation of the self-energy matrix structure $\frac{(L+1)}{U}\Sigma_{n,n'}$ in Eq. 6.12. The non-vanishing contributions are given in black with the left plot representing the last two lines of Eq. 6.12 and the right plot giving the second line. Parameters used to generate the plot: $L = 32$ and $N = 8$ (quarter filling). The lower triangle term is also known as the Umklapp term in the literature.

The matrix elements now read

$$\begin{aligned} v_{n,m;n',m'} = & \frac{U}{2(L+1)}\left(1-\frac{1}{L+1}\right) \\ & \times \Bigg\{ \cos\left(k_n - k_{n'}\right)\left[\delta^{(2\pi)}_{k_n-k_{n'},k_m-k_{m'}} + \delta^{(2\pi)}_{k_n-k_{n'},-(k_m-k_{m'})}\right] \\ & - \cos\left(k_n - k_{n'}\right)\left[\delta^{(2\pi)}_{k_n-k_{n'},k_m+k_{m'}} + \delta^{(2\pi)}_{k_n-k_{n'},-(k_m+k_{m'})}\right] \\ & - \cos\left(k_n + k_{n'}\right)\left[\delta^{(2\pi)}_{k_n+k_{n'},k_m-k_{m'}} + \delta^{(2\pi)}_{k_n+k_{n'},-(k_m-k_{m'})}\right] \\ & + \cos\left(k_n + k_{n'}\right)\left[\delta^{(2\pi)}_{k_n+k_{n'},k_m+k_{m'}} + \delta^{(2\pi)}_{k_n+k_{n'},-(k_m+k_{m'})}\right] \Bigg\} \\ & - \frac{B}{L+1}. \end{aligned} \tag{6.11}$$

We note that the boundary term does not contribute in the TD

limit due to the additional factor of $1/L$. This term only becomes relevant in fairly small systems.

We further decompose the four fermion operators in Eq. 6.4 as $\hat{a}_n^\dagger \hat{a}_{n'} \hat{a}_m^\dagger \hat{a}_{m'} \approx 2\hat{a}_n^\dagger \hat{a}_{n'} \langle \hat{a}_m^\dagger \hat{a}_{m'} \rangle - 2\hat{a}_n^\dagger \hat{a}_{m'} \langle \hat{a}_m^\dagger \hat{a}_{n'} \rangle$. These two constitute the direct Hartree and Fock exchange terms of the self-energy. Performing the operator algebra and satisfying different momentum conservation conditions we identify the self-energy at Hartree-Fock level as

$$\begin{aligned}\frac{(L+1)\Sigma^{\mathrm{HF}}_{n,n'}}{U} &= \left\{ 2N - \sum_{m=1}^{N} \Big[\cos(k_n - k_m) + \cos(k_n + k_m) \Big] \right\} \delta_{n,n'} \\ &- \left\{ \cos(k_n - k_{n'}) - \cos\left(\frac{k_n + k_{n'}}{2} \right) \right\} f\left(\frac{|n - n'|}{2} \right) \\ &+ \left\{ \cos(k_n + k_{n'}) - \cos\left(\frac{k_n - k_{n'}}{2} \right) \right\} f\left(\frac{n + n'}{2} \right) \\ &+ \left\{ \cos(k_n + k_{n'}) + \cos\left(\frac{k_n - k_{n'}}{2} \right) \right\} f\left(L + 1 - \frac{n + n'}{2} \right),\end{aligned} \tag{6.12}$$

where we have used the following notation

$$f\left(\frac{n - n'}{2} \right) = \theta\left(k_{\mathrm{F}} - k_{\frac{n-n'}{2}} \right) \tag{6.13}$$

$$f(m) = \begin{cases} 1, & \text{if} \quad m \leq N \quad \wedge \quad m \in \mathbb{N}, \\ 0, & \text{otherwise.} \end{cases} \tag{6.14}$$

The self-energy contains both diagonal and offdiagonal terms and when the matrix elements indices are such that $n + n'$ is even we have a non-vanishing contribution. The graphical representation of the matrix structure is given in Fig. 6.1. We assign different names (*lower*,*upper* and *strip*) to each of the terms for later use. Each term has a Hartree and a Fock part, corresponding to the first and second term in each line of Eq. 6.12, respectively. We focus now on the

diagonal elements and derive, using the geometric series,

$$\begin{aligned}\Sigma^{\mathrm{HF}}_{n,n} &= \frac{U}{L+1}\left\{2N - 2\cos(k_n)\sum_{m=1}^{N}\cos\left(k_m\right)\right\} \\ &= \frac{U}{(L+1)}\left\{2N - \cos(k_n)\left(\frac{\sin\left[\frac{\pi}{2(L+1)}(2N+1)\right]}{\sin\left[\frac{\pi}{2(L+1)}\right]} - 1\right)\right\}.\end{aligned} \tag{6.15}$$

Then, in the TD limit ($L \to \infty$) the diagonal part of the self-energy reads

$$\Sigma^{\mathrm{HF}}_{n,n} = 2U\nu - \frac{2U}{\pi}\sin\left(\pi\nu\right)\cos\left(k_n\right). \tag{6.16}$$

In the Green's function we separate the diagonal and off-diagonal self-energy[1] contributions as

$$G^{\mathrm{HF}}_{n,n'}(i\omega) = \frac{1}{\Big[i\omega - \xi(k_n)\Big]\delta_{n,n'} - \Sigma^{\mathrm{HF}}_{n,n'}\delta_{n,n'} - \tilde{\Sigma}^{\mathrm{HF}}_{n,n'}}. \tag{6.17}$$

In Eq. 6.16 the first term is a shift of the chemical potential and the second term renormalizes the hopping. Therefore, the renormalized dispersion at Hartree-Fock level reads

$$\begin{aligned}\bar{\xi}(k_n) &= -2\bar{t}\cos\left(k_n\right) - \bar{\mu}, \\ \bar{t} &= t + \frac{U}{\pi}\sin\left(\pi\nu\right), \\ \bar{\mu} &= \mu - 2U\nu.\end{aligned} \tag{6.18}$$

In terms of the renormalized quantities, the Green's function, Eq. 6.17, reads

$$G^{\mathrm{HF}}_{n,n'}(i\omega) = \frac{1}{\Big[i\omega - \bar{\xi}(k_n)\Big]\delta_{n,n'} - \tilde{\Sigma}^{\mathrm{HF}}_{n,n'}}. \tag{6.19}$$

In comparison, in case of PBC the self-energy is diagonal in the momentum representation, and the renormalization of t and μ is the same as for OBC which we consider here.

[1] We denote with $\bar{\Sigma}$ the offdiagonal self-energy contributions.

The off-diagonal (non-local) structure of the self-energy, encoded in Eq. 6.12, makes taking the inverse to obtain the Green's function difficult. Therefore, going further we expand for the Green's function matrix to circumvent the inversion; see Sect. 6.1.2.

6.1.2 Perturbation theory for the Green's function

Ignoring the indices and frequency dependence for a moment we rewrite the previous Dyson equation as

$$G^{\mathrm{HF}}(i\omega) = \underbrace{\frac{1}{[i\omega - \bar{\xi}(k)]I}}_{=D} \cdot \frac{1}{I - \tilde{\Sigma}^{\mathrm{HF}} \cdot \dfrac{1}{[i\omega - \bar{\xi}(k)]I}}, \tag{6.20}$$

where I denotes the identity matrix operator. We expand the second factor in a geometric series[2]

$$G^{\mathrm{HF}} = D(I + \tilde{\Sigma}^{\mathrm{HF}} D + \tilde{\Sigma}^{\mathrm{HF}} D \tilde{\Sigma}^{\mathrm{HF}} D + \ldots). \tag{6.21}$$

We further focus on the leading correction term $D\tilde{\Sigma}^{\mathrm{HF}} D$. Reintroducing all the k-space indices yields

$$\left[D\tilde{\Sigma}^{\mathrm{HF}} D\right]_{n,n'} = \sum_{m=1}^{\infty} \sum_{m'=1}^{\infty} D_{n,m} \tilde{\Sigma}^{\mathrm{HF}}_{m,m'} D_{m',n'} = D_{n,n} \tilde{\Sigma}^{\mathrm{HF}}_{n,n'} D_{n',n'}. \tag{6.22}$$

[2]The diagonal elements dominant over the offdiagonal ones making the geometric series expansion consistent.

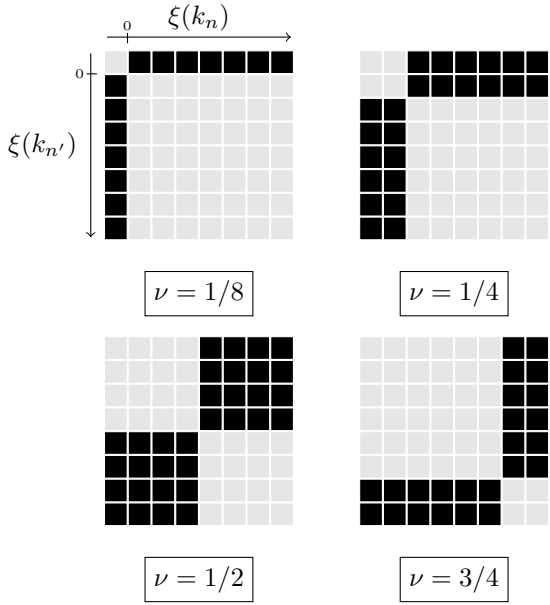

Figure 6.2: Contributing parts of $k_n, k_{n'}$-space for different filling. Black color: non-vanishing contribution. Grey color: no contribution. System size $L = 8$ taken for this sketch.

The simplification of indices is due to the diagonal structure of D. Using the expansion in Eq. 6.21 we avoid taking the inverse of the self-energy matrix in order to calculate the Green's function. Therefore, we are able to compute the density at equilibrium and zero temperature according to Eq. 2.14 and Eq. 6.21 as

$$n_j^{\mathrm{HF}} = \frac{1}{2\pi} \int_{-\infty}^{\infty} \mathrm{d}\omega e^{i\omega\eta} G_{j,j}^{\mathrm{HF}}(i\omega) = n_j^0 + n_j^{1\mathrm{PT}} + \cdots , \tag{6.23}$$

where a non-vanishing self-energy produces a correction to the density due to the interaction. In Sect. 5.1, for example, we computed the explicit inverse of the Hamiltonian matrix and obtained the complete Green's function and the series in Eq. 6.23. This 'full inversion' procedure is numerical and does not provide any analytic

insight into the behavior of the density. However, n_j^{1PT} is simple enough to enable such an analysis. In particular, it follows that

$$n_j^{\mathrm{1PT}} = \frac{1}{\pi(L+1)} \underbrace{\int_{-\infty}^{\infty} \mathrm{d}\omega e^{i\omega\eta} \sum_{n,n'=1} \frac{\sin(k_n j)\sin(k_{n'} j)}{[i\omega - \bar{\xi}(k_n)][i\omega - \bar{\xi}(k_{n'})]} \tilde{\Sigma}^{\mathrm{HF}}_{n,n'}}_{=T} \tag{6.24}$$

The convergence factor η is, at this stage, not necessary because the integrand asymptotically decays as $1/\omega^2$; see the discussion in Sect. 2.3. We perform the same steps as in the non-interacting case and interchange the sum and the integral[3] to obtain

$$T = \sum_{n,n'=1} \tilde{\Sigma}^{\mathrm{HF}}_{n,n'} \sin(k_n j)\sin(k_{n'} j) \int_{-\infty}^{\infty} \mathrm{d}\omega \frac{1}{[i\omega - \bar{\xi}(k_n)][i\omega - \bar{\xi}(k_{n'})]}. \tag{6.25}$$

We evaluate the integral by contour integration. We are free to close the contour in either the upper or the lower half-plane, which leads to

$$T = 2\pi \sum_{n,n'=1} \frac{\tilde{\Sigma}^{\mathrm{HF}}_{n,n'} \sin(k_n j)\sin(k_{n'} j)}{\bar{\xi}(k_n) - \bar{\xi}(k_{n'})} \Big\{ \Theta\big[-\bar{\xi}(k_n)\big]\Theta\big[\bar{\xi}(k_{n'})\big] - \Theta\big[-\bar{\xi}(k_{n'})\big]\Theta\big[\bar{\xi}(k_n)\big] \Big\}. \tag{6.26}$$

In Fig. 6.2 we explore different fillings and visualize the non-vanishing parts of the $k_n, k_{n'}$-space that are a direct consequence of the step functions. The sums run exclusively over the black colored parts of the matrix. We further denote $\tilde{\sigma}^{\mathrm{HF}}_{n,n'} = (L+1)\tilde{\Sigma}^{\mathrm{HF}}_{n,n'}$ and write down the final expression for the density[4] as

$$n_j^{\mathrm{1PT}} = \frac{2U}{\bar{t}(L+1)^2} \sum_{n'=N+1}^{L} \sum_{n=1}^{N-1} \frac{\sin\left(\frac{n\pi}{L+1} j\right)\sin\left(\frac{n'\pi}{L+1} j\right)}{\cos\left(\frac{n'\pi}{L+1}\right) - \cos\left(\frac{n\pi}{L+1}\right)} \tilde{\sigma}^{\mathrm{HF}}_{n,n'}, \tag{6.27}$$

[3] As was done in Sect. 5.1.1.

[4] Due to the symmetry of the matrix elements under the exchange of indices $n \to n'$ the two terms in Eq. 6.26 are equivalent.

with

$$\begin{aligned}\tilde{\sigma}^{\mathrm{HF}}_{n,n'} = &-\left\{\cos\left(k_n - k_{n'}\right) - \cos\left(\frac{k_n + k_{n'}}{2}\right)\right\} f\left(\frac{n' - n}{2}\right) \\ &+\left\{\cos\left(k_n + k_{n'}\right) - \cos\left(\frac{k_n - k_{n'}}{2}\right)\right\} f\left(\frac{n + n'}{2}\right) \\ &+\left\{\cos\left(k_n + k_{n'}\right) + \cos\left(\frac{k_n - k_{n'}}{2}\right)\right\} f\left(L + 1 - \frac{n + n'}{2}\right).\end{aligned} \tag{6.28}$$

The density to first order in Eq. 6.27 can be readily evaluated for finite systems. Moreover, one can perform the asymptotic analysis of this expression in the TD limit; see Sect. 6.1.3.

6.1.3 The TD limit

Taking the TD limit ($L \to \infty$) turns the sums in Eq. 6.27 into integrals. In particular,

$$\sum_{n'=N+1}^{L} \sum_{n=1}^{N-1} \to \frac{(L+1)^2}{2\pi^2} \int_0^{k_{\mathrm{F}}} \int_{k_{\mathrm{F}}}^{\pi} \mathrm{d}k \mathrm{d}k'. \tag{6.29}$$

It is important to note that the factor $1/2$ accounts for the fact that the density of points in the continuum is half of what it should be because in the discrete case we considered only even elements. Consequently, in the TD limit we have

$$n_j^{\mathrm{1PT}} = \frac{U}{t\pi^2} \int_0^{k_{\mathrm{F}}} \int_{k_{\mathrm{F}}}^{\pi} \frac{\sin\left(kj\right)\sin\left(k'j\right)}{\cos\left(k'\right) - \cos\left(k\right)} \sigma^{\mathrm{HF}}_{k,k'} \mathrm{d}k' \mathrm{d}k, \tag{6.30}$$

and

$$\begin{aligned}\sigma^{\mathrm{HF}}_{k,k'} = &-\left\{\cos(k-k') - \cos\left(\frac{k+k'}{2}\right)\right\}\theta\left(k_{\mathrm{F}} - \frac{k-k'}{2}\right)\\ &+\left\{\cos(k+k') - \cos\left(\frac{k-k'}{2}\right)\right\}\theta\left(k_{\mathrm{F}} - \frac{k+k'}{2}\right)\\ &+\left\{\cos(k+k') + \cos\left(\frac{k-k'}{2}\right)\right\}\theta\left(\pi - \frac{k+k'}{2}\right). \quad (6.31)\end{aligned}$$

Interestingly, due to the denominator which is intrinsic to the leading order correction and not because of the self-energy, the integrand in Eq. 6.30 appears to be singular at $k = k' = k_{\mathrm{F}}$. However, this does not imply that the integrals themselves are ill-defined and without a finite value. In particular, for choices of j's, e.g. at quarter filling ($\nu = 1/4$) and at sites[5] $j = 4, 8, 12, \ldots$ n_j^{1PT} has finite values. In Fig. 6.3 we plot the difference between the density expression in Eq. 6.27 and 6.30, for this special choice of parameters. This plot confirms that the TD limit has been properly taken and all prefactors have been correctly accounted for. The density that results from the sum in Eq. 6.27 is heavily influenced by its finite size nature and the existence of both boundaries. In the case when we take the TD limit in Eq. 6.30 we effectively have a semi-infinite system that extends from only the left boundary while the second boundary is at infinity.

Performing the analysis of the density for a certain choice of sites seems unsatisfactory. Especially because we know that Eq. 6.27 should, in principle, have a well defined TD limit. Luckily, the singularities can be lifted with a suitable transformation in the 2D plane. In fact, there exists a set of transformation, described in Appendix A, to do exactly that.

[5] Which form the dominant envelope in this case; see Sect. 5.1.2.

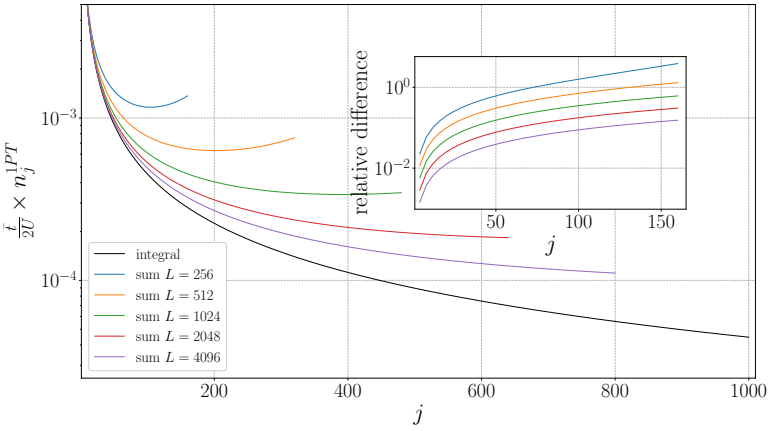

Figure 6.3: Comparison between the density computed with Eqs. 6.27 and 6.30. Dominant envelope at quarter filling plotted. Only part of the density is presented, the remaining part is symmetric across the middle of the chain. Inset: relative difference between the sum and the integral. As we increase L we get closer to the TD limit result.

In particular, we use the Duffy transformation which completely removes the singularity and allows for a numerical evaluation to high precision of the relevant integrals. The validity of this 'regularization' procedure is verified by comparing to the direct evaluation of Eq. 6.30 for those j for which the integrand is finite, see Fig. 6.3.

When it comes to the analytical treatment of the integral in Eq. 6.30 only an asymptotic treatment can be performed, which is based on the steepest descent method and is described in Appendix B. This procedure provides the correct value for the integral and the density in the $j \to \infty$ limit. We present the results for two different cases next in Sect. 6.1.5 and 6.1.4. However, we note that in order to perform the asymptotic analysis we need to start from the original integral still containing the singularity because the asymptotic analysis relies on the presence of the pole structure.

6.1.4 General-filling (generic) case

For filling $\nu \neq 1/2$ the density is computed as

$$n_j^{\mathrm{1PT}} = \frac{U}{t\pi^2}\int_0^{k_\mathrm{F}} \mathrm{d}k \int_{k_\mathrm{F}}^{\pi} \mathrm{d}k' \frac{\sin(kj)\sin(k'j)}{\cos(k')-\cos(k)}\sigma_{k,k'}^{\mathrm{HF}} \tag{6.32}$$

$$\begin{aligned}\sigma_{k,k'}^{\mathrm{HF}} = &-\left\{\cos(k-k')-\cos\left(\frac{k+k'}{2}\right)\right\}\theta\left(k_\mathrm{F}-\frac{(k'-k)}{2}\right)\\ &+\left\{\cos(k+k')-\cos\left(\frac{k-k'}{2}\right)\right\}\theta\left(k_\mathrm{F}-\frac{(k+k')}{2}\right)\end{aligned}$$

Notice the absence of the Umklapp terms, i.e. the *lower* triangle terms[6]. By applying the theta functions in Eq. 6.32 we obtain multiple integrals on separate domains. Some of those integrals are defined on domains that do not contain the singularity at $k = k' = k_\mathrm{F}$ in the integrand. Those integrals can be shown to give an asymptotic contribution of order j^{-2} using the common integration by parts[7]. Those integrals which contain the pole at $(k_\mathrm{F}, k_\mathrm{F})$ have a leading asymptotic behavior of order j^{-1}. They can be treated with the steepest descent method in Appendix B.1 on the rectangular domains and in Appendix B.2 on the triangular domains. There exist only two integrals that contain the pole and are given over the rectangular[8] domain, one from the Hartree and one from the Fock terms, and those are

$$I_{\mathrm{S}}^{\mathrm{H}} = -\int_0^{k_\mathrm{F}} \mathrm{d}k \int_{k_\mathrm{F}}^{2k_\mathrm{F}} \mathrm{d}k' \frac{\sin(kj)\sin(k'j)}{\cos(k')-\cos(k)}\cos(k-k'), \tag{6.33}$$

$$I_{\mathrm{S}}^{\mathrm{F}} = \int_0^{k_\mathrm{F}} \mathrm{d}k \int_{k_\mathrm{F}}^{2k_\mathrm{F}} \mathrm{d}k' \frac{\sin(kj)\sin(k'j)}{\cos(k')-\cos(k)}\cos\left(\frac{k+k'}{2}\right). \tag{6.34}$$

[6] Graphically this is immediate if one superimposes Fig. 6.1 and Fig. 6.2, the Umklapp term away from half-filling does not fall into the colored part of the matrix in Fig. 6.2.

[7] Similarly as in Eq. B.6.

[8] In this particular case a square, the subscript S denotes this fact.

Their asymptotic solutions read

$$I_{\mathrm{S}}^{\mathrm{H}} \approx -\frac{\pi}{4j\sin(k_{\mathrm{F}})}\cos(2jk_{\mathrm{F}}), \tag{6.35}$$

$$I_{\mathrm{S}}^{\mathrm{F}} \approx \frac{\pi\cos(k_{\mathrm{F}})}{4j\sin(k_{\mathrm{F}})}\cos(2jk_{\mathrm{F}}). \tag{6.36}$$

Furthermore, there are two integrals given over the triangular domain that contain the pole and those are

$$I_{\mathrm{T}}^{\mathrm{H}} = \int_0^{k_{\mathrm{F}}} \mathrm{d}k \int_{k_{\mathrm{F}}}^{2k_{\mathrm{F}}-k} \mathrm{d}k' \frac{\sin(kj)\sin(k'j)}{\cos(k')-\cos(k)}\cos(k+k'), \tag{6.37}$$

$$I_{\mathrm{T}}^{\mathrm{F}} = -\int_0^{k_{\mathrm{F}}} \mathrm{d}k \int_{k_{\mathrm{F}}}^{2k_{\mathrm{F}}-k} \mathrm{d}k' \frac{\sin(kj)\sin(k'j)}{\cos(k')-\cos(k)}\cos\left(\frac{k-k'}{2}\right), \tag{6.38}$$

Their asymptotic solutions contain a logarithmic factor in the position and read as

$$\begin{aligned} I_{\mathrm{T}}^{\mathrm{H}} \approx{}& \frac{\pi\cos(2k_{\mathrm{F}})}{8j\sin(k_{\mathrm{F}})}\cos(2jk_{\mathrm{F}}) \\ &+ \frac{\cos(2k_{\mathrm{F}})}{4j\sin(k_{\mathrm{F}})}\left[\ln j+\gamma+\ln\left(4\tan\frac{k_{\mathrm{F}}}{2}\right)\right]\sin(2jk_{\mathrm{F}}), \end{aligned} \tag{6.39}$$

$$\begin{aligned} I_{\mathrm{T}}^{\mathrm{F}} \approx{}& -\frac{\pi}{8j\sin(k_{\mathrm{F}})}\cos(2jk_{\mathrm{F}}) \\ &- \frac{1}{4j\sin(k_{\mathrm{F}})}\Big[\ln j+\gamma+\ln(2\sin k_{\mathrm{F}})\Big]\sin(2jk_{\mathrm{F}}), \end{aligned} \tag{6.40}$$

where $\gamma \approx 0.577...$ which is the Euler-Mascheroni constant. In Fig. 6.4 we compare the asymptotic with the numerical results for the four integrals presented here.

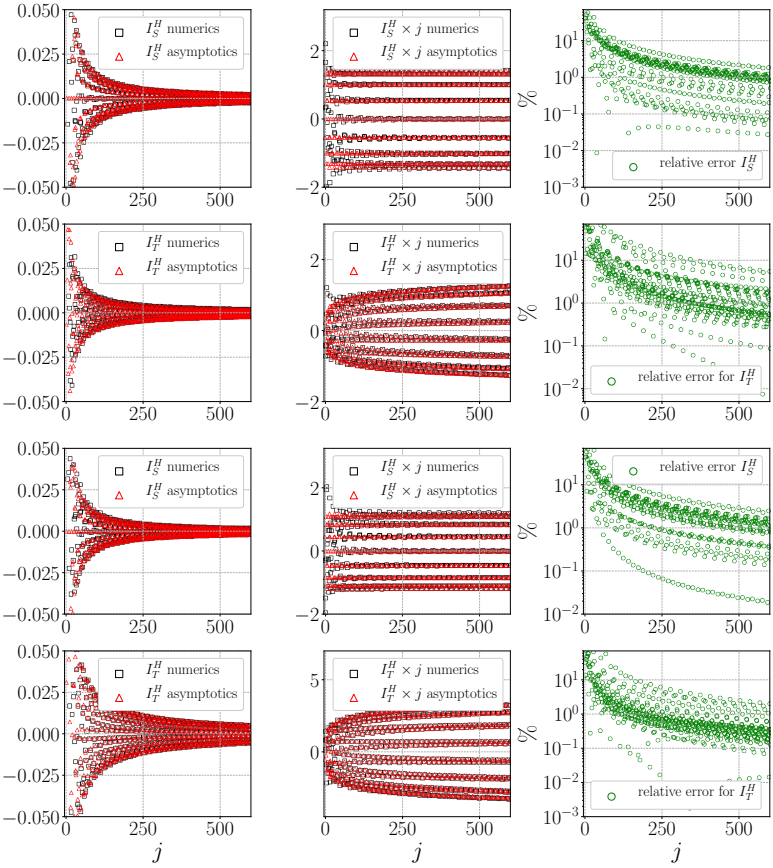

Figure 6.4: Numerics vs. asymptotics of the integrals in Eq. 6.33-6.34 and Eq. 6.37-6.38 for a generic $\nu = \frac{3}{16}$ filling. Numerics performed for every j by using the transformations in Appendix A. Relative and absolute precision set at 10^{-12}. Asymptotics accessed by techniques in Appendix B. First column: density envelopes; second column: density envelopes multiplied with the site index j; third column: relative error made between asymptotics and numerics

Adding up all the contributions

$$I = \frac{\bar{t}\pi^2}{U} n_j^{1\mathrm{PT}} = I_{\mathrm{S}}^{\mathrm{H}} + I_{\mathrm{S}}^{\mathrm{F}} + I_{\mathrm{T}}^{\mathrm{H}} + I_{\mathrm{T}}^{\mathrm{F}}, \tag{6.41}$$

we arrive at

$$\begin{aligned} I \approx & \frac{\pi}{4j\sin(k_{\mathrm{F}})}\left[-\frac{3}{2} + \cos k_{\mathrm{F}} + \frac{\cos(2k_{\mathrm{F}})}{2}\right]\cos(2jk_{\mathrm{F}}) \\ & + \frac{1}{4j\sin(k_{\mathrm{F}})}\Big(\ln j + \gamma\Big)\Big(\cos(2k_{\mathrm{F}}) - 1\Big)\sin(2jk_{\mathrm{F}}) \\ & + \frac{1}{4j\sin(k_{\mathrm{F}})}\left[\cos(2k_{\mathrm{F}})\ln\left(4\tan\frac{k_{\mathrm{F}}}{2}\right) - \ln(2\sin k_{\mathrm{F}})\right]\sin(2jk_{\mathrm{F}}) \\ & + \mathcal{O}(j^{-2}). \end{aligned} \tag{6.42}$$

It is important to note that only the integrals $I_{\mathrm{T}}^{\mathrm{H}}$ and $I_{\mathrm{T}}^{\mathrm{F}}$ have asymptotic terms of the form $\ln j/j$. The key observation is that the triangular region needs to have a pole at one of the vertices for a logarithmic contribution to occur.

Interestingly, the asymptotic results away from half-filling are in agreement with known field theory predictions. In particular, if we isolate the dominant term in Eq. 6.42 it follows that the density reads

$$n_j^0 + n_j^{1\mathrm{PT}} = \nu - \frac{\sin(2k_{\mathrm{F}}j)}{2\pi j}\left(1 + \frac{U\big[1-\cos(2k_{\mathrm{F}})\big]}{2\pi t\sin(k_{\mathrm{F}})}\ln(j)\right), \tag{6.43}$$

which is consistent, at linear order in interaction, with the bosonization result in Eq. 5.2 after we identify the Luttinger parameter as

$$K = 1 - \frac{U}{\pi v_{\mathrm{F}}}\big[1-\cos(2k_{\mathrm{F}})\big], \tag{6.44}$$

where $v_{\mathrm{F}} = 2t\sin(k_{\mathrm{F}})$ is the Fermi velocity. At half-filling, the Luttinger parameter in Eq. 6.44 matches with the prediction from BA in Eq. 3.50, after we expand to obtain the first order correction in U. Furthermore, from the *boundary exponent* α_{B} in Ref. [MMS+00],

an equivalent expression[9] for the Luttinger parameter to Eq. 6.44, can be derived according to

$$\alpha_B = \frac{1}{K} - 1, \quad \text{and} \quad \alpha_{\mathrm{B}} = \frac{U}{\pi v_{\mathrm{F}}}[1 - \cos(2k_{\mathrm{F}})], \tag{6.45}$$

for small U.

Similar conclusion has been made by the authors in Refs. [SMM+00] and [MMS+00] regarding the generation of the logarithmic correction in the frequency ω of the LDOS. In particular, a triangular structure in the self-energy with a pole at the vertex was identified to be essential. Moreover, they showed that in the 'full inversion' Hartree-Fock approximation the logarithmic corrections are summed up to produce a power law in the LDOS. In Sect. 7, with high energy resolution calculations we provide evidence that this is not the case for the density.

This result can be viewed as another example[10] where perturbation theory in systems with OBC produces logarithmic divergence, in this case in the site index $\ln(j)$, with a prefactor that is *first* -order in the interaction. In systems with PBC the divergence occurs in *second*-order perturbation theory and is a direct consequence of a singular self-energy; see Ref. [Sól79]. However, in the case of OBC the self-energy is not singular but is rather characterized by an extended structure which through an involved matrix inversion leads to the singularities in the leading order.

6.1.5 Half-filling (non-generic) case

For half-filling ($\nu = 1/2$) the first order correction to the density reduces to

$$n_j^{\mathrm{1PT}} = \frac{U}{t\pi^2} \int_0^{\frac{\pi}{2}} \mathrm{d}k \int_{\frac{\pi}{2}}^{\pi} \mathrm{d}k' \frac{\sin(kj)\sin(k'j)}{\cos(k') - \cos(k)} \sigma^{\mathrm{HF}}_{k,k'}, \tag{6.46}$$

$$\sigma^{\mathrm{HF}}_{k,k'} = -2\sin(k)\sin(k') + \cos(k/2)\cos(k'/2) - \sin(k/2)\sin(k'/2).$$

The self-energy was simplified by noticing that the Fock terms (second terms in the *upper* and *lower* triangles) are equal except

[9] In the same order of interaction.

[10] Alongside to the LDOS; see Sect. 5.24

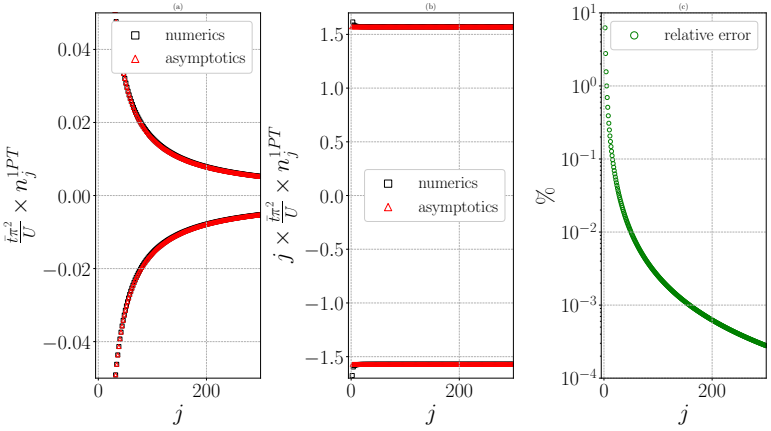

Figure 6.5: Numerics of Eq. 6.46 vs. asymptotics in Eq. 6.47 at half-filling. Numerics performed for every j by using the transformations in Appendix A. Relative and absolute precision set at 10^{-12}. Asymptotics accessed by techniques in Appendix B. a.) density envelopes, b.) density envelopes multiplied with the site index j, c.) relative error made between asymptotics and analytics.

for a minus sign, thereby canceling each other's contribution. On the other hand, at half-filling, the Hartree terms (*upper* and *lower* triangle) together form a full square region instead of individual triangular ones. The *strip* contribution is an integration on the same square integration region.

The asymptotic analysis, $j \to \infty$, of Eq. 6.46 yields

$$\frac{\bar{t}\pi^2}{U} n_j^{1\mathrm{PT}} \approx -\frac{\pi}{2} \frac{\cos(\pi j)}{j}. \tag{6.47}$$

The asymptotics of the integral is checked against the numerics in Fig. 6.5. The numerical solutions of the integral quickly converge to the asymptotic result. Given that we are able to obtain the asymptotic approximation for the integral we write down the density

to first order in the self-energy (first order in U) which reads

$$n_j^{\mathrm{HF}} = \frac{1}{2} - \frac{U}{2t\pi}\frac{\cos(\pi j)}{j} + \mathcal{O}(j^{-2}). \tag{6.48}$$

This result for the density is inconsistent with the field theory prediction of Eq. 5.2 according to which we expect to obtain a logarithmic correction of $\ln(j)$ in leading order of the interaction; as we did in Sect. 6.1.4.

A particularly simple way to deal with the non-generic density decay at half-filling is to perform the perturbation theory starting from a slightly different Hamiltonian. This new Hamiltonian is equipped with an approprite non-interacting basis that helps us understand the result we obtained in Eq. 6.48.

6.2 Interacting ground state density at half-filling

We describe how to perform the perturbative treatment at half-filling for the microscopic spinless fermion model with nearest-neighbor interactions. In particular, to recover the logarithmic corrections in Eq. 6.48 we treat a single site impurity in our system. We show that we can use the strength of the single-particle impurity potential as an control parameter, through which we are able to move from a non-generic to generic regime.

6.2.1 Non-interacting states ansatz

We model our single impurity of strength V to be at the first site of the open boundary chain as

$$\hat{H}^0 + \hat{V} = -t\sum_{j=1}^{L}\left(\hat{c}_{j+1}^\dagger \hat{c}_j + \hat{c}_j^\dagger \hat{c}_{j+1}\right) + V\hat{c}_1^\dagger \hat{c}_1. \tag{6.49}$$

The first site has been chosen for computational convenience. We proceed to calculate the eigenstates of this particular non-interacting Hamiltonian in preparation for the perturbative treatment. We make

an ansatz for the possible form of the eigenstates as

$$|k\rangle = \sum_{j=1}^{L} a_j |j\rangle; \quad a_j = A \sin(kj + \bar{\delta}), \tag{6.50}$$

where A is the normalization constant. Furthermore, $\bar{\delta} = \bar{\delta}(V, t, k)$ is a phase which depends on the momentum and the impurity details. By solving the Schrödinger equation (for all momenta k) we obtain the dispersion relation $\epsilon(k) = -2t\cos(k)$, the phase shift

$$\bar{\delta}(V, t, k) = \arctan\left(\frac{\sin(k)}{\cos(k) + V/t}\right) - k, \quad \text{with} \quad \delta = \bar{\delta} + k, \tag{6.51}$$

and the discretization condition $k \equiv k_n = \frac{n\pi}{L} - \frac{\delta(k_n)}{L}$. The discretization condition on the momentum is an implicit equation which we have to solve numerically. From the normalization requirement and our ansatz for the states the normalization 'constant' reads

$$A = \left(\frac{L}{2} - \frac{\cos\left[2\delta(k_n) + k_n(L-1)\right]\sin(k_n L)}{2\sin(k_n)}\right)^{-1/2}. \tag{6.52}$$

In the limits $V \to 0$ and $V \to \infty$ the well-known eigenstates, the momentum discretization and normalization of the free system are recovered. However, in the infinite impurity potential ($V \to \infty$) case the particles have a vanishing probability amplitude to occupy the first site, effectively leaving us with a free system of $L-1$ sites. We verified that these are the correct finite size states (for any L) by comparing them to numerically obtained eigenstates. For large but finite L the states take up a simpler form

$$a_j = \langle j|n\rangle = \sqrt{\frac{2}{L+1}}\sin\left[(j-1)k_n + \delta(k_n)\right], \tag{6.53}$$

where $k_n = \frac{n\pi}{L+1}$. We use these states in our further perturbative considerations. They reduce to the impurity free states in two different impurity strength limits which we use to check our derivations; see Sect. 6.2. Furthermore, the states are consistent with the ones derived in [ZA97].

6.2.2 Non-interacting density

The presence of an impurity breaks the particle-hole symmetry and introduces Friedel oscillations in the density at half-filling. Given the states in Eq. 6.53 we are able to explicitly evaluate the non-interacting impurity Green's function and consequently the density according to

$$n_j^0 = \frac{1}{2} + \frac{1}{\pi}\int_0^\infty d\omega \mathrm{Re}\big[G^0_{j,j}(i\omega)\big], \tag{6.54}$$

where

$$G^0_{j,j}(i\omega) = \sum_{n,n'=1}^{L} \langle j|n\rangle\langle n'|j\rangle G^0_{n,n'}(i\omega)\delta_{n,n'}. \tag{6.55}$$

The impurity-free non-interacting Green's function is diagonal, and we obtain[11]

$$n_j^0 = \frac{1}{2} + \frac{1}{\pi(L+1)}\int_0^\infty d\omega \mathrm{Re}\left[\sum_{n=1}^{L}\frac{1}{i\omega - \xi(k_n)} - \frac{\cos\big[2(j-1)k_n + 2\delta(k_n)\big]}{i\omega - \xi(k_n)}\right]. \tag{6.56}$$

The first term in the square bracket is trivial and gives zero in the half-filling case. The second term is more interesting and we compute it to be

$$\int_0^\infty d\omega \mathrm{Re}\left[\sum_{n=1}^{L}\frac{\cos\big[2(j-1)k_n + 2\delta(k_n)\big]}{i\omega - \xi(k_n)}\right]$$
$$= \frac{\pi}{2}\sum_{n=1}^{L}\cos\big[2(j-1)k_n + 2\delta(k_n)\big]\big(\theta(n-N) - \theta(N-n)\big). \tag{6.57}$$

We cannot directly evaluate the sum due to the non-trivial momentum dependence of the phase shift. Instead, we evaluate the

[11] Similarly to Eq. 5.7.

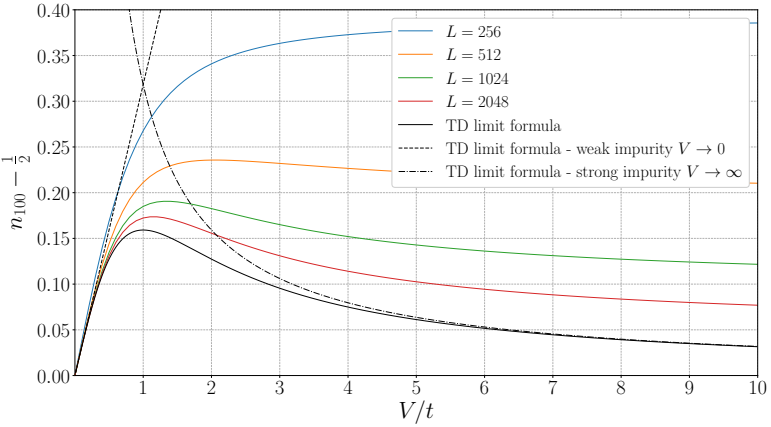

Figure 6.6: Plot of the density amplitude at site $j = 100$. The finite size results are in qualitative agreement with the TD analytical result in Eq. 6.54. By increasing the system size the numerical results get closer to the analytic formula result. At $V \to 0$ we are at the particle-hole symmetric point. At $V \to \infty$ we recover particle-hole symmetry again.

expression in TD limit, where the sum turns into an integral. In this way, we obtain the density at half-filling to the leading order in $1/j$ as[12]

$$n_j^0 = \frac{1}{2} + \frac{\cos(\pi j)}{2\pi j} \sin\left[2 \arctan\left(V^{-1}\right)\right] + \mathcal{O}(j^{-2}) \tag{6.58}$$

In both relevant limits (weak and strong impurity) we recover the impurity-free result at half-filling; see Eq. 5.11. The derived expression for the density is valid for all values of V and is in qualitative agreement with the numerical diagonalization, as shown in Fig. 6.6. Expanding around the two different impurity limits, the weak and

[12] With a site impurity at the first site.

the strong, yields

$$\lim_{V\to 0} n_j^0 = \frac{1}{2} + \frac{V\cos(\pi j)}{\pi j} + \mathcal{O}\Big(V^3\Big), \tag{6.59}$$

$$\lim_{V\to \infty} n_j^0 = \frac{1}{2} + \frac{\cos(\pi j)}{V\pi j} + \mathcal{O}\Big(V^{-3}\Big). \tag{6.60}$$

The density amplitude depends linearly on V and $1/V$ followed by a cubic term, respectively.

The same asymptotic expressions for the density can be derived using the scattering T-matrix approach (at first Born approximation level) described in [BF04] and [Eco06]. However, the T-matrix encodes the effects of the impurity through the Green's function rather than the states.

6.2.3 Perturbation theory

Given the asymptotic states in presence of a site impurity in Eq. 6.53 we are able to follow the same steps as in Ch. 6.1.1 and derive the expression for the self-energy (for large L) to first order as

$$\frac{(L+1)\Sigma^{\mathrm{HF}}_{n,n'}}{U} = \left\{ L - \sum_{m=1}^{L/2} \Big(\cos(k_n - k_m) + \cos(k_n + k_m) \Big) \right\} \delta_{n,n'}$$
$$- \left\{ \cos\left[(k_n - k_{n'}) + \delta(k_{n'}) - \delta(k_n) - 2\delta\left(\frac{k_{n'} - k_n}{2} \right) \right] \right.$$
$$\left. - \cos\left[\left(\frac{k_n + k_{n'}}{2} \right) + \delta(k_{n'}) - \delta(k_n) - 2\delta\left(\frac{k_{n'} - k_n}{2} \right) \right] \right\} f\left(\frac{n' - n}{2} \right)$$

$$
\begin{aligned}
&- \Bigg\{ \cos\left[(k_n - k_{n'}) + \delta(k_{n'}) - \delta(k_n) + 2\delta\left(\frac{k_{n'} - k_n}{2}\right)\right] \\
&- \cos\left[\left(\frac{k_n + k_{n'}}{2}\right) + \delta(k_{n'}) - \delta(k_n) + 2\delta\left(\frac{k_{n'} - k_n}{2}\right)\right]\Bigg\} f\left(\frac{n - n'}{2}\right) \\
&+ \Bigg\{ \cos\left[(k_n + k_{n'}) - \delta(k_{n'}) - \delta(k_n) + 2\delta\left(\frac{k_{n'} + k_n}{2}\right)\right] \\
&- \cos\left[\left(\frac{k_n - k_{n'}}{2}\right) - \delta(k_{n'}) - \delta(k_n) + 2\delta\left(\frac{k_{n'} + k_n}{2}\right)\right]\Bigg\} f\left(\frac{n + n'}{2}\right) \\
&+ \Bigg\{ \cos\left[(k_n + k_{n'}) - \delta(k_{n'}) - \delta(k_n) - 2\delta\left(\pi - \frac{k_{n'} + k_n}{2}\right)\right] \\
&+ \cos\left[\left(\frac{k_n - k_{n'}}{2}\right) - \delta(k_{n'}) - \delta(k_n) - 2\delta\left(\pi - \frac{k_{n'} + k_n}{2}\right)\right]\Bigg\} \\
&\times f\left(L + 1 - \frac{n + n'}{2}\right).
\end{aligned}
\tag{6.61}
$$

The difference between the self-energy expression in Eq. 6.12 and 6.61 is the presence of the phase shift δ which encodes the impurity details. The structures in the self-energy remain the same as in Fig. 6.1 just modulated by the phase δ. However, the diagonal part of the self-energy remains impurity independent. As expected, there is no effective renormalization of the bulk hopping and chemical potential due to the presence of a single site impurity at the Hartree-Fock level. The phase shift δ is an antisymmetric function with $\delta(\pi + x) = -\delta(x)$. We use this property to show that in the limit $V \to 0$ we recover the impurity free results. In the strong impurity limit, $V \to \infty$, we arrive to the same impurity free results with an effective system size of $L - 1$ instead of L.

The density is similarly computed to the impurity free case and reads

$$\frac{\bar{t}\pi^2}{U} n_j^{\mathrm{1PT}} = \frac{1}{2} \int_0^{\pi/2} \int_{\pi/2}^{\pi} \frac{\sigma^{\mathrm{HF}}_{k,k'}}{\cos(k') - \cos(k)} \times \sin\Big(k(j-1) + \delta(k,V)\Big) \sin\Big(k'(j-1) + \delta(k',V)\Big) \mathrm{d}k \mathrm{d}k', \tag{6.62}$$

where we have taken the TD limit and redefined $(L+1)\Sigma^{\mathrm{HF}}_{n,n'} = \sigma^{\mathrm{HF}}_{k,k'}$. The prefactor of $1/2$ is, however, present because the self-energy matrix, due to the phase shift, is not symmetric under the exchange of indices $n \to n'$; see Eq. 6.26.

The results of the numerical evaluation of Eq. 6.62 for different impurity strengths are presented in Fig. 6.7. The impurity free result is recovered for vanishing impurity strength, while for finite impurity strength qualitatively different envelopes can be observed. In particular, we observe a monotonic increase (instead of a constant) of the $j \times n_j$, which hints at a $\ln(j)/j$ term in the density. We analyze the asymptotic behavior to confirm this in see Sect. 6.2.4.

Furthermore, we note that an interchange between the upper and lower envelopes (odd and even sites) happens for finite impurity strength. This can be observed in Fig. 6.7 if we compare the values in the plot for $j = 100$. For the impurity free case this point belongs to the lower envelope (not shown in the plot) while for any finite impurity strength at this site a point is present in the upper density envelope. To illustrate this we evaluate $j \times \frac{\bar{t}\pi^2}{U} \times n_j^{\mathrm{1PT}}$ at $j = 99$ and at $j = 100$ and compare it to the impurity free envelopes in Fig. 6.8. Both envelops reach their maximum at $V = 1$ where a qualitative change occurs, and this crossover signals a transition between weak and strong impurity physics. In the non-interacting case this kind of crossover is present as well and can be seen in Fig. 6.6 but without the sign change. Moreover, in Sect. 6.2.4 we derive the asymptotic density which gives further gives support to the presence of a crossover.

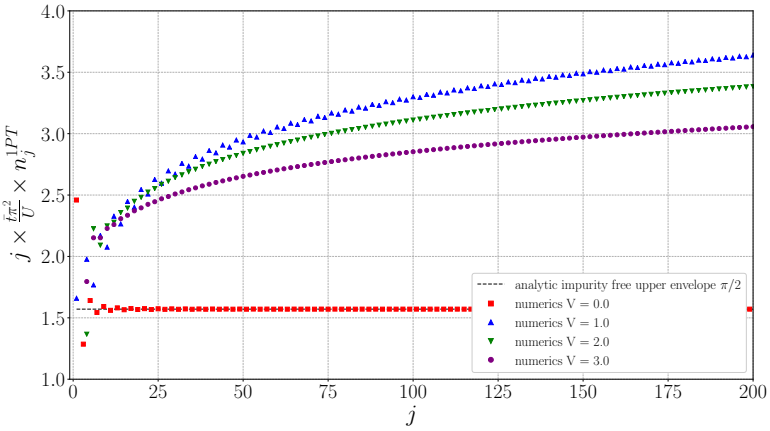

Figure 6.7: Numerical evaluation of the integral in Eq. 6.62 for different impurity strengths. Upper envelop plotted. Impurity free asymptotic result of the integral in Eq. 6.47.

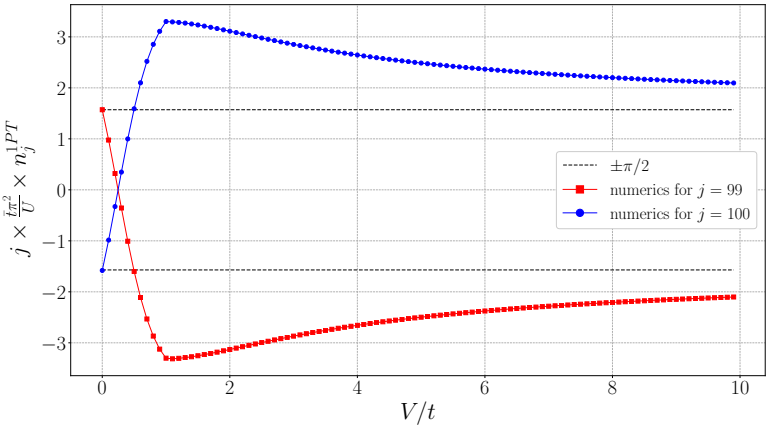

Figure 6.8: Numerical solution of Eq. 6.62 at sites $j = 99$ and $j = 100$ for different impurity strengths. An inversion between the lower and upper envelope can be observed (odd and even). In limits $V \to 0$ and $V \to \infty$ impurity free results can be obtained but with a sign difference in $V \to \infty$ case.

6.2.4 Asymptotics of the perturbation theory

The logarithmic contribution in Eq. 6.62 (self-energy part of the integrand) comes from the triangular structures[13]. Furthermore, it can be shown that, by exploiting the properties of the phase shift, the Fock contributions from the upper and lower triangles are equal but have opposite sign leading to a vanishing contribution. Thus, the only relevant terms are the Hartree ones and the upper and lower triangle ones. Therefore, to extract the leading asymptotics we can exclusively focus on the upper triangle Hartree term. For computing the first order correction to the density we need evaluate

$$\frac{\bar{t}\pi^2}{U} n_j^{\mathrm{1PT}} \approx \int_0^{k_\mathrm{F}} \int_{k_\mathrm{F}}^{2k_\mathrm{F}-k} \frac{\cos\left[k + k' - \delta(k') - \delta(k) + 2\delta\left(\frac{k+k'}{2}\right)\right]}{\cos(k') - \cos(k)} \times \sin\Big(k(j-1) + \delta(k,V)\Big) \sin\Big(k'(j-1) + \delta(k',V)\Big) \mathrm{d}k\mathrm{d}k'. \tag{6.63}$$

We keep using k_F for convenience but note that $k_\mathrm{F} = \pi/2$. To compute the integral we apply the steps as described in Appendix B and arrive at

$$I_1 = \frac{e^{2i(j-1)k_\mathrm{F}}}{4} \int_0^\infty \mathrm{d}(iy') e^{-(j-1)y'} \int_0^{k_\mathrm{F}} \frac{\mathrm{d}k e^{i\delta(k_\mathrm{F}-k)} e^{i\delta(k_\mathrm{F}+k+iy')}}{\cos(k_\mathrm{F}+k+iy') - \cos(k_\mathrm{F}-k)} \tag{6.64}$$

$$\times \cos\left[2k_\mathrm{F} + iy' + 2\delta\left(k_\mathrm{F} + \frac{iy'}{2}\right) - \big(\delta(k_\mathrm{F}+k+iy') + \delta(k_\mathrm{F}-k)\big)\right], \tag{6.65}$$

where $\frac{\bar{t}\pi^2}{U} n_j^{\mathrm{1PT}} = 2\mathrm{Re}\big[I_1\big]$. In the relevant limits ($V \to 0$, $V \to \infty$) we are able to recover the impurity free integral. We proceed by solving the inner integral over k, however, we first use trigonometric

[13] As was the case away from half-filling; see Sect. 6.1.4

identities to arrive at

$$
\begin{aligned}
&- \frac{\cos\left[2k_{\mathrm{F}} + iy' + 2\delta\left(k_{\mathrm{F}} + \frac{iy'}{2}\right)\right]}{4\sin\left(k_{\mathrm{F}} + \frac{iy'}{2}\right)} \\
&\times \left\{ \int_0^{k_{\mathrm{F}}} \frac{\mathrm{d}k}{\sin\left(k + \frac{iy'}{2}\right)} + \int_0^{k_{\mathrm{F}}} \mathrm{d}k \frac{e^{2i[\delta(k_{\mathrm{F}}-k)+\delta(k_{\mathrm{F}}+k+iy')]}}{\sin\left(k + \frac{iy'}{2}\right)} \right\} \\
&- \frac{\sin\left[2k_{\mathrm{F}} + iy' + 2\delta\left(k_{\mathrm{F}} + \frac{iy'}{2}\right)\right]}{4i\sin\left(k_{\mathrm{F}} + \frac{iy'}{2}\right)} \\
&\times \left\{ \int_0^{k_{\mathrm{F}}} \mathrm{d}k \frac{e^{2i[\delta(k_{\mathrm{F}}-k)+\delta(k_{\mathrm{F}}+k+iy')]}}{\sin\left(k + \frac{iy'}{2}\right)} - \int_0^{k_{\mathrm{F}}} \frac{\mathrm{d}k}{\sin\left(k + \frac{iy'}{2}\right)} \right\}. \qquad (6.66)
\end{aligned}
$$

Two out of the four integrals can be solved in the TD limit by using $\int \frac{dx}{\sin(x)} = \ln\tan\left(\frac{x}{2}\right)$. The interesting terms are the two remaining ones that contain the exponentials. These two terms are in fact extremely difficult to evaluate in the TD limit due to the momentum dependent phase shift δ. Therefore, we focus our attention on the two limits of weak and strong impurity, where the phase shift simplifies greatly and allows for the asymptotic analysis.

Weak impurity limit $V \to 0$

We expand the phase shift in this limit, $\delta(k) = k - \sin(k)V + \mathcal{O}(V^2)$, which after some trigonometric transformation, leads to

$$
\begin{aligned}
&\int_0^{k_{\mathrm{F}}} \mathrm{d}k \frac{e^{2i[\delta(k_{\mathrm{F}}-k)+\delta(k_{\mathrm{F}}+k+iy')]}}{\sin\left(k + \frac{iy'}{2}\right)} \approx e^{2i\pi} e^{-2y'} \\
&\times \int_0^{\frac{\pi}{2}} \frac{e^{-4iV\cos\left(\frac{iy'}{2}\right)\cos\left(k+\frac{iy'}{2}\right)}}{\sin\left(k + \frac{iy'}{2}\right)} \mathrm{d}k. \qquad (6.67)
\end{aligned}
$$

This integral enjoys an exact representation in terms of trigonometric integrals[14] Si and Ci for $\{y' \in \mathbb{R}, y' > 0\}$ and $\{V \in \mathbb{R}, V > 0\}$ as

$$
\begin{aligned}
M(y,V) \equiv & \int_0^{\frac{\pi}{2}} \frac{e^{-4iV\cos\left(\frac{iy'}{2}\right)\cos\left(k+\frac{iy'}{2}\right)}}{\sin\left(k+\frac{iy'}{2}\right)}\mathrm{d}k = \frac{1}{2}e^{-4iV\cosh\left(\frac{y}{2}\right)} \\
& \times \Bigg\{ e^{8iV\cosh\left(\frac{y}{2}\right)} \Bigg(\mathrm{Ci}\left[4V\cosh\left(\frac{y}{2}\right) + 2V\cosh(y) + 2V\right] \\
& - \mathrm{Ci}\left[4V\cosh\left(\frac{y}{2}\right) - 2iV\sinh(y)\right] \\
& - i\Bigg(\mathrm{Si}\left[2V(2\cosh\left(\frac{y}{2}\right) + \cosh(y) + 1)\right] \\
& + \mathrm{Si}\left[2iV\sinh(y) - 2V\mathrm{csch}\left(\frac{y}{2}\right)\sinh(y)\right]\Bigg)\Bigg) \\
& - \mathrm{Ci}\left[-8V\cosh\left(\frac{y}{2}\right)\sinh^2\left(\frac{y}{4}\right)\right] + \mathrm{Ci}\left[4V\cosh\left(\frac{y}{2}\right) + 2iV\sinh(y)\right] \\
& + i\Bigg(\mathrm{Si}\left[-4V\cosh\left(\frac{y}{2}\right) + 2V\cosh(y) + 2V\right] \\
& + \mathrm{Si}\left[4V\cosh\left(\frac{y}{2}\right) + 2iV\sinh(y)\right]\Bigg)\Bigg\}. \qquad (6.68)
\end{aligned}
$$

With this identification we write the I_1 term as

$$
\begin{aligned}
I_1 \approx & -\frac{e^{i\pi(j+1)}}{16}\int_0^{\infty} \mathrm{d}(iy')e^{-(j+1)y'}\frac{e^{i\left[2\pi+2iy'-2\cos\left(\frac{iy'}{2}\right)V\right]}}{\cos\left(\frac{iy'}{2}\right)} \\
& \times \ln\left[\frac{\tan\left(\frac{\pi}{4}+\frac{iy'}{4}\right)}{\tan\left(\frac{iy'}{4}\right)}\right]
\end{aligned}
$$

[14] See Eq. 6.2.9 and 6.2.11 of Ref. [DL] for the definitions.

$$-\frac{e^{i\pi(j+1)}}{16}\int_0^\infty \mathrm{d}(iy')e^{-(j+1)y'}\frac{e^{-i\left[2\pi+2iy'-2\cos\left(\frac{iy'}{2}\right)V\right]}}{\cos\left(\frac{iy'}{2}\right)}M(y,V). \tag{6.69}$$

If we now change the integration variable to $t = y'(j+1)$ and take the limit $j \to \infty$, we effectively expand the integrand around $t = 0$. For the dominant term in the asymptotic limit we then obtain

$$I_1 \approx -\frac{ie^{i[\pi(j+1)-2V]}}{8}\frac{[\gamma+\ln(j+1)]}{j+1}+... \tag{6.70}$$

Taking the real part we obtain the dominant asymptotic contribution of the density in Eq. 6.63, in the weak impurity case, as[15]

$$\frac{\bar{t}\pi^2}{U}n_j^{1\mathrm{PT}}(V\to 0)\approx\frac{\ln(j)}{4j}\sin(\pi j-2V). \tag{6.71}$$

It differs from the one in Eq. 6.42 by a finite phase shift in the sine which, for finite impurity strength, makes the prefactor to the logarithm non-vanishing. This finite phase provides the mechanism of breaking the particle-hole symmetry. In the limit $V \to 0$ we recover the impurity free result for half-filling.

[15] This expression is similar to the one we derive in Sect. 6.1.4, but valid for half-filling.

Strong impurity limit $V \to \infty$

The phase shift in this limit reads $\delta(k) = \dfrac{\sin k}{V} + \mathcal{O}(V^{-2})$. The integral that we need to solve now reads

$$\int_0^{k_F} \mathrm{d}k \frac{e^{2i(\delta(k_F-k)+\delta(k_F+k+iy'))}}{\sin\left(k+\frac{iy'}{2}\right)} \approx \int_0^{\frac{\pi}{2}} \frac{e^{4iV^{-1}\cos\left(\frac{iy'}{2}\right)\cos\left(k+\frac{iy'}{2}\right)}}{\sin\left(k+\frac{iy'}{2}\right)} \mathrm{d}k \tag{6.72}$$

$$\begin{aligned} &= \frac{1}{2} e^{-4iV^{-1}\cosh\left(\frac{y}{2}\right)} \Bigg\{ \mathrm{Ei}\left[8iV^{-1}\cosh^2\left(\frac{y}{4}\right)\cosh\left(\frac{y}{2}\right)\right] \\ &- \mathrm{Ei}\left[8iV^{-1}\cos^2\left[\frac{1}{4}(iy+\pi)\right]\cosh\left(\frac{y}{2}\right)\right] \\ &+ e^{8iV^{-1}\cosh\left(\frac{y}{2}\right)} \Bigg\{ \mathrm{Ei}\left[-8iV^{-1}\cosh\left(\frac{y}{2}\right)\sin^2\left(\frac{1}{4}(iy+\pi)\right)\right] \\ &- \mathrm{Ei}\left[8iV^{-1}\cosh\left(\frac{y}{2}\right)\sinh^2\left(\frac{y}{4}\right)\right] \Bigg\} \Bigg\}, \end{aligned} \tag{6.73}$$

where Ei denotes the exponential integral[16]. Repeating similar steps as in the weak impurity, case we obtain

$$\frac{\bar{t}\pi^2}{U} n_j^{1\mathrm{PT}}(V\to\infty) \approx \frac{\ln j}{4j} \sin\left(\pi j + \frac{2}{V}\right). \tag{6.74}$$

In this limit we also obtain a finite phase that breaks the particle-hole symmetry and we recover the impurity free result for $V \to \infty$. There is one important difference between the weak and strong impurity results beyond the possible substitution $V \to \frac{1}{V}$, namely a different sign of the finite phase. This sign change is consistent with the numerical results presented in Fig. 6.8.

In Sect. 7.2 we show how the asymptotic density expressions from Eq. 6.71 and 6.74 can help us understand the 'full inversion' Hartree-Fock approximation results.

[16] See Eq. 6.2.6 in Ref. [DL] for the definition.

7 Friedel oscillations in TD limit

In this Chapter, we expand on our findings from Chap. 5 regarding the spinless fermion model with nearest-neighbor interactions. In particular, we improve on the finite size results by attaching a single non-interacting reservoir and adiabatically turning off the interaction. By using this procedure we are able to tell if the power law is present or not in the Hartree-Fock and LDA DFT density.

In Sect. 7.1 we discuss our methodology and in Sect. 7.2 we present and discuss the results. In Sect. 7.2.1 we first apply the described method to LDA DFT and discuss how the low energy asymptotics are consistently evaluated. In Sect. 7.2.3 with the full understanding of the calculation details we discuss the non-generic nature of the Hartree-Fock approximation at half-filling which was one of the main topics in Chap. 6.

7.1 The method

As advertised we focus on the spinless fermion model with nearest-neightbour interactions defined in Eq. 5.1 and couple this finite interacting chain to a non-interacting environment, as explained in Sect. 2.5. Turning the interaction sharply off leads to, for example, a jump in conductance or to unwanted backscattering in the local density from the boundary; see Ref. [EMA+05] for the definition of the conductance in interacting wires and further details on the issue.

Therefore, we employ the smoothening function to the interaction in an effort to model 'perfect' contacts which suppress boundary effects.
The density oscillation decay rates change due to the interactions and the gradual transition to the non-interacting rates ensures that any boundary effects from 'second boundary' have been negated and that we approach the TD limit in a controlled and consistent way. However, to achieve this we first redefine the interacting part of the finite system Hamiltonian as

$$H^{\text{int}} = \sum_{j=1}^{L-1} U_{j,j+1}\Big[n_j - r(\nu,U)\Big]\Big[n_{j+1} - r(\nu,U)\Big]. \tag{7.1}$$

The interaction is only present between the bonds of the sites 1 to L and not in the reservoir. The single-particle potential $r(\nu,U)$ shifts the operator n_j and depends on the filling factor ν and interaction U. We choose r such that the average density in the interacting wire is fixed to ν. Physically, this additional single-particle potential prevents the particles from leaving the interacting wire and precisely counters the effects of the interaction as we move towards the non-interacting reservoir. For the purpose of determining the appropriate r we employ the algorithm in Sect. 2.4.1.

For the nearest-neighbor interaction in Eq. 7.1 we select the following function to achieve the smoothening

$$U_{j,j+1} = U\frac{\arctan\big[(j-j_s)/w\big] - \arctan\big[(1-j_s)/w\big]}{\arctan\big[(L-j_s)/w\big] - \arctan\big[(1-j_s)/w\big]}, \tag{7.2}$$

which $U \to 0$ as we approach L. Similar smoothening function can be used if there is a second lead on the left of the finite system. U is the bulk interaction of the lattice system and w and j_s are usually left as a choice. Parameters w and j_s are chosen such that a smooth contact is achieved. Close to the boundary the particular choices of the two parameters do not influence the observable such as density. However, as we look at the density away from the boundary in this effectively semi-infinite system we observe that certain pairs of choices perform 'better' compared to others. Saying they perform better implies that they lead to a smoother density from which a

power law is more easily inferred. In the following section we present our results and all the relevant parameters that we used to obtain them.

7.2 The results and discussion

7.2.1 Density Functional Theory

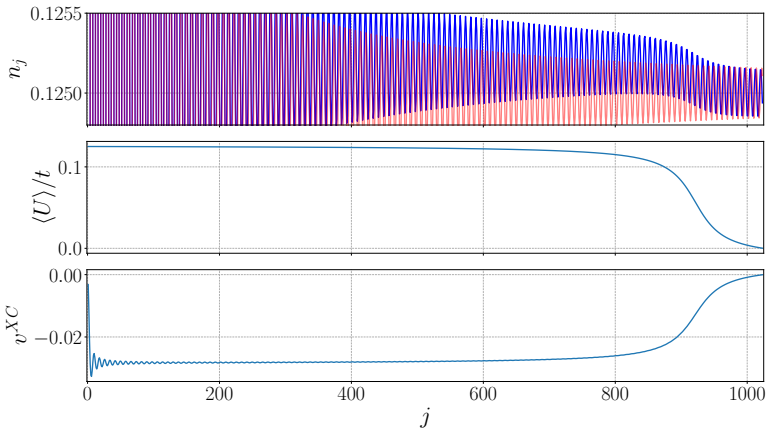

Figure 7.1: Illustration of the smooth connection of the finite interaction wire to an non-interacting reservoir. We set system size to $L = 1024$, the interaction to $U/t = 0.125$, and filling $\nu = 1/8$, and parameters $w = 32$ and $j_s = 9L/10$. The interaction is treated with the DFT method with the LDA approximation. Top panel: the DFT density (blue) and non-interacting density (red); middle panel: scaling of interaction $\langle U \rangle$; bottom panel: exchange-correlation potential v^{XC}.

In Fig. 7.1 we illustrate how a smooth connection to the lead is achieved. In particular, we plot the density n_j (top panel), the scaling of local interaction $\langle U \rangle = (U_{j+1} + U_{j-1})/2$ (middle) and the exchange-correlation v^{XC}(bottom). We used DFT together with

the LDA approximation to the exchange-correlation potential to treat the interaction as already described in Sect. 5.1. The SCF cycle converged as quickly as for the finite system case and similarly no CDW instabilities are present for the repulsive interaction in the $0 < U/t < 2$ regime. The DFT density (top panel in blue) does not exhibit any abrupt changes but rather a smooth decay of the density oscillation as j approaches L. We additionally plot the non-interacting density in the TD limit (top panel in red) from Eq. 5.11.

Obtaining a perfectly smooth density in a LDA DFT calculation additionally requires the knowledge of the LDA exchange-correlation potential for a continuous number of interaction strengths from U to 0; see middle panel of Fig. 7.1. This implies that one needs to solve the BA equations from Chap. 3 at each lattice site which can not be efficiently performed. In practice, we precompute the LDA exchange-correlation potential for a fixed number of interactions U_i along the decaying function before we run the calculation to obtain the density. We further linearly interpolate between the obtained values if U happens to lie in between the precomputed U_i and U_{i+1}. The parameterization from Ref. [AC07] on the other hand offers an efficient way to generate the LDA exchange-correlation potential. However, as we show in Fig. 5.2 this parameterization is not suitable away from half-filling and therefore we do not use it in our work. At half-filling the LDA BA exchange-correlation potential approaches zero in the gapless LL regime. This leads to a minimal correction to the density at this particular filling. Therefore, we exempt the half-filling case from our further analysis.

Looking at the top plot of the density (blue line) of Fig. 7.1 one might deduce that the average density in the interacting region is not at the correct filling ν but rather higher. This would imply that any further analysis on this data set is going to be for this higher filling opposed to the one we started with. However, this is not the case. In Fig. 7.2 we plot the same density from Fig. 7.1 but now compared to the density from larger systems. We observe a systematic trend of the average density moving closer and closer to the correct average filling implying that our thermodynamic analysis is consistently performed and for the correct filling. The density in the interacting region being higher is another finite size effect a

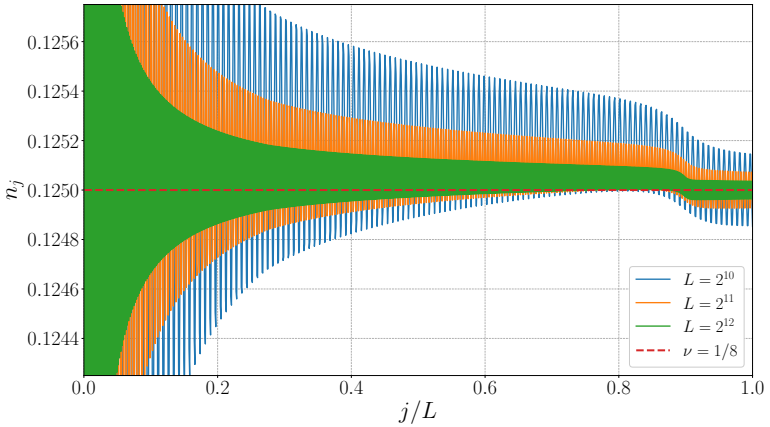

Figure 7.2: Friedel oscillations for different system sizes. Same parameters used as in Fig. 7.1.

direct consequence of the prescribed condition of choosing r such that the average in the total system (interacting together with the non-interacting in finite system of size L) is a close a possible to ν.

To show that the method to access the TD limit from Sect. 7.1 is indeed useful we compute the density of a system with a lead connected (OPEN[1]) on the right side and a boundary on the left as in the sketch in Fig. 2.3. We compare the density decay of this OPEN system with a finite (CLOSED) system with two boundaries. In Fig. 7.3 the logarithmic derivative of the upper dominant envelopes[2] for OPEN and CLOSED systems is presented. In the case of the OPEN system we observe that the logarithmic derivative exhibits a closer to a constant value behavior over a larger distance compared to the CLOSED system. This implies a more 'stable' power law[3]and enables a more reliable measurement of the the power law exponent.

[1]This does not refer to the open boundary conditions (OBC) but rather that the finite system has been opened up and allowed to interface with an environment (lead).

[2]The upper dominant envelope is formed at sites $j = 5, 13, 21, ...$ and the lower dominant envelope at $j = 1, 9, 17, ...$ at $v = 1/8$ filling.

[3]If there is a power law present at all.

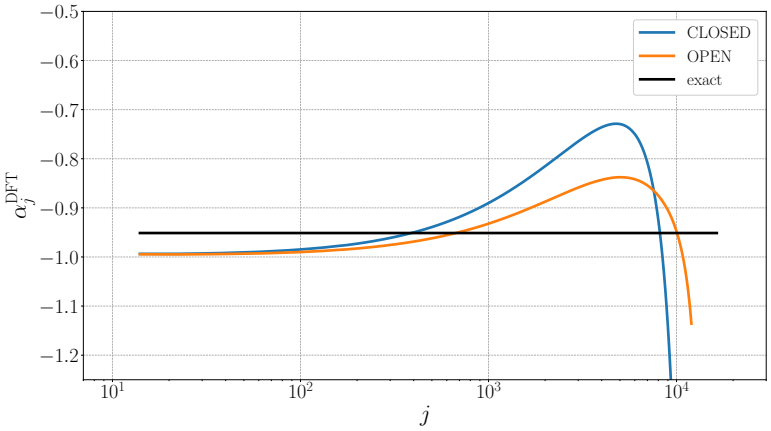

Figure 7.3: Logarithmic derivative (from Eq. 5.17) for a finite interacting system (CLOSED) and finite interacting connected to an non-interacting lead (OPEN). Parameters used: $L = 2^{14}$, $\nu = 1/8$, $j_s = 19L/20$, $U/t = 0.25$ and $w = 64$. Further discussion in text.

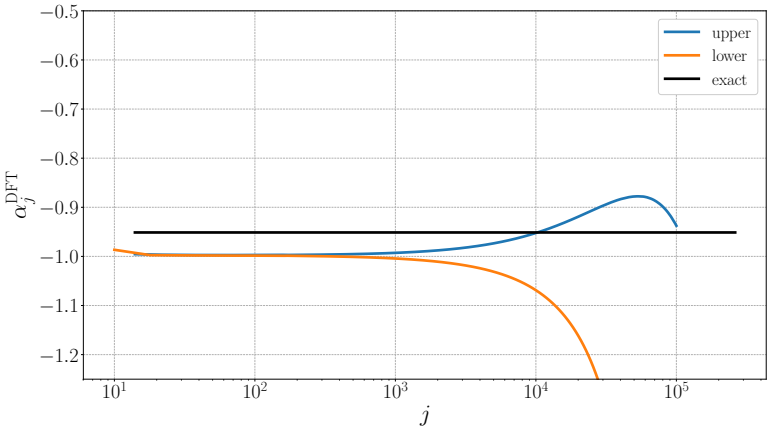

Figure 7.4: Logarithmic derivative of the upper and lower envelope of the LDA DFT density. The upper envelope provides a more 'stable' power law . Same parameters as for Fig. 7.3 but for $L = 2^{16}$ and $U/t = 0.1$. Further discussion in text.

In the true TD limit there is no difference between looking at the lower and upper dominant envelope of the density. In practice, as illustrated in Fig. 7.4, the density actually deviates earlier from a constant value in the case of the lower envelope. This can be understood by looking back at Fig. 7.1 and identifying that the smoothening procedure will always induce small differences between the upper and lower envelopes. Irrespective of how 'perfect' the contact is, approaching the non-interacting density from above (blue line approaching the red) will always produce a different way of connecting the interacting and non-interacting region[4] for the upper and lower envelopes.

Any finite size approach[5] fails to capture the correct asymptotics of the density. In Fig. 7.5, we illustrate how our approach produces a consistent and reliable determination of the underlying power law in case of LDA DFT. As we increase the system size L in the OPEN case we achieve a consistent straight line in the logarithmic derivative over several orders in the site index j signaling a power law decay. In fact for $L = 2^{20}$ the underlying power law is 'stable' over almost four orders in j! In Fig. 7.3, 7.4 and 7.5 we compare the LDA DFT results to the exact asymptotic exponent computed via Eq. 3.42. There exists an obvious disagreement between the exact exponent and the one obtained with DFT. The LDA DFT calculation for finite repulsive interaction, $U > 0$, is consistent with an exponent that is close to the noninteracting value of -1. To show this, in Fig. 7.6, we compute the exponent of the density within LDA DFT for different interaction strengths and fillings. We observe that LDA DFT does not give a satisfying description of the Tomonaga-Luttinger liquid power-law scaling of the decay of the density away from an open boundary towards the bulk value ν.

In the past the typical LDAs have found success in inhomogeneous systems where interaction is not too strong; see Ref. [Ull12]. However, in 1D the correlation effects due to the strong interaction play a more prominent role compared to higher dimensions where quasi-particle Fermi liquid paradigm is all-encompassing. Therefore, the correct description of strongly correlated Luttinger liquids in 1D via DFT

[4] See the blue density in the region in between $j = 800$ and $j = 1000$ and how different the upper and lower envelopes actually have to be.

[5] For example, see Fig. 5.5 and discussion regarding the figure in text.

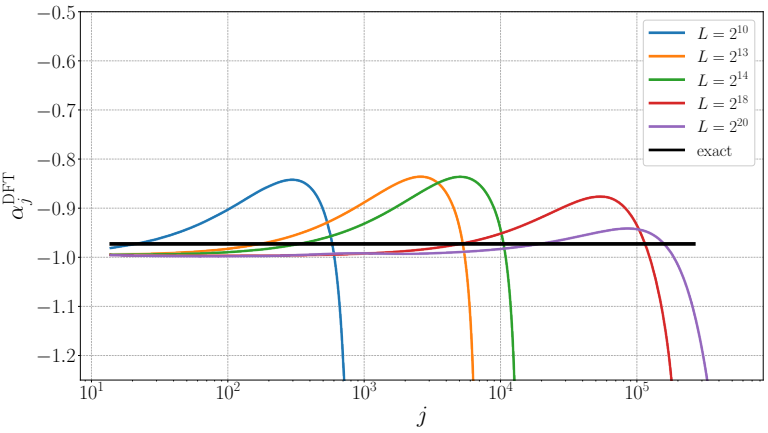

Figure 7.5: Logarithmic derivative for different systems sizes L (see legend). Same parameters used as in Fig. 7.3. Further discussion in text.

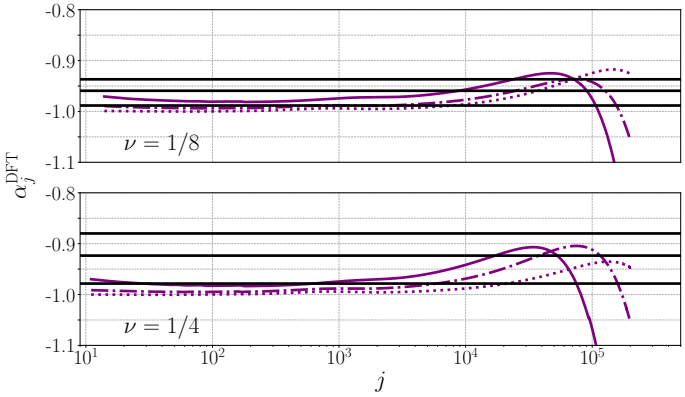

Figure 7.6: The exponents measured using logarithmic derivative for system size $L = 2^{20}$. The parameters are $\nu = 1/8$ (upper panel) and $\nu = 1/4$ (lower panel), $U/t = 0.1$ (dotted), $U/t = 0.4$ (dashed-dotted), and $U/t = 0.7$ (solid). Solid lines from bottom to top ($U/t = 0.1, 0.4, 0.7$) depick the exact exponents.

remains an open question.

7.2.2 Hartree-Fock approximation

We now discuss the results of 'full inversion' HF calculations, and following the discussion at the end of Sect. 6.1.4 we try to determine whether or not this particular approximate approach leads to beyond logarithmic corrections[6] in the density which are specified in Eq. 6.43. To that end, we analyse the results from this method using both the logarithmic derivative α_j from Eq. 5.17 and the semi-logarithmic derivative which we define as

$$\beta_j = 2\pi \frac{(j+\nu^{-1})\tilde{n}(j+\nu^{-1}) - (j-\nu^{-1})\tilde{n}(j-\nu^{-1})}{\ln(j+\nu^{-1}) - \ln(j-\nu^{-1})}. \tag{7.3}$$

If the density data is consistent with the logarithmic correction from Eq. 6.43, β_j should display a plateau at the value $\frac{U}{2\pi t \sin(k_\mathrm{F})}[1-\cos(2k_\mathrm{F})]$. In Fig. 7.7 we compare α_j^HF and β_j^HF for a given parameter set to judge which of the two is more plateau-like. For small U/t the 'full inversion' HF data are consistent with both the power-law and the logarithmic behavior. For larger U/t, β_j^HF is more plateau-like as compared to α_j^HF. Furthermore, the value of the plateau of β_j^HF is close to $\frac{U}{2\pi t \sin(k_\mathrm{F})}[1-\cos(2k_\mathrm{F})]$ which is shown as the solid horizontal line. However, due to the effect of the right boundary, at larger j a deviation from the plateau is found already for $j \ll L$.

For $\nu = 1/4$ and $U/t = 0.7$ a deviation between the plateau value of the data and the expectation (solid horizontal line) from first order perturbation theory is found. This is due to higher order corrections (in U/t) appearing in the 'full inversion' HF approximation. For larger interactions those become sizable. One such correction originates from the changed band width $t \to \bar{t}$; see Eq. 6.18. In fact the horizontal dashed line which reads

$$\frac{U}{2\pi \bar{t} \sin(k_\mathrm{F})}[1-\cos(2k_\mathrm{F})] \tag{7.4}$$

[6] In particular, to a power law.

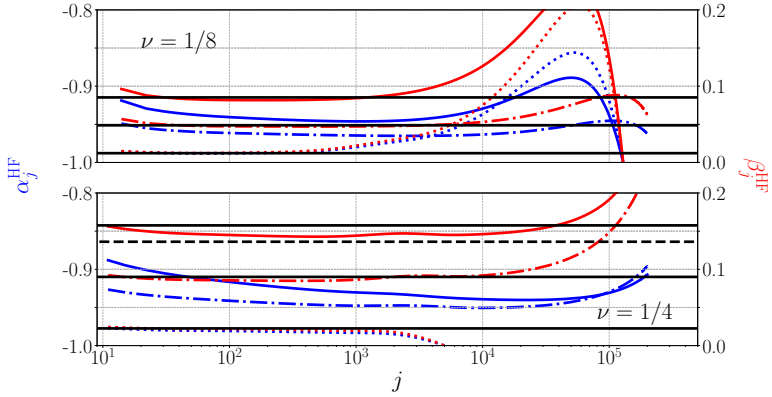

Figure 7.7: The exponent α_j^{HF} Eq. 5.17 (blue) and prefactor of $\ln(j)$ Eq. 7.3 (red) of the decay of the density oscillations within the 'full inversion' HF approximation for a system with two open boundaries. The parameters are $\nu = 1/8$ (upper panel) and $\nu = 1/4$ (lower panel), $U/t = 0.1$ (dotted), $U/t = 0.4$ (dashed-dotted), and $U/t = 0.7$ (solid). The horizontal solid lines indicate the prefactor of the $\ln j$ term from first order perturbation theory for the Green function from Eq. 6.43. The horizontal dashed line shows this value with t replaced by $\bar{t}$ (only shown for $\nu = 1/4$ and $U/t = 0.7$).

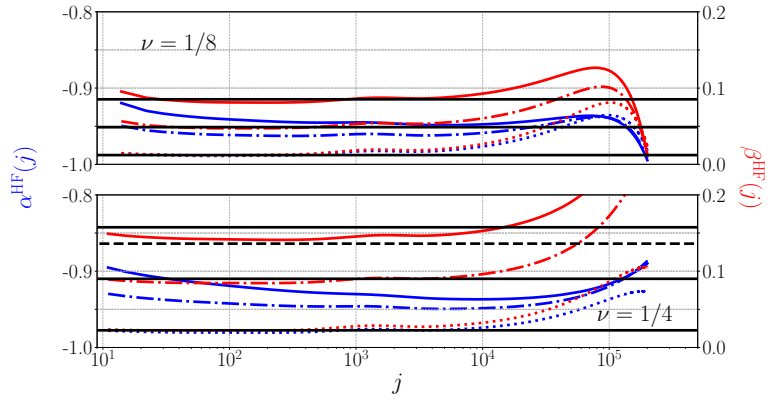

Figure 7.8: Parameters same as in Fig. 7.7, but for a system with one open boundary, adiabatically connected to a semi-infinite non-interacting reservoir.

fits the data better. The dashed line and this renormalization is plotted only for quarter filling and interaction strength $U = 0.7$.

In Fig. 7.8 we suppress the effect of the boundary by attaching a non-interacting reseroir. We use the same parameters as in Fig. 7.7. The results of Fig. 7.8 support the observations made already in the previous plot where both boundaries were present and indicate that 'full inversion' HF does not lead to a resummation of logarithmic terms (starting with the first order linear correction) to a power law.

7.2.3 Hartree-Fock approximation at half-filling

Putting together the non-interacting density results in Eqs. 6.59 and 6.60 with results from the first order perturbation theory in the Green's function (at Hartree-Fock level), Eqs. 6.71 and 6.74, respectively, we obtain

$$n_j^0 + n_j^{1\mathrm{PT}} \underset{V\to 0}{=} \frac{1}{2} + \frac{V}{\pi}\frac{\cos(\pi j)}{j}\Big(1 - \frac{U}{\pi t}\ln j\Big), \tag{7.5}$$

$$n_j^0 + n_j^{1\mathrm{PT}} \underset{V\to \infty}{=} \frac{1}{2} + \frac{1}{V\pi}\frac{\cos(\pi j)}{j}\Big(1 + \frac{U}{\pi t}\ln j\Big). \tag{7.6}$$

In the weak impurity case ($V \to 0$), for any repulsive interaction $U > 0$, in similar manner as in Sect. 6.1.4, we identify a prefactor to the logarithm with a negative sign, while in the strong impurity case ($V \to \infty$) a prefactor with a positive sign. Therefore, as already mentioned in Sect. 6.2, a qualitative change to the density occurs at some finite impurity strength V.

In Fig. 7.9 we observe this qualitative change in the numerical 'full inversion' HF approximation density data as well. Implying that with the introduction of a single impurity at the first site, we are able to recover the logarithm[7] and induce a transition from a non-generic to the generic regime (one which is predicted by the field theory method). However, once we are in the generic regime a choice of an extremely strong impurity effectively leads back to the impurity free semi-infinite system with the boundary now at $j = 1$ instead at $j = 0$. Our analysis, therefore, although only perturbative, should be of relevance to any methodology that treats this particular model and the observable that is the density.

[7] To be contrasted with Eq. 6.48.

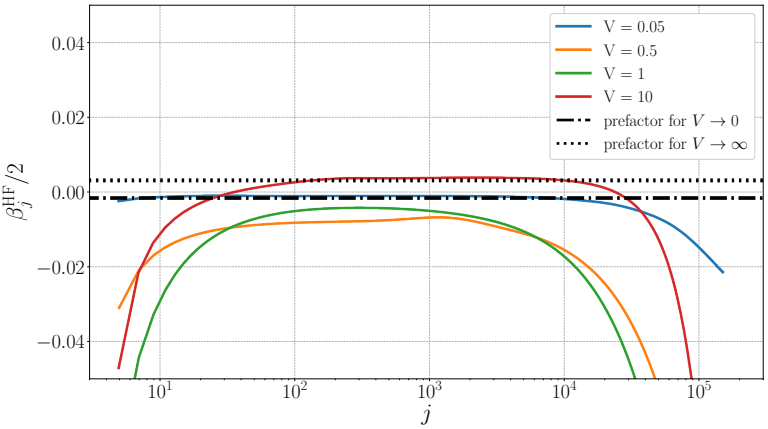

Figure 7.9: The prefactor of $\ln(j)$ Eq. 7.3 of the decay of the density oscillations within the 'full inversion' HF approximation for a system with one open boundary and adibatically connected to a semi-infinite noninteracting reservoir. We treat a system where the interaction is set to $U/t = 0.1$ and the $j = 1$ site is subjected to a varying single-particle impurity potential V. As the impurity strength increases from $V = 0$ a transition from a negative to a positive β_j^{HF} occurs. To perform the calculation we used: $L = 5 \cdot 2^{17}$, $\nu = 1/2$, $j_s = 9L/10$ and $w = 64$. The prefactor is compared to analytical prediction in Eq. 7.5 (black dashed-dotted) and Eq. 7.6 (black dashed).

8 Conclusions and outlook

In this thesis, we focused on the ground state properties of correlated one-dimensional fermionic systems. In particular, using various approaches and approximation schemes, we examined the Friedel oscillations of the charge density in the presence of interaction and open boundary conditions.

The method of main interest to us was Density Functional Theory (DFT). First, in order to study the density oscillations decay away from the boundaries in a finite system, we employed the Local Density Approximation (LDA); see Sect. 5. For the model with short-range interaction the LDA was built from the Bethe ansatz (BA) solution of the homogeneous reference system in the thermodynamic limit; see Ref. 5.1. We compared the LDA results to the exact density obtained numerically from Density Matrix Renormalization Group (DMRG) calculations in order to estimate how successful this approximation truly is in computing the density. In Ref. [AC07], a similar analysis has been performed but for smaller systems and not in comparison to other common approximation schemes such as the Hartree-Fock (HF) approximation. While the self-consistent HF approximation is subject to charge-density wave instabilities, LDA DFT showed no such tendencies. Moreover, the comparative study gave insight into the severe and unequivocal influence of finite size effects on the density. Although the importance of finite-size effects in quantum many-body systems is established and well-documented in the literature, we reiterate on this issue in the effort to motivate

the necessity for an efficient method in the intermediate to large length scales where such effects are negligible in comparison to the underlying low energy physics. This lead to the formulation of the ordinary differential equation (ODE) DFT method, and in particular to the computation of the density using the Matsubara Green's function formalism without any reference to the Kohn-Sham (KS) eigenstates; see Sect. 4.3 and 2.

The Green's function formalism with its variety of flavors is quite common in quantum many-body theory. However, to our knowledge, the particular implementation of Matsubara Green's functions with DFT, and resulting in the formulation of the ODE DFT method, has not been performed elsewhere. Moreover, solving a set of first order differential equations to obtain the KS ground state densitiy, instead of direct diagonalization, can be considered unusual. The most likely reason that this kind of formalism has not been discussed in the DFT community before, is that in DFT one solves a system of non-interacting particles subject to an effective potential and typical diagonalization schemes are very efficient[1]. In material related calculations where DFT is usually applied, only few eigenstates per unit cell are relevant and those can be efficiently computed by diagonalization[2]. In transport calculations only a small and finite junction system is simulated and the effects of the environment are effectively projected out. However, to answer questions regarding the low energy Luttinger liquid (LL) physics, the treatment of large systems and also a substantial number of particles is necessary and its no longer sufficient to rely on the efficiency of the diagonalization of a non-interacting problem.

The efficiency of the ODE DFT approach comes at the price of precision, as was already pointed out in Chap. 2, which can in principle be improved if more effort is put into solving the differential equations. This approach is flexible and general. General, in the sense that it can be readily applied to a variety of problems

[1] Of course, the improvement of the efficiency of DFT calculations is a field of study on its own, but we would like to stress here that compared to other many-body methods DFT is not computationally demanding. It reduces to the diagonalization of the non-interacting KS Hamiltonian and computation of a not extremely large number of eigenstates.

[2] In this type of calculations periodic boundary conditions are assumed to simulate the bulk.

that can be mapped to tri- or penta-diagonal Hamiltonian matrix operators, even beyond simple model Hamiltonians. Therefore, it would be interesting to apply this method to transport and various other computationally demanding ground state calculations. Furthermore, extending the Matsubara formalism to ground state energy calculations presents an interesting project from the DFT perspective.

Part of this thesis was dedicated to a perturbative study of Friedel oscillations; see Chap. 6. In systems with open boundary conditions, perturbation theory has already proven to be quite successful; see Ref. [SMM+00]. Our research in this context is, therefore, a continuation of this line of efforts but for the density. The perturbation theory for the density has shown to be more involved compared to previous calculations on the local density of states. In particular, the integrals appearing in the perturbative correction in U required a special set of transformations in order to be reliably evaluated; see Appendix A. Furthermore, the asymptotic analysis required innovative ways of treating singular behavior of the integrands using contour integration and the steepest descent method on two-dimensional Fourier type integrals; see Appendix B. This approach can be readily generalized and applied to higher-dimensional Fourier integrals and higher order singularities at the vertex of the support. Nevertheless, similar mechanisms and singularity structure were ultimately responsible for the logarithmic corrections in the LDOS and the density; see Sect. 6.2. Also, we find that the 'full inversion' Hartree-Fock approximation does not not lead to a power-law decay of the density. This is an interesting result, given that the LDOS at the same approximation level is characterized by a power-law.

Moreover, using perturbation theory we were able to treat the half-filling case of the spinless fermion model with nearest-neighbor hopping. We illustrated the special nature of the particle-hole symmetry in this model and discussed a simple mechanism that lead to the breaking of this symmetry. This kind of analysis is of relevance to any methodology that attempts to treat this particular microscopic model.

In Chap. 7 we used the Matsubara Green's function approach to effectively treat semi-infinite systems where the finite size effects are significantly reduced, enabling a consistent inference of the

asymptotics. We were able to discern a power-law behavior in the density computed using the LDA DFT. The LDA lead to the correct tendency of the density decay exponent to be larger than -1 for repulsive interactions. However, the measured exponent was significantly different from the exact one. This implies that LDA, in fact, is unable to capture the correct Luttinger liquid behavior of the density in the microscopic model of interacting spinless fermions. Moreover, in small interaction strength regimes the HF approximation was show to perform better than LDA DFT.

LDA DFT does not capture LL physics of the density decay, but some other approximation to the exchange-correlation potential might. Our work on the ODE DFT method and the particular way we reduce the finite size effects by coupling to an semi-infinite environment, however, enables a consistent analysis of the LL fixed point in case such an approximation is found.

The natural extensions beyond LDA are categorized according to the Jacob's ladder taxonomy. According to this ladder representation of functional approximations, the first step towards improving the LDA is to include information about the derivative of the density with respect to the space coordinate into the exchange-correlation potential. This information can, in principle, provide an improvement in treating systems where a boundary breaks the translational invariance and leads to Friedel oscillations. However, the Bethe ansatz approach in the thermodynamic limit treats exclusively homogeneous systems and is unable to provide us with such details. It is, nevertheless, encouraging that in one dimension a large number of other exact or low energy results are available in strongly correlated regimes that can be exploited in the effort of constructing better approximations that indeed capture LL physics.

Appendix

A Numerical treatment of multidimensional Fourier type integrals with a singularity at a vertex

The piece-wise integral in Eq. 6.30 entails two particular challenges in its numerical evaluation: first the integrand is highly oscillatory and second the integral is an improper integral of the second kind (i.e. the integrand is singular at $k = k' = k_\mathrm{F}$). The first challenge can be overcome by using specialized numerical routines for Fourier type integrals that take the oscillatory behavior into account. In this appendix we address the second challenge. However, we note that the integrand is not singular for certain j as mentioned in the text, namely the ones for which the numerator vanishes, $\sin(k_\mathrm{F} j) = 0$ (e.g. if $k_\mathrm{F} = \frac{\pi}{4}$ for $j = 4, 8, 12, ...$). In those cases we can reliably evaluate the integral but in all others we are faced with the divergence.

In this Appendix, we remove the singularity with a suitable variable transformation introduced in Ref. [Duf82]. This transformation allows for the treatment of multidimensional integrals over square based pyramids or cubes where the singularity lies at a vertex. In our particular application we treat a double integral over

a triangular domain with a singularity at one of the vertices. The transformation will enable the evaluation of the integral for any site index j with high numerical precision. However, before we use the transformation we have to place the singularity at the origin and at one of the vertices of the hypotenuse of the triangle as in Fig. A.1 in between (C) and (D). This requires us to first perform a set of transformations on our original integral.

The integral is initially divided into four separate ones over triangular domains (Fig. A.1) as

$$I_1 = \int_0^{k_\mathrm{F}} \mathrm{d}x \int_{k_\mathrm{F}}^{2k_\mathrm{F}-x} \frac{\sin(xj)\sin(yj)}{\cos(y)-\cos(x)} f_1(x,y)\mathrm{d}y, \tag{A.1}$$

$$I_2 = \int_0^{k_\mathrm{F}} \mathrm{d}x \int_{2k_\mathrm{F}-x}^{k_\mathrm{F}} \frac{\sin(xj)\sin(yj)}{\cos(y)-\cos(x)} f_2(x,y)\mathrm{d}y, \tag{A.2}$$

$$I_3 = \int_0^{k_\mathrm{F}} \mathrm{d}x \int_{2k_\mathrm{F}}^{2k_\mathrm{F}+x} \frac{\sin(xj)\sin(yj)}{\cos(y)-\cos(x)} f_3(x,y)\mathrm{d}y, \tag{A.3}$$

$$I_4 = 0. \tag{A.4}$$

Here, f_1, f_2 and f_3 are dummy functions that depend on both x and y (k and k' respectively). The only requirement on these functions for the following procedure to be applicable is that they are analytic. In our case, they encode the Hartree-Fock self-energy contributions and are indeed analytic. For general fillings I_1 and I_2 have a pole at $(k_\mathrm{F}, k_\mathrm{F})$ in the integrand. This is not the case for I_3 and we can immediately evaluate it. Therefore, in the following we focus on I_1 and I_2.

The set of transformations together with the corresponding Jacobians that take us from integrating over triangular support with a singularity at one of the vertices to a square support $[0,1]\times[0,1]$ without the singularity (see Fig. A.1), is given by

- $A_1 : (x,y) \mapsto (k_\mathrm{F} - xk_\mathrm{F} - yk_\mathrm{F}, k_\mathrm{F} + xk_\mathrm{F})$ with $|J| = k_\mathrm{F}^2$,
- $A_2 : (x,y) \mapsto (k_\mathrm{F} - yk_\mathrm{F}, k_\mathrm{F} + xk_\mathrm{F} + yk_\mathrm{F})$ with $|J| = k_\mathrm{F}^2$,

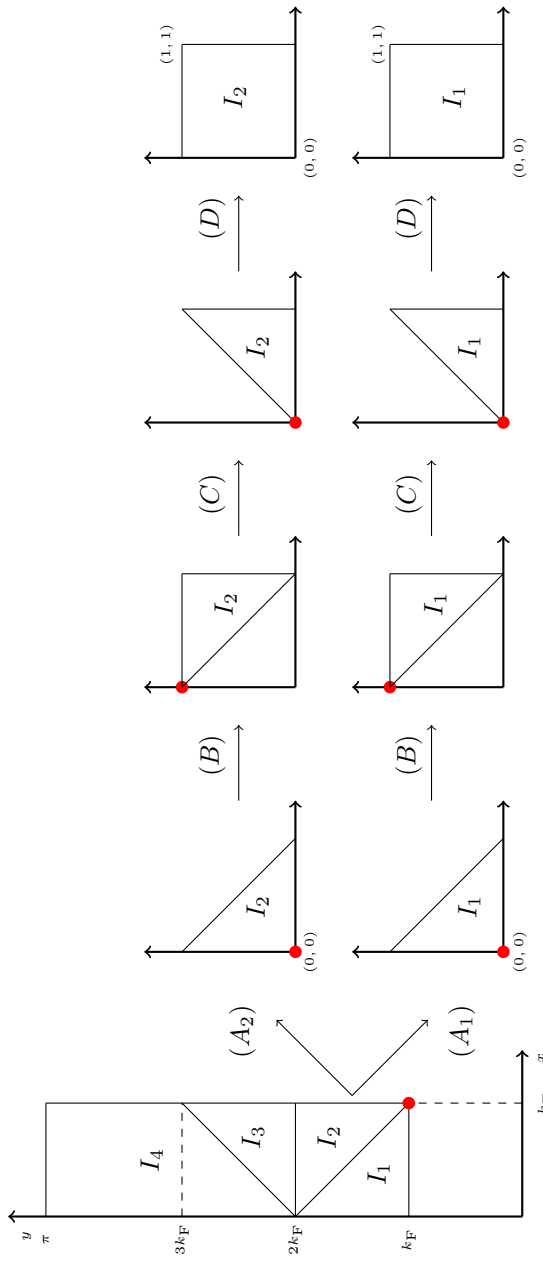

Figure A.1: Sketch of the integration domain of the integral in Eq. 6.30 and subsequent division in Eq. A.1-A.4, followed by the sequence of transformations $\{A_{1,2},B,C,D\}$. The red dot represents the singularity. Transformations (A) to the (C) are there to make the integral Duffy transformation amenable.

- $B : (x, y) \mapsto (x, x + y)$ with $|J| = 1$,

- C : exchange the order of integration (instead of integrating first over y integrate over x). This can be done via a Heaviside θ function as

$$\int_0^1 \mathrm{d}x \int_{f(x)}^1 g(x,y)\mathrm{d}y = \int_0^1 \mathrm{d}x \int_0^1 \theta\Big(y - f(x)\Big) g(x,y)\mathrm{d}y$$
$$= \int_0^1 \mathrm{d}y \int_0^1 \theta\Big(f(x) - y\Big) g(x,y)\mathrm{d}x = \int_0^1 \mathrm{d}y \int_0^y g(x,y)\mathrm{d}x,$$

  and then use $(x, y) \mapsto (y, x)$ with $|J| = 1$,

- D : Duffy transformation $(x, y) \mapsto (x, xy)$ with $|J| = x$.

The affine transformations $A_{1,2}$,B and C bring the integral to a Duffy transformable form, and the last transformation D is the one known as Duffy transform. After this set of transformations $\{A_{1,2}, B, C, D\}$ the integrals in Eq. A.1 and A.2 read

$$I_1 = k_\mathrm{F}^2 \int_0^1 \mathrm{d}x \int_0^1 \frac{x \sin(jt_1) \sin(jt_2)}{\cos(t_2) - \cos(t_1)} f_1(t_1, t_2)\mathrm{d}y, \tag{A.5}$$

$$I_2 = k_\mathrm{F}^2 \int_0^1 \mathrm{d}x \int_0^1 \frac{x \sin(jt_3) \sin(jt_4)}{\cos(t_4) - \cos(t_3)} f_2(t_3, t_4)\mathrm{d}y, \tag{A.6}$$

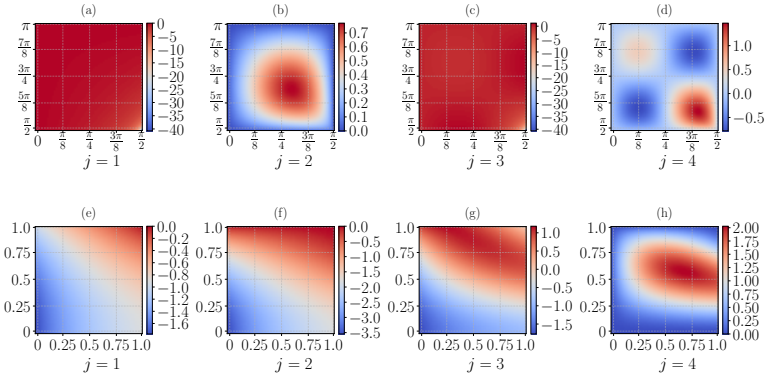

Figure A.2: Particular example of how the singularities get lifted at half-filling ($k_\mathrm{F} = \pi/2$) after the application of the transformations for different sites j. Top row: integrand of $I_1 + I_2$ as in Eq. A.1 and A.2. Bottom row: after transformations $I_1 + I_2$ as in Eq. A.5 and A.6. The divergent cases are (a) and (c) which transform into (e) and (g) which are analytic. We plotted the integrand as a $L \times L$ grid with $L = 64$. For simplicity we used $f_{1,2}(x, y) = 1$ for this plot.

where we denoted $t_1 = k_\mathrm{F}(1-x)$, $t_2 = k_\mathrm{F}(1+xy)$, $t_3 = k_\mathrm{F}(1-xy)$ and $t_4 = k_\mathrm{F}(1+x)$. Notice the emergence of a factor x in the numerator after the transformations. This factor is the one that allows for the regularization of the divergent integrands. The integrand is now analytic in the square region for all sites j. In Fig. A.2 we plot the integrand and how it changes under the transformations for the case of half-filling. We observe that for $j = 1$ and $j = 3$ the singular peak in the integrand is smoothened out on the full square domain.

B Asymptotic analysis of multidimensional Fourier type integrals with a singularity at a vertex

In this Appendix, we perform the asymptotic analysis, $j \to \infty$, for the Fourier type integrals in Sect. 6 . We separately discuss integrals that are given over rectangular and triangular domains. Our focus is going to be on the two-dimensional integrals but similar steps, as the ones presented here, can be applied to higher dimensional variants.

B.1 Integrals over a rectangular domain

An example from this category of integrals is

$$I = \int_0^a \mathrm{d}x \int_a^b \mathrm{d}y \frac{\sin(xj)\sin(yj)}{\cos(y) - \cos(x)} f(x,y), \tag{B.1}$$

where $f(x,y)$ is assumed to be analytic. An additional constraint on $f(x,y)$ is that we assume it is a symmetric function under the

exchange of arguments[1]. The bounds should satisfy $0 < a < b$ but the approach could readily be extended to more general situations. The integrand is singular at $x = y = a$, hence, the usual integration by parts approach fails to extract the asymptotics. Therefore, we rewrite the integral as

$$I = \int_0^a \mathrm{d}x \int_a^b \mathrm{d}y \Big(e^{ixj} - e^{-ixj}\Big)\Big(e^{iyj} - e^{-iyj}\Big) g(x,y), \tag{B.2}$$

with $g(x,y) = -\frac{1}{4}\frac{f(x,y)}{\cos(y)-\cos(x)}$. In this form the integral represents an ordinary Fourier integral and its asymptotics can be accessed by the steepest descent method described in Ref. [BO99]. We first focus on the integral over y, in particular

$$\int_a^b \mathrm{d}y \Big(e^{iyj} - e^{-iyj}\Big) g(x,y). \tag{B.3}$$

To evaluate the integral over $g(x,y)e^{iyj}$ we deform the integration contour $\mathcal{C}$, which runs from a to b along the real y axis, to one that is made out of three line segments: $\mathcal{C}_1$ which runs parallel to the imaginary y axis from a to $a+iy'$; $\mathcal{C}_2$ which runs parallel to the real y axis from $a+iy'$ to $b+iy'$; and $\mathcal{C}_3$ which runs from $b+iy'$ to b along a straight line parallel to the imaginary y axis as depicted in Fig. B.1 (a). Next we let $y' \to \infty$ such that the integral along $\mathcal{C}_2$ vanishes. Exercising a similar contour decomposition for the second term we obtain two relevant contours $\mathcal{C}_4$ and $\mathcal{C}_6$ while the integral along $\mathcal{C}_5$ vanishes for the same reason $\mathcal{C}_2$ did, see Fig. B.1 (a).

After the contour deformation of the integral over y the total integral becomes

$$I = \int_0^\infty \mathrm{d}(iy') e^{-jy'} \int_0^a \mathrm{d}x h(x) \Big(e^{ixj} - e^{-ixj}\Big), \tag{B.4}$$

with $h(x) = e^{ija} g(x, a+iy') - e^{ijb} g(x, b+iy') + e^{-ija} g(x, a-iy') - e^{-ijb} g(x, b-iy')$.

[1] In particular, $f(x,y) = f(y,x)$. Later, in the text we show why and where this property is important.

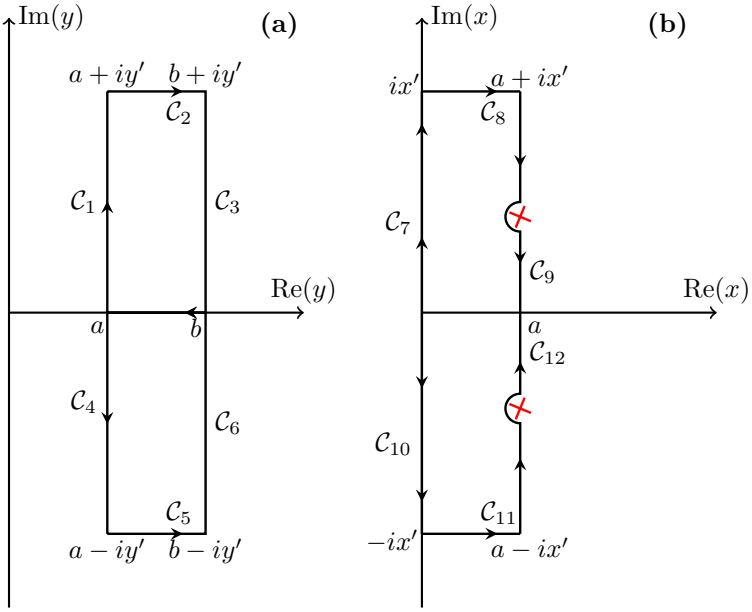

Figure B.1: (a) inner integral contours, (b) outer integral contours. Poles are at the red crosses and at intersections between inner and outer contours.

We apply the same steps to the integral over x and deform the contour into three line segments for each of the two terms. This time, however, two poles are present on the contours, which arise from the singularity at $x = y = a$. They have, due to our contour deformation, moved away from the real axis as depicted in the right of Fig. B.1 (b). The integral after the second contour deformation[2]

[2]By noticing that $h(ix') + h(-ix') = h(ix') + h^*(ix') = 2\mathrm{Re}[h(ix')]$.

reads as

$$I = \int_0^\infty \mathrm{d}(iy')e^{-y'j}\Big\{i\pi\mathrm{Res}\Big[h(a+ix')e^{ij(a+ix')}, x' \to y'\Big] + i\pi\mathrm{Res}\Big[h(a-ix')e^{-ij(a-ix')}, x' \to y'\Big] + \int_0^\infty \mathrm{d}(ix')e^{-x'j}\Big(2\mathrm{Re}[h(ix')] - e^{ija}h(a+ix') - e^{-ija}h(a-ix')\Big)\Big\}, \tag{B.5}$$

where $\mathrm{Res}(f, c)$ denotes the residue of a function f at c. The poles have only half of the usual residue contribution because they lie on the contours. The terms

$$\int_0^\infty \mathrm{d}(iy')e^{-jy'} \int_0^\infty \mathrm{d}(ix')e^{-jx'} 2\mathrm{Re}[h(ix)]$$
$$= 2\mathrm{Re}\Bigg[-\frac{1}{4}\int_0^\infty \mathrm{d}(iy')e^{-jy'} \int_0^\infty \mathrm{d}(ix')e^{-jx'}$$
$$\Bigg(e^{ija}\frac{f(ix', a+iy')}{\cos(a+iy') - \cos(ix')} - e^{ijb}\frac{f(ix', b+iy')}{\cos(b+iy') - \cos(ix')}$$
$$+ e^{-ija}\frac{f(ix', a-iy')}{\cos(a-iy') - \cos(ix')} - e^{-ijb}\frac{f(ix', b-iy')}{\cos(b-iy') - \cos(ix')}\Bigg)\Bigg], \tag{B.6}$$

exhibit a asymptotic decay of order j^{-2}. The asymptotic analysis by integration by parts[3] tells us that each integral out of the double integral gives a leading order of j^{-1} and, therefore, j^{-2} for the total integrals. The two remaining terms in the third line of Eq. B.5, when explicitly written out, read

[3] Works well here because f is analytic and no poles are present in the rest of the integrand.

$$\frac{1}{4}\int_0^\infty \mathrm{d}(iy')e^{-jy'}\int_0^\infty \mathrm{d}(ix')e^{-jx'}\Bigg\{$$

$$\frac{e^{2ija}f(a+ix',a+iy')}{\cos(a+iy')-\cos(a+ix')}+\frac{e^{-2ija}f(a-ix',a-iy')}{\cos(a-iy')-\cos(a-ix')}, \tag{B.7}$$

$$+\frac{f(a+ix',a-iy')}{\cos(a-iy')-\cos(a+ix')}+\frac{f(a-ix',a+iy')}{\cos(a+iy')-\cos(a-ix')}, \tag{B.8}$$

$$+\frac{e^{ij(a+b)}f(a+ix',b+iy')}{\cos(b+iy')-\cos(a+ix')}+\frac{e^{-ij(a+b)}f(a-ix',b-iy')}{\cos(b-iy')-\cos(a-ix')}, \tag{B.9}$$

$$+\frac{e^{ij(a-b)}f(a+ix',b-iy')}{\cos(b-iy')-\cos(a+ix')}+\frac{e^{ij(b-a)}f(a-ix',b+iy')}{\cos(b+iy')-\cos(a-ix')}\Bigg\}. \tag{B.10}$$

Both of the terms in Eq. B.7 are individually zero because the domain of integration is symmetric under reflection w.r.t. to the axis $x' = y'$[4]. The two terms in Eq. B.8 cancel each other, iff f is a symmetric function which can be seen from an exchange of arguments. The terms in Eqs. B.9 and B.10 give a subdominant contribution of j^{-2} as did the terms in Eq. B.6.
The dominant contribution of the integral comes from the residue terms. In particular, the residue in the upper half-plane reads

$$\begin{aligned}
&\mathrm{Res}\Big[h(a+ix')e^{ij(a+ix')},x'\to y'\Big]\\
&=-\frac{e^{ija}}{4}\mathrm{Res}\left[\frac{f(a+ix',a+iy')}{\cos(a+iy')-\cos(a+ix')}e^{ij(a+ix')},x'\to y'\right]\\
&=-\frac{e^{2ija}}{4\sin(a+iy')}f(a+iy',a+iy')e^{-jy'}.
\end{aligned}$$

[4]Denoting the double integral as S and performing a variable transformation $(x',y')\mapsto(y',x')$ (together with the symmetric property of f) lead to $S=-S$ which is satisfied iff $S=0$.

The remaining residue of the pole in the lower half-plane can be evaluated similarly. Having computed both of the residues we finally arrive at

$$I \approx \frac{\pi}{4} \int_0^\infty \mathrm{d}y' e^{-2jy'} \left(\frac{f(a+iy', a+iy')}{\sin(a+iy')} e^{2ija} + \frac{f(a-iy', a-iy')}{\sin(a-iy')} e^{-2ija} \right). \tag{B.11}$$

Expanding around $y' = 0$ ($j \to \infty$ limit) we obtain

$$I \approx \frac{\pi}{2} \frac{f(a,a)}{\sin(a)} \cos(2ja) \int_0^\infty \mathrm{d}y' e^{-2jy'}. \tag{B.12}$$

The remaining integral can be trivially evaluated, and we obtain

$$I \approx \frac{\pi}{4j} \frac{f(a,a)}{\sin(a)} \cos(2ja). \tag{B.13}$$

B.2 Integrals over a triangular domain

An example from this category is

$$I = \int_0^a \mathrm{d}x \int_a^{2a-x} \mathrm{d}y \frac{\sin(xj)\sin(yj)}{\cos(y) - \cos(x)} f(x,y), \tag{B.14}$$

where we assume that $f(x,y)$ is analytic and symmetric under the exchange of variables. We begin by rewriting the integral as

$$I = \int_0^a \mathrm{d}x \int_a^{2a-x} \mathrm{d}y \Big(e^{ixj} - e^{-ixj}\Big)\Big(e^{iyj} - e^{-iyj}\Big) g(x,y), \tag{B.15}$$

with $g(x,y) = -\frac{1}{4} \frac{f(x,y)}{\cos(y) - \cos(x)}$. Now we use the following transformation $(x,y) \mapsto (a-x, a+y)$ with $|J| = -1$ which brings the

pole from (a, a) to $(0, 0)$ which in turn simplifies the computation by fixing the singularity structure to a static[5] contour instead of a moving one. This yields

$$I = \int_0^a \mathrm{d}x \int_0^x \mathrm{d}y \Big(e^{ij(a-x)} - e^{-ij(a-x)}\Big)\Big(e^{ij(a+y)} - e^{-ij(a+y)}\Big) \times g(a-x, a+y). \tag{B.16}$$

Using similar contour extensions for the integral over y, with $I = I_1 + I_2$, as in the rectangular example we arrive at

$$I_1 = e^{ija} \int_0^a \mathrm{d}x \int_0^\infty \mathrm{d}(iy')e^{-jy'} \Big[\Big(e^{ij(a-x)} - e^{-ij(a-x)}\Big)g(a-x, a+iy') - \Big(e^{ija} - e^{-ij(a-2x)}\Big)g(a-x, a+x+iy')\Big], \tag{B.17}$$

$$I_2 = e^{-ija} \int_0^a \mathrm{d}x \int_0^\infty \mathrm{d}(iy')e^{-jy'} \Big[\Big(e^{ij(a-x)} - e^{-ij(a-x)}\Big) \times g(a-x, a-iy') - \Big(e^{ij(a-2x)} - e^{-ija}\Big)g(a-x, a+x-iy')\Big]. \tag{B.18}$$

[5] Independent of the a variable.

We note that I_2 is the complex conjugate of I_1 which implies $I = 2\mathrm{Re}\big[I_1\big]$. Writing out I_1 explicitly we obtain

$$I_1 = -\frac{e^{2ija}}{4}\int_0^a \mathrm{d}x \int_0^\infty \mathrm{d}(iy')e^{-jy'}\frac{f(a-x,a+iy')}{\cos(a+iy')-\cos(a-x)}e^{-ijx} \tag{B.19}$$

$$+\frac{1}{4}\int_0^a \mathrm{d}x \int_0^\infty d(iy')e^{-jy'}\frac{f(a-x,a+iy')}{\cos(a+iy')-\cos(a-x)}e^{ijx} \tag{B.20}$$

$$+\frac{e^{2ija}}{4}\int_0^a \mathrm{d}x \int_0^\infty \mathrm{d}(iy')e^{-jy'}\frac{f(a-x,a+x+iy')}{\cos(a+x+iy')-\cos(a-x)} \tag{B.21}$$

$$-\frac{1}{4}\int_0^a \mathrm{d}x \int_0^\infty \mathrm{d}(iy')e^{-jy'}\frac{f(a-x,a+x+iy')}{\cos(a+x+iy')-\cos(a-x)}e^{2ijx}. \tag{B.22}$$

The terms in Eqs. B.20 and B.22 do not contain any poles and their asymptotic contributions are of sub-dominant j^{-2} character, similar to what we have seen for the rectangular domain in Sect. B.1. The term in Eq. B.19 contains a pole (as depicted in Fig. B.2) after we deformed the contour for the remaining integral over x variable. Computing the residue of this term we obtain the following contribution to the leading order[6]

$$\approx \frac{\pi}{8j\sin a}f(a,a)e^{2ija} \tag{B.23}$$

Up to this point the computations were equivalent to the computations in the rectangular example. However, there is one important difference due to the remaining term in Eq. B.21, which reads

$$\frac{e^{2ija}}{4}\int_0^\infty \mathrm{d}(iy')e^{-jy'}\underbrace{\int_0^a \mathrm{d}x\frac{f(a-x,a+x+iy')}{\cos(a+x+iy')-\cos(a-x)}}_{R}. \tag{B.24}$$

[6] Under the assumptions of separability and analyticity of f.

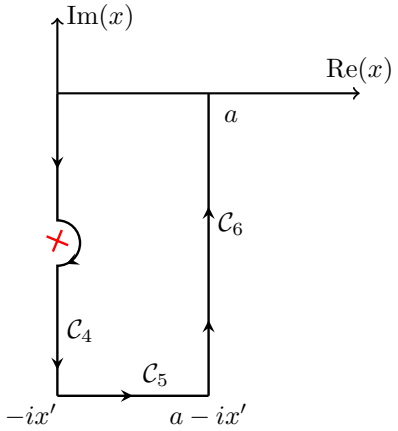

Figure B.2: Relevant contour of Eq. B.19. It is important to note that the overlapping contours for inner (over y variable) and outer (over x variable) are the ones along the $\mathrm{Re}(x) = 0$. This is different from what we had in the rectangular case (see Sect. B.1) where the overlapping contours were at $x = a$. This is due to the initial shift of the integration variables. The pole comes with a minus sign because of the anti-clockwise orientation.

We note that the R integral is an ordinary j independent integral! It contains no exponential factors and can be evaluated for a given function f.

As an example we choose $f(x, y) = \cos(x + y)$, a function that is even and analytic[7]. In this case we have

$$R = -\frac{1}{2\sin\left(a + \frac{iy'}{2}\right)} \cos(2a + iy') \int_0^a \frac{1}{\sin\left(x + \frac{iy'}{2}\right)} \mathrm{d}x. \tag{B.25}$$

This is in fact a well-known integral and we obtain

$$R = -\frac{\cos(2a + iy')}{2\sin\left(a + \frac{iy'}{2}\right)} \ln\left[\tan\left(\frac{a}{2} + \frac{iy'}{4}\right) \cot\left(\frac{iy'}{4}\right)\right]. \tag{B.26}$$

[7] In particular, this is the $I_{\mathrm{H}}^{\mathrm{T}}$ integral in Chapter 6.1.4.

Plugging this back into Eq. B.23 we find

$$-\frac{ie^{2ija}}{8}\int_0^\infty \mathrm{d}y' e^{-jy'}\frac{\cos(2a+iy')}{\sin\left(a+\frac{iy'}{2}\right)}\ln\left[\tan\left(\frac{a}{2}+\frac{iy'}{4}\right)\cot\left(\frac{iy'}{4}\right)\right].$$

Expanding around $y'=0$ [8] we obtain

$$-\frac{ie^{2ija}}{8}\frac{\cos(2a)}{\sin(a)}\int_0^\infty dy'\ln\Big[-4(y')^{-1}i\tan\left(\frac{a}{2}\right)\Big]e^{-jy'}.$$

Next we use the solution of the integral $\int_0^\infty e^{-xj}\ln(x)dx=-\frac{(\gamma+\ln(j))}{j}$ with $\gamma\approx 0.577...$ which is the Euler-Mascheroni constant which gives the following solution for the integral

$$R=-\frac{ie^{2ija}}{8j\sin(a)}\cos(2a)\Big(\ln j+\gamma+\ln 4\tan\left(\frac{a}{2}\right)\Big)-\frac{\pi\cos(2a)}{16j\sin(a)}e^{2ija}. \tag{B.27}$$

Therefore, together with the result from the residue, we obtain for the final expression for the leading order asymptotics in j^{-1} the following

$$I\approx\frac{\sin(2ja)\cos(2a)}{4j\sin(a)}\Big(\ln j+\gamma+\ln 4\tan\left(\frac{a}{2}\right)\Big)+\frac{\cos(2ja)\pi\cos(2a)}{8j\sin(a)}. \tag{B.28}$$

[8] Which is quivalent to considering the $j\to\infty$ limit.

Bibliography

[DL] NIST Digital Library of Mathematical Functions. http://dlmf.nist.gov/, Release 1.0.22 of 2019-03-15. F. W. J. Olver, A. B. Olde Daalhuis, D. W. Lozier, B. I. Schneider, R. F. Boisvert, C. W. Clark, B. R. Miller and B. V. Saunders, eds. 99, 101

[AC07] Francisco C. Alcaraz and Klaus Capelle. Density functional formulations for quantum chains. *Physical Review B*, 76(3):035109, Jul 2007. 6, 7, 56, 57, 58, 106, 115

[AEM+04] S. Andergassen, T. Enss, V. Meden, W. Metzner, U. Schollwoeck, and K. Schoenhammer. Functional renormalization group for luttinger liquids with impurities. *Physical Review B*, 70(7), Aug 2004. arXiv: cond-mat/0403517. 5, 17, 60

[AEM+06] S. Andergassen, T. Enss, V. Meden, W. Metzner, U. Schollwck, and K. Schnhammer. Renormalization-group analysis of the one-dimensional extended hubbard model with a single impurity. *Physical Review B*, 73(4):045125, Jan 2006. 67, 68, 69

[ASG+15] Xavier Andrade, David Strubbe, Umberto De Giovannini, Ask Hjorth Larsen, Micael J. T. Oliveira, Joseba Alberdi-Rodriguez, Alejandro Varas, Iris Theophilou, Nicole Helbig, Matthieu J. Verstraete, and et al. Real-space grids and the octopus code as tools for the

development of new simulation approaches for electronic systems. *Physical Chemistry Chemical Physics*, 17(47):3137131396, Nov 2015. 64

[BDZ08] Immanuel Bloch, Jean Dalibard, and Wilhelm Zwerger. Many-body physics with ultracold gases. *Reviews of Modern Physics*, 80(3):885964, Jul 2008. 3

[BF04] Henrik Bruus and Karsten Flensberg. *Many-Body Quantum Theory in Condensed Matter Physics: An Introduction*. Oxford University Press, Nov 2004. 10, 93

[BO99] Carl M. Bender and Steven A. Orszag. *Advanced Mathematical Methods for Scientists and Engineers: Asymptotic Methods and Perturbation Theory*. Springer, 1999 edition edition, Oct 1999. 128

[Bur12] Kieron Burke. Perspective on density functional theory. *The Journal of Chemical Physics*, 136(15):150901, Apr 2012. 41

[Car84] John L. Cardy. Conformal invariance and surface critical behavior. *Nuclear Physics B*, 240(4):514532, Nov 1984. 51

[CC13] Klaus Capelle and Vivaldo L. Campo. Density functionals and model hamiltonians: Pillars of many-particle physics. *Physics Reports*, 528(3):91159, Jul 2013. 7, 44

[CCR85] J. T. Chayes, L. Chayes, and Mary Beth Ruskai. Density functional approach to quantum lattice systems. *Journal of Statistical Physics*, 38(3):497518, Feb 1985. 45

[CLE93] M. F. Crommie, C. P. Lutz, and D. M. Eigler. Imaging standing waves in a two-dimensional electron gas. *Nature*, 363(6429):524, Jun 1993. 3

[CLSO03] K. Capelle, N. A. Lima, M. F. Silva, and L. N. Oliveira. Density-functional theory for the hubbard model: Numerical results for the luttinger liquid and the mott insulator. In N. I. Gidopoulos and S.Editors Wilson, editors,

The Fundamentals of Electron Density, Density Matrix and Density Functional Theory in Atoms, Molecules and the Solid State, Progress in Theoretical Chemistry and Physics, page 145168. Springer Netherlands, 2003. 68

[CNO+15] Lawrence W. Cheuk, Matthew A. Nichols, Melih Okan, Thomas Gersdorf, Vinay V. Ramasesh, Waseem S. Bakr, Thomas Lompe, and Martin W. Zwierlein. Quantum-gas microscope for fermionic atoms. *Physical Review Letters*, 114(19):193001, May 2015. 3

[CSN09] Aaron Clauset, Cosma Rohilla Shalizi, and M. E. J. Newman. Power-law distributions in empirical data. *SIAM Review*, 51(4):661703, Nov 2009. arXiv: 0706.1062. 60

[CSS06] Michele Casula, Sandro Sorella, and Gaetano Senatore. Ground state properties of the one-dimensional coulomb gas using the lattice regularized diffusion monte carlo method. *Physical Review B*, 74(24):245427, Dec 2006. 63

[DBGY10] Vikram V. Deshpande, Marc Bockrath, Leonid I. Glazman, and Amir Yacoby. Electron liquids and solids in one dimension. *Nature*, 464:209216, Mar 2010. 3

[DG90] Reiner M. Dreizler and Eberhard K. U. Gross. *Density Functional Theory: An Approach to the Quantum Many-Body Problem*. Springer-Verlag, 1990. 7

[Duf82] M. G. Duffy. Quadrature over a pyramid or cube of integrands with a singularity at a vertex. *SIAM Journal on Numerical Analysis*, 19(6):12601262, Dec 1982. 121

[Eco06] Eleftherios N. Economou. *Greens Functions in Quantum Physics*. Springer, 3rd edition edition, Jul 2006. 93

[EG95] Reinhold Egger and Hermann Grabert. Friedel oscillations for interacting fermions in one dimension. *Physical Review Letters*, 75(19):35053508, Nov 1995. 50

[EG96] Reinhold Egger and Hermann Grabert. *Friedel Oscillations in Luttinger Liquids*, page 133158. NATO ASI Series. Springer Netherlands, 1996. 62

[Egg00] Sebastian Eggert. Scanning tunneling microscopy of a luttinger liquid. *Physical Review Letters*, 84(19):44134416, May 2000. 3

[EMA+05] T. Enss, V. Meden, S. Andergassen, X. Barnab-Thriault, W. Metzner, and K. Schnhammer. Impurity and correlation effects on transport in one-dimensional quantum wires. *Physical Review B*, 71(15):155401, Apr 2005. 103

[Ens05] Tilman Enss. Renormalization, conservation laws and transport in correlated electron systems. *arXiv:cond-mat/0504703*, Apr 2005. arXiv: cond-mat/0504703. 5, 22

[Fra17] Fabio Franchini. *An Introduction to Integrable Techniques for One-Dimensional Quantum Systems*. Springer, 1st ed. 2017 edition edition, Jul 2017. 2, 28, 33, 35, 40, 51

[Fri58] J. Friedel. Metallic alloys. *Il Nuovo Cimento (1955-1965)*, 7(2):287311, Sep 1958. 1

[FW03] Alexander L. Fetter and John Dirk Walecka. *Quantum Theory of Many-Particle Systems*. Dover Publications, Jun 2003. 13

[Gia04] Thierry Giamarchi. *Quantum Physics in One Dimension*. Clarendon Press, 1 edition edition, Feb 2004. 2, 7, 30, 59, 66, 67

[Gia12] T. Giamarchi. Some experimental tests of tomonagaluttinger liquids. *International Journal of Modern Physics B*, 26(22):1244004, Jul 2012. 2, 3, 6

[Giu08] Gabriele Giuliani. *Quantum Theory of the Electron Liquid*. Cambridge University Press, 1 edition edition, Jun 2008. 1

[GPS08] Stefano Giorgini, Lev P. Pitaevskii, and Sandro Stringari. Theory of ultracold atomic fermi gases. *Reviews of Modern Physics*, 80(4):12151274, Oct 2008. 3

[GS86] O. Gunnarsson and K. Schnhammer. Density-functional treatment of an exactly solvable semiconductor model. *Physical Review Letters*, 56(18):19681971, May 1986. 44

[Hal80] F. D. M. Haldane. General relation of correlation exponents and spectral properties of one-dimensional fermi systems: Application to the anisotropic $s = \frac{1}{2}$ heisenberg chain. *Physical Review Letters*, 45(16):13581362, Oct 1980. 51

[Hal81] F. D. M. Haldane. Effective harmonic-fluid approach to low-energy properties of one-dimensional quantum fluids. *Physical Review Letters*, 47(25):18401843, Dec 1981. 2

[HD23] E Hückel and P Debye. The theory of electrolytes: I. lowering of freezing point and related phenomena. *Phys. Z*, 24:185–206, 1923. 1

[HFC+11] N. Helbig, J. I. Fuks, M. Casula, M. J. Verstraete, M. A. L. Marques, I. V. Tokatly, and A. Rubio. Density functional theory beyond the linear regime: Validating an adiabatic local density approximation. *Physical Review A*, 83(3):032503, Mar 2011. 62, 63

[HHK+15] Elmar Haller, James Hudson, Andrew Kelly, Dylan A. Cotta, Bruno Peaudecerf, Graham D. Bruce, and Stefan Kuhr. Single-atom imaging of fermions in a quantum-gas microscope. *Nature Physics*, 11(9):738742, Sep 2015. 3

[HK64] P. Hohenberg and W. Kohn. Inhomogeneous electron gas. *Physical Review*, 136(3B):B864B871, Nov 1964. 42

[Kan12] M. E. Kanal. Parallel algorithm on inversion for adjacent pentadiagonal matrices with mpi. *The Journal of Supercomputing*, 59(2):10711078, Feb 2012. 17

[Kar18] C. Karrash. *Private communication*. 2018. 37

[KBI97] V. E. Korepin, N. M. Bogoliubov, and A. G. Izergin. *Quantum Inverse Scattering Method and Correlation Functions*. Cambridge University Press, Mar 1997. 36, 39, 40

[KBYH01] K. Kanisawa, M. J. Butcher, H. Yamaguchi, and Y. Hirayama. Imaging of friedel oscillation patterns of two-dimensionally accumulated electrons at epitaxially grown inas(111) *A* surfaces. *Physical Review Letters*, 86(15):33843387, Apr 2001. 3

[KF92] C. L. Kane and Matthew P. A. Fisher. Transport in a one-channel luttinger liquid. *Physical Review Letters*, 68(8):12201223, Feb 1992. 49

[Kle] Lennart Klebl. Friedel oscillations in one-dimensional many-body systems with long-range interaction, bachelor thesis, rwth aachen 2017. 63

[KM98] Michael Karbach and Gerhard Muller. Introduction to the bethe ansatz i. *arXiv:cond-mat/9809162*, Sep 1998. arXiv: cond-mat/9809162. 30

[KM12] C. Karrasch and J. E. Moore. Luttinger liquid physics from infinite-system dmrg. *arXiv:1207.0011 [cond-mat]*, Jun 2012. arXiv: 1207.0011. 5, 38

[KMT99] N. Kitanine, J. M. Maillet, and V. Terras. Form factors of the xxz heisenberg spin-12 finite chain. *Nuclear Physics B*, 554(3):647678, Aug 1999. 4

[KS65] W. Kohn and L. J. Sham. Self-consistent equations including exchange and correlation effects. *Physical Review*, 140(4A):A1133A1138, Nov 1965. 42

[KSA+05] S. Kurth, G. Stefanucci, C.-O. Almbladh, A. Rubio, and E. K. U. Gross. Time-dependent quantum transport: A practical scheme using density functional theory. *Physical Review B*, 72(3), Jul 2005. arXiv: cond-mat/0502391. 22

[LSOC03] N. A. Lima, M. F. Silva, L. N. Oliveira, and K. Capelle. Density functionals not based on the electron gas: Local-density approximation for a luttinger liquid. *Physical Review Letters*, 90(14):146402, Apr 2003. 6, 7, 60, 68

[Lut63] J. M. Luttinger. An exactly soluble model of a manyfermion system. *Journal of Mathematical Physics*, 4(9):11541162, Sep 1963. 2

[LW68] Elliott H. Lieb and F. Y. Wu. Absence of mott transition in an exact solution of the short-range, one-band model in one dimension. *Physical Review Letters*, 20(25):14451448, Jun 1968. 66

[Mah00] Gerald D. Mahan. *Many-Particle Physics*. Springer, 3rd ed. 2000 edition edition, Oct 2000. 11

[MM16] L. Markhof and V. Meden. Spectral function of the tomonaga-luttinger model revisited: Power laws and universality. *Physical Review B*, 93(8):085108, Feb 2016. 60

[MMS+00] V. Meden, W. Metzner, U. Schollwck, O. Schneider, T. Stauber, and K. Schnhammer. Luttinger liquids with boundaries: Power-laws and energy scales. *The European Physical Journal B*, 16(4):631646, Aug 2000. 67, 86, 87

[MOB12] Miguel A. L. Marques, Micael J. T. Oliveira, and Tobias Burnus. Libxc: A library of exchange and correlation functionals for density functional theory. *Computer Physics Communications*, 183(10):22722281, Oct 2012. 63

[MSH+12] Walter Metzner, Manfred Salmhofer, Carsten Honerkamp, Volker Meden, and Kurt Schnhammer. Functional renormalization group approach to correlated fermion systems. *Reviews of Modern Physics*, 84(1):299352, Mar 2012. 5

[NM05] Reinhard M. Noack and Salvatore R. Manmana. Diagonalization and numerical renormalizationgroupbased methods for interacting quantum systems. *AIP Conference Proceedings*, 789(1):93163, Sep 2005. 4

[Orb58] R. Orbach. Linear antiferromagnetic chain with anisotropic coupling. *Physical Review*, 112(2):309316, Oct 1958. 32

[PS01] John P. Perdew and Karla Schmidt. Jacobs ladder of density functional approximations for the exchange-correlation energy. *AIP Conference Proceedings*, 577(1):120, Jul 2001. 41

[PSH+98] L. Petersen, P. T. Sprunger, Ph. Hofmann, E. Lgsgaard, B. G. Briner, M. Doering, H.-P. Rust, A. M. Bradshaw, F. Besenbacher, and E. W. Plummer. Direct imaging of the two-dimensional fermi contour: Fourier-transform stm. *Physical Review B*, 57(12):R6858R6861, Mar 1998. 3

[QFY+97] Shaojin Qin, Michele Fabrizio, Lu Yu, Masaki Oshikawa, and Ian Affleck. Impurity in a luttinger liquid away from half-filling: A numerical study. *Physical Review B*, 56(15):97669774, Oct 1997. 40

[RHL+17] Keno Riechers, Klaus Hueck, Niclas Luick, Thomas Lompe, and Henning Moritz. Detecting friedel oscillations in ultracold fermi gases. *The European Physical Journal D*, 71(9):232, Sep 2017. 3

[Sch90] H. J. Schulz. Correlation exponents and the metal-insulator transition in the one-dimensional hubbard model. *Physical Review Letters*, 64(23):28312834, Jun 1990. 66

[Sch93] H. J. Schulz. Wigner crystal in one dimension. *Physical Review Letters*, 71(12):18641867, Sep 1993. 63, 65

[Sch02] K. Schönhammer. The luttinger liquid concept for interacting electrons in one dimension. *Journal of Physics: Condensed Matter*, 14(48):1278312791, Nov 2002. 3

[Sch11a] Ulrich Schollwöck. The density-matrix renormalization group in the age of matrix product states. *Annals of Physics*, 326(1):96192, Jan 2011. 4, 5

[Sch11b] Ulrich Schollwöeck. The density-matrix renormalization group in the age of matrix product states. *Annals of Physics*, 326(1):96192, Jan 2011. arXiv: 1008.3477. 5, 38

[SDSE08] Stefan Schenk, Michael Dzierzawa, Peter Schwab, and Ulrich Eckern. Successes and failures of bethe ansatz density functional theory. *Physical Review B*, 78(16):165102, Oct 2008. 5, 6, 7, 56

[SG05] George E. Simion and Gabriele F. Giuliani. Friedel oscillations in a fermi liquid. *Physical Review B*, 72(4):045127, Jul 2005. 1, 2

[SL13] Gianluca Stefanucci and Robert van Leeuwen. *Nonequilibrium Many-Body Theory of Quantum Systems: A Modern Introduction*. Cambridge University Press, 1 edition edition, Apr 2013. 47

[SMM+00] K. Schnhammer, V. Meden, W. Metzner, U. Schollwck, and O. Gunnarsson. Boundary effects on one-particle spectra of luttinger liquids. *Physical Review B*, 61(7):43934396, Feb 2000. 66, 67, 68, 87, 117

[SMMS02] U. Schollwöck, V. Meden, W. Metzner, and K. Schönhammer. DMRG studies of impurities in Luttinger Liquids. *Progress of Theoretical Physics Supplement*, 145:312319, Feb 2002. 4

[Sól79] J. Sólyom. The fermi gas model of one-dimensional conductors. *Advances in Physics*, 28(2):201303, Apr 1979. 67, 71, 87

[SSDE11] S. Schenk, P. Schwab, M. Dzierzawa, and U. Eckern. Density functional theory for a model quantum dot: Beyond the local-density approximation. *Physical Review B*, 83(11):115128, Mar 2011. 47

[TZ85] I. Tütto and A. Zawadowski. Quantum theory of local perturbation of the charge-density wave by an impurity: Friedel oscillations. *Physical Review B*, 32(4):24492470, Aug 1985. 1

[Ull12] Carsten Ullrich. *Time-Dependent Density-Functional Theory: Concepts and Applications*. Oxford University Press, 1 edition edition, Feb 2012. 7, 44, 45, 57, 109

[Vid07] G. Vidal. Classical simulation of infinite-size quantum lattice systems in one spatial dimension. *Physical Review Letters*, 98(7), Feb 2007. arXiv: cond-mat/0605597. 5, 38

[VLRK03] G. Vidal, J. I. Latorre, E. Rico, and A. Kitaev. Entanglement in quantum critical phenomena. *Physical Review Letters*, 90(22):227902, Jun 2003. 4

[WBS+14] Lucas O. Wagner, Thomas E. Baker, E. M. Stoudenmire, Kieron Burke, and Steven R. White. Kohn-sham calculations with the exact functional. *Physical Review B*, 90(4):045109, Jul 2014. 41

[Whi92] Steven R. White. Density matrix formulation for quantum renormalization groups. *Physical Review Letters*, 69(19):28632866, Nov 1992. 4

[Whi93] Steven R. White. Density-matrix algorithms for quantum renormalization groups. *Physical Review B*, 48(14):1034510356, Oct 1993. 4

[WVP96] Y. Wang, J. Voit, and Fu-Cho Pu. Exact boundary critical exponents and tunneling effects in integrable models for quantum wires. *Physical Review B*, 54(12):84918500, Sep 1996. 4, 51

[ZA97] Alexandre M. Zagoskin and Ian Affleck. Fermi edge singularities: Bound states and finite-size effects. *Journal of Physics A: Mathematical and General*, 30(16):5743, 1997. 90

[ZMM+11] B. Zimmermann, T. Müller, J. Meineke, T. Esslinger, and H. Moritz. High-resolution imaging of ultracold fermions in microscopically tailored optical potentials. *New Journal of Physics*, 13(4):043007, Apr 2011. 3